Nanofiber-Reinforced Soft Robotic Actuators

a dissertation presented
by
Nina R. Sinatra
to
The School of Engineering and Applied Sciences

in partial fulfillment of the requirements
for the degree of
Doctor of Philosophy
in the subject of
Engineering Sciences

Harvard University
Cambridge, Massachusetts
January 2019

©2019 – Nina R. Sinatra
all rights reserved.

Thesis advisor: Professor Robert J. Wood Author: Nina R. Sinatra

Nanofiber-Reinforced Soft Robotic Actuators

Abstract

The advent of soft robotics has facilitated the development of highly compliant actuators and end effectors using pliable materials such as polymers and foams. Unlike conventional metal or plastic devices, soft robots are well suited for industrial and medical applications requiring extreme care, flexible form factors, smooth motions, and low applied forces. A fundamental challenge across many of these domains is gentle handling of fragile materials.

In this thesis, we develop nanofiber-reinforced composite soft actuators and demonstrate their utility for gentle grasping. We conduct a multiscale analysis of nanofiber structure, mechanics, and processing parameters, and apply these conclusions toward engineering novel manufacturing techniques for tough, highly aligned fibers. To facilitate design of multi-layer composite actuators, we derive two analytical models which describe the influence of fiber orientation and layup design on actuator curvature and motion. Combining multiple actuators into an ultra-compliant end effector, we demonstrate the capability of this device to perform unprecedented delicate manipulation tasks using laboratory tank testing and pilot field studies.

Contents

0 Introduction 1
- 0.1 Brief Survey of Soft Robotics . . . 1
- 0.2 Soft Robotic Manipulators . . . 3
- 0.3 Modeling Soft Robotic Actuators . . . 4
- 0.4 Nanofibers: Why Scale Matters . . . 6
- 0.5 Contributions . . . 8
- 0.6 Thesis Outline . . . 9

1 Controlling anisotropy and mechanics of polymer nanofibers 11
- 1.1 Introduction . . . 11
- 1.2 Experimental Setup . . . 13
- 1.3 Manufacturing Nanofibers Using Pull Spinning . . . 17
- 1.4 Mechanism behind Fiber Formation . . . 18
- 1.5 Quantifying Anisotropy of Pull Spun Nanofibers . . . 21
- 1.6 Fiber Muscular Thin Films Support Contractility Measurements . . . 22
- 1.7 Nanofiber Anisotropy Influences Material Performance . . . 26
- 1.8 Point-of-Use Apparel Fabrication . . . 28
- 1.9 Summary . . . 30

2 Fabricating Multi-Material Nanofabrics using Rotary Jet Spinning 32
- 2.1 Introduction . . . 32
- 2.2 Experimental Setup . . . 35
- 2.3 Fiber Structure Conserved across Reservoirs . . . 36
- 2.4 Fabric Composition Influences Material Mechanics . . . 38
- 2.5 Manufacturing Composite Nanofabrics using Orthogonal Solvents . . . 40
- 2.6 Summary . . . 42

3 Nanofiber-Reinforced Soft Fluidic Micro-Actuators 44
- 3.1 Introduction . . . 44
- 3.2 Experimental Methods . . . 47
- 3.3 Nanofiber Morphology is Independent of Post-Processing . . . 54

3.4 Effect of Nanofiber Orientation and Actuator Design on Bending 55
3.5 Composite structure influences bulk mechanical properties 59
3.6 Regulating actuator bending using nanofiber orientation 64
3.7 Summary 65

4 Model-Driven Design of Nanofiber-Reinforced Soft Fluidic Actuators Capable of Complex 3D Motions 66
4.1 Introduction 67
4.2 Experimental Methods 69
4.3 Results and Discussion 77
4.4 Summary 84

5 Ultra-Gentle Manipulation of Delicate Structures using a Soft Robotic Gripper 86
5.1 Introduction 86
5.2 Experimental Methods 89
5.3 Design Criteria for Ultra-Gentle Gripper 93
5.4 Evaluation of Underwater Grasping Performance 98
5.5 Preliminary Field Testing of Soft Robotic Gripper 105
5.6 Summary 107

6 Conclusion 109
6.1 Summary 109
6.2 Point-of-Use Textiles 111
6.3 Sensing via Multi-Material Nanotextiles 112
6.4 Expanding the Topography of Fiber-Reinforced Actuators 112
6.5 The Future of Soft Robotic Gripping: Modular and Multi-Functional 113
6.6 Interactive Soft Robotics in Entertainment 115
6.7 Conclusion 116

Appendix A Appendix A 117
A.1 Nanofiber Scaffolds for Tissue Engineering 117
A.2 Structural Properties of Polymer Nanofibers 119
A.3 Mechanical Properties of Composite Micro-Actuators 126
A.4 Laminate Plate Model for Soft Composite Actuators 128
A.5 Performance of Soft Marine Grippers 131

References 158

Listing of figures

1 Soft robots . . . 3
2 SEM micrographs of micro- and nanofibers. . . . 5
3 Nanofiber manufacturing processes. . . . 7

1.1 Design and function of the pull spinning system. . . . 16
1.2 Characterizing pull spun nanofibers and system parameters. . . . 19
1.3 Fiber muscular thin films (fMTFs) for *in vitro* functional testing of muscle tissue. . . . 23
1.4 Pull spun nanofibers for point-of-wear apparel design. . . . 25
1.5 Mechanical properties of pull spun nanofibers . . . 29

2.1 Multi-material nanotextile fabrication . . . 34
2.2 Morphology of rotary jet spun nanofibers . . . 38
2.3 Mechanical properties of pure, blend, and multi-material nanofabrics . . . 40
2.4 2D FTIR contour maps of multi-modal nanotextiles . . . 41
2.5 FTIR spectra of nanofabrics with orthogonal solvents . . . 43

3.1 Classification of soft actuators . . . 46
3.2 Fiber fabrication and post-processing . . . 54
3.3 Fabricating composite soft actuators . . . 56
3.4 Schematic of composite micro-actuators . . . 57
3.5 Analytical and empirical actuator curvature . . . 60
3.6 Curvature of composite micro-actuators . . . 61
3.7 Mechanical properties of composite and elastomer actuators . . . 62
3.8 Bend-twist coupling of micro-actuators . . . 63

4.1 Soft elastomer and composite actuators . . . 68
4.2 Manufacturing mesoscale nanofiber-reinforced actuators . . . 70
4.3 Analytical predictions for actuator twist . . . 79
4.4 Bend-twist coupled nanofiber-reinforced actuators . . . 83
4.5 Soft actuators with hybrid bending modes . . . 85

5.1 Soft robotic actuation in the deep sea . . . 90

5.2 Fabricating nanofiber-reinforced soft robotic actuators 92
5.3 Selecting actuator geometry 95
5.4 Contact pressure of soft actuators 97
5.5 Soft gripper region of acquisition 99
5.6 Robustness of soft gripper to external forces 103
5.7 Hand-held soft robotic gripping device 104
5.8 Gentle grasping of *Aurelia aurita* 105

A.1 SEM images of pull spun nanofibers 120
A.2 Calibration of pull spinner motor 120
A.3 Radius and alignment of nanofibers 122
A.4 Fiber radius vs. fabrication time 123
A.5 Viscosity of polymer solution 125
A.6 Thickness of fiber muscular thin films 126
A.7 Mechanical properties of composite actuators 127
A.8 Pressure vs. inflating channel area 128
A.9 Failure pressure and fiber reinforcement 129
A.10 Schematic of composite actuator lamina 130
A.11 Varying matrix and nanofiber stiffness values 131
A.12 Destructive grasp attempt of gelatinous acorn worm 132
A.13 Drag force vs. soft gripper speed 135
A.14 Maximum pull force using a caging grasp 136

Acknowledgments

First, I would like to thank my advisor, Prof. Robert Wood, for his phenomenal mentorship and tutelage. As a result of his leadership and care, my time in the Microrobotics Lab has been enjoyable, productive, and rewarding. Rob's consistent and enthusiastic support has enabled me to explore exciting research directions and to develop further as an engineer. Additionally, I would like to thank my committee members, Prof. Joost Vlassak and Prof. Jennifer Lewis, for their insights and feedback. My collaboration with Prof. Vlassak was indispensable for developing analytical models of my robotic actuators. I appreciate his patience and guidance throughout that process, and have learned a great deal from our conversations.

I am also grateful for the collaborations that I have had the opportunity to participate in during my time in the Microrobotics Lab. In particular, I want to thank Daniel Vogt, Clark Teeple, Kaitlyn Becker, and Prof. David Gruber for all that they have taught me about robotics and marine biology. Our conversations and teamwork have made my PhD experience infinitely richer and more interesting. I would also like to thank aquarists Steve Spina, Chris Doller, and the New England Aquarium for their patience, assistance, and jellyfish wrangling during our field experiments. I greatly appreciate the opportunity to collaborate with Anand Varma and Jason Jaacks, and remain in awe of the spectacular photos and videos that they captured of our robot.

I am thankful for the great support that I have received from many individuals in the Harvard community, especially Cate Lagueux and Dr. John Girash. Your advocacy, advice, and assistance have propelled me toward greater success and confidence during this journey.

I would like to extend my heartfelt appreciation to my parents, Nancy and Louis, without whose unparalleled generosity, guidance, and love I would not have achieved this dream. From exciting successes to challenging moments, their presence, confidence, and strength have constantly driven me forward to conquer my most ambitious goals. Finally, I would like to thank my fiancé, Alborz, whose unwavering encouragement, support, and belief in me has galvanized me to sharpen my resolve and reach new heights.

Author List

The following authors contributed to this thesis:

Prof. Leila F. Deravi, Dr. Christophe O. Chantre, Dr. Alexander P. Nesmith, Prof. Hongyan Yuan, Dr. Thomas Grevesse, Josue A. Goss, Dr. Mohammad R. Badrossamy, and Dr. Luke A. MacQueen, to Chapter 1.

Prof. Johan U. Lind, to Chapter 2.

Prof. Kevin Kit Parker, to Chapters 1, 2, and 3.

Prof. Tommaso Ranzani, to Chapter 3.

Prof. Joost J. Vlassak, to Chapters 3 and 4.

Prof. David Gruber, to Chapter 5.

Clark Teeple, to Chapter 5.

Daniel Vogt, to Chapter 5.

0 Introduction

0.1 Brief Survey of Soft Robotics

The field of soft robotics has developed rapidly within the past thirty years, producing an exciting body of work involving flexible material design, smooth movements and locomotion, and novel grasping paradigms[1,2,3,4]. However, to fully appreciate the scope of the field, we must first ask: 1) what is a soft robot, and 2) what useful qualities do they possess? To answer these questions, we will

briefly examine the history and state of the soft robotics field, exploring the common elements that unite devices in this domain.

Soft robots are generally classified based on the inherent mechanical compliance of their constituent materials, and the smooth motions and large deformations that they undergo. The conventional idea of a robotic system involves a hard metallic or plastic exterior, discrete degrees of freedom, and limited flexibility. When asked to give an example of a robot, the average individual might think of the rapid, precise motions of an industrial robot assembling a car, the sturdy chassis of an automated vacuum cleaning the floor, or even the rigid humanoid forms of science fiction. In contrast, the field of soft robotics draws inspiration from natural structures, processes, and motions[5]. The building blocks for these machines - components such as silicone rubbers, hydrogels, granular media, and fabric - are inherently pliable and flexible. One of the earliest examples of a soft actuator is the McKibben artifical muscle, inspired by human muscular tissue and originally used for orthopedic rehabilitation[6]; these devices extend and contract by pressurizing a soft bladder reinforced circumferentially with a woven shell[7,8,9]. As the implementation of compliant materials within robots progressed, other works explored the utility of soft fingertips for grasping robots using materials such as foam, gel, and rubber[10]; these studies concluded that pliable robot fingertips can improve grasp stability and energy dissipation[11,12].

Rather than covering rigid structures with soft coatings, subsequent publications explored the use of encapsulated granular materials to perform conformal grasping under applied shear stress[13,14,15]. Over time, the focus of the field shifted from the development of soft components within comparatively rigid structures to the design and fabrication of fully soft robots[16]. Today, the majority of soft robotic actuators are developed for two major applications: locomotion and grasping; examples of several contemporary devices are displayed in Figure 1. Terrestrial locomotive soft robots use techniques such as low-pressure pneumatic pressurization or shape memory alloys to generate a crawling or undulating motion[17,18,19]. These devices draw inspiration from the motion of inchworms[20],

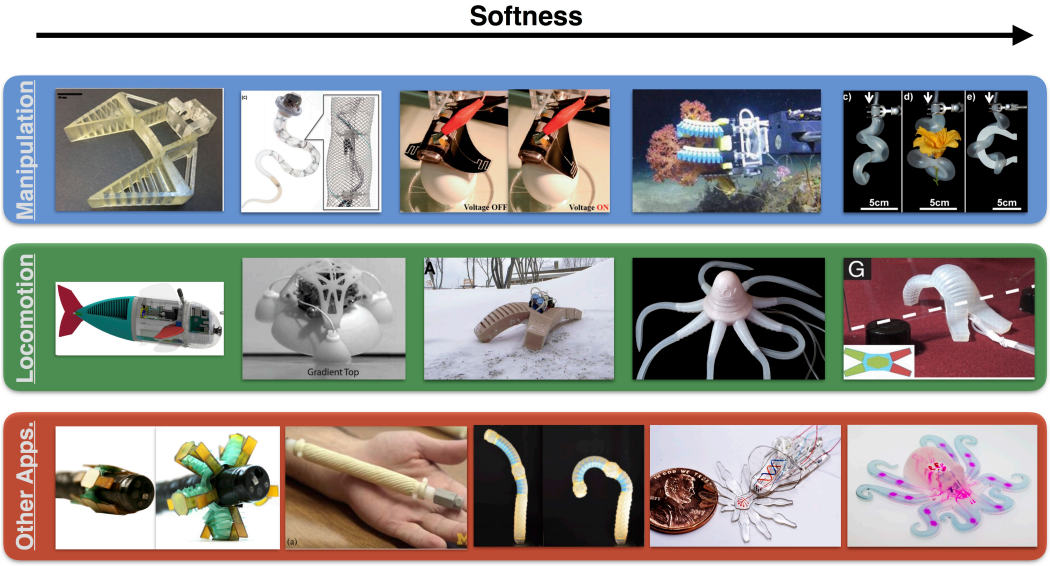


Figure 1: Various examples of soft robotic devices. Manipulators, from left: Fin Ray[27]; SMA-driven soft robotic octopus arm[28,5]; electroadhesion-based dielectric elastomer actuators[29]; squishy robot fingers[30]; and elastomeric robot tentacles[31]. Locomotors, from left: SoFi soft robotic fish[32]; functionally graded soft robot[33]; untethered soft robot[18]; bioinspired soft octopus robot[34]; and multigait soft robot[17]. Other applications, from left: deployable endoscopic stabilizers[35]; fiber-reinforced elastomeric enclosure (FREE) actuators[36]; trajectory matching fiber-reinforced soft actuator[37]; Microfluidic Origami for Reconfigurable Pneumatic/Hydraulic (MORPH) device[38]; and 3D printed soft robot powered by catalytic decomposition[16].

caterpillars[21], and snakes[22]. Marine locomotion has also been achieved using dielectric elastomers inspired by the motion of fins[23,24,25], and pneumatic actuators whose contraction mimics the stroke of a manta ray[26].

0.2 Soft Robotic Manipulators

Soft robotic end effectors are developed to interface with compliant structures, or to deploy in domains for which contact with rigid structures may result in damage or discomfort[39,1]. The smooth motions and flexible bodies of these high aspect ratio devices make them useful tools for minimally invasive surgeries[40,41,42,43,44], rehabilitation[45,46,2], agricultural produce handling[47,48,49], micromanipulation[50,51,52], and interacting with delicate organisms[30]. A common challenge across these ap-

plications is gentle handling of fragile materials in dynamic environments. Many devices consist of compliant elastomeric matrices containing internal channels or structures. These robots are pressurized pneumatically, hydraulically, by applying heat to shape memory polymers, or by using tension cables, thus stimulating the structure to bend, extend, and/or twist[53,28]. As with soft locomotors, flexible robotic grippers often draw inspiration from nature. For example, Cianchetti et al developed an artificial muscular hydrostat whose design and motion mimics that of an octopus arm[54,28]. Schaffner et al also demonstrated a synthetic muscular hydrostat by 3D printing photocurable silicone inks of various stiffnesses in alternating patterns[55]. The bending mode of this class of actuators is determined by exploiting features such as geometric asymmetry[56,57,58], fiber reinforcement[59,60], and variable material stiffness[61].

0.3 Modeling Soft Robotic Actuators

Conventional robots operate in six degrees of freedom, encompassing Cartesian displacements in the x, y, and z directions and rotations around these axes. However, soft robots are capable of more fluid trajectories than their rigid counterparts. For instance, a pneumatically actuated robot moves passively through a continuous path. This movement represents a shift from defined, discrete motion to nearly infinite degrees of freedom. For this reason, many compliant robots are considered to be under-actuated. Moreover, the hyperelastic materials used as building blocks for soft actuators result in large deformations and a nonlinear relationship between input pressure, stress, and strain. These features introduce significant challenges into modeling soft actuator static and kinematic behavior, control, and mechanics. To capture this behavior, studies have used strategies such as nonlinear elasticity approaches[26], optimization algorithms[37], Euler-Bernoulli beam mechanics[62], and support vector regression methods[63].

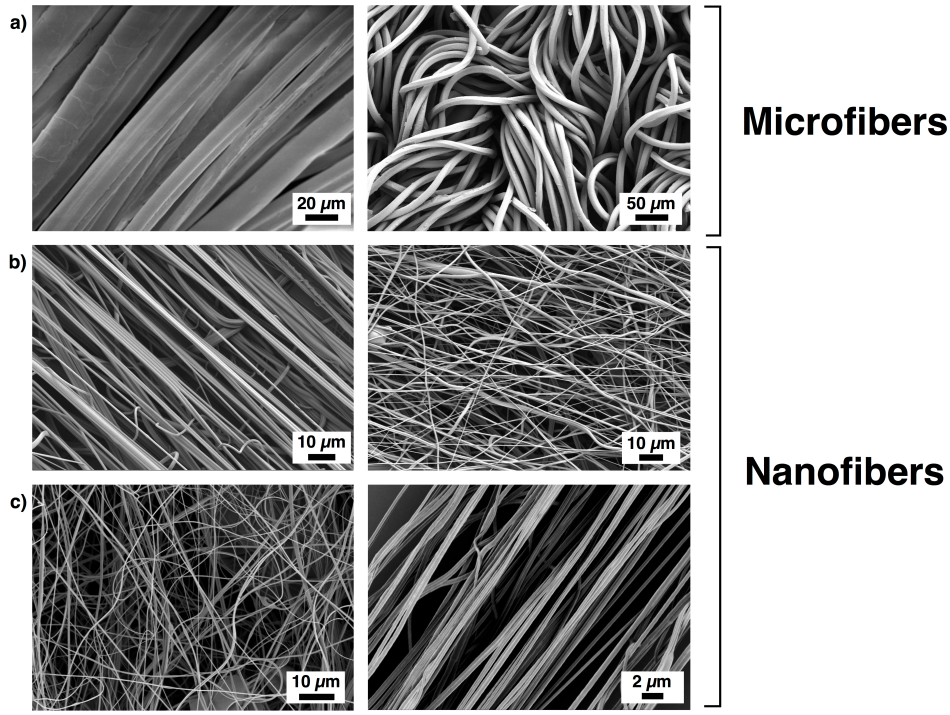


Figure 2: SEM micrographs of micro- and nanofibers composed of a variety of polymer and protein materials. a) *from left*: Fabric sample from a sportswear garment containing wool, lycra, and Coolmax (polyester) fibers; Spandex fibers. b) *from left*: Polyurethane and hybrid polyurethane/nylon nanofibers. c) *from left*: Polycaprolactone/gelatin and Poly(vinylidene fluoride-co-trifluoroethylene) nanofibers.

0.4 Nanofibers: Why Scale Matters

This dissertation discusses the design of novel soft actuators and the fabrication of innovative fibrous materials to direct the motion of these robots. Specifically, we will focus on the production and characterization of nanofibers. Nanofibers are defined as high aspect ratio structures whose diameter is less than 1 μm. To lend perspective to this number, the average human hair has an diameter of 50 μm. Like the microfibers (Figure 2a) which compose most of the textile structures with which we are familiar – such as garments, tents, and furniture covers – nanofibers can be manufactured from a wide variety of constituent materials, including polymers, proteins, metals, and plant materials (Figure 2b-c). Unlike microfibers, nanoscale fibers exhibit unique features such as a high surface area-to-volume ratio (up to 10^3 times that of microfibers[64]), tunable stiffness, and large specific strength. These characteristics are important design parameters for engineering materials where nano- and micro-scale topology inform macroscale applications that range from textiles[65,66], tissue engineering scaffolds[67,68,69,70,71], and drug delivery[72,73,74] to filtration[75], sensors[69,76,77], catalysis[78,79,80], and optics[81,82,83].

0.4.1 Polymer Nanofiber Manufacturing

Such a broad scope of applications demands versatile manufacturing techniques amenable to multiple material processing conditions. Across various fabrication approaches, the first step to generating polymer-based nanofibers involves preparing a precursor solution of the desired components. In most cases, the selected polymer(s) are either dissolved in an organic solvent or melted to form this liquid. A fiber is produced by drawing small volumes of the viscous precursor solution into a jet, which either cools the molten polymer or evaporates the volatile solvent to expose a polymer bundle. Properties such as fiber diameter, tensile strength, process throughput, and the percentage of morphological defects are regulated through solution viscosity, solvent selection, polymer con-

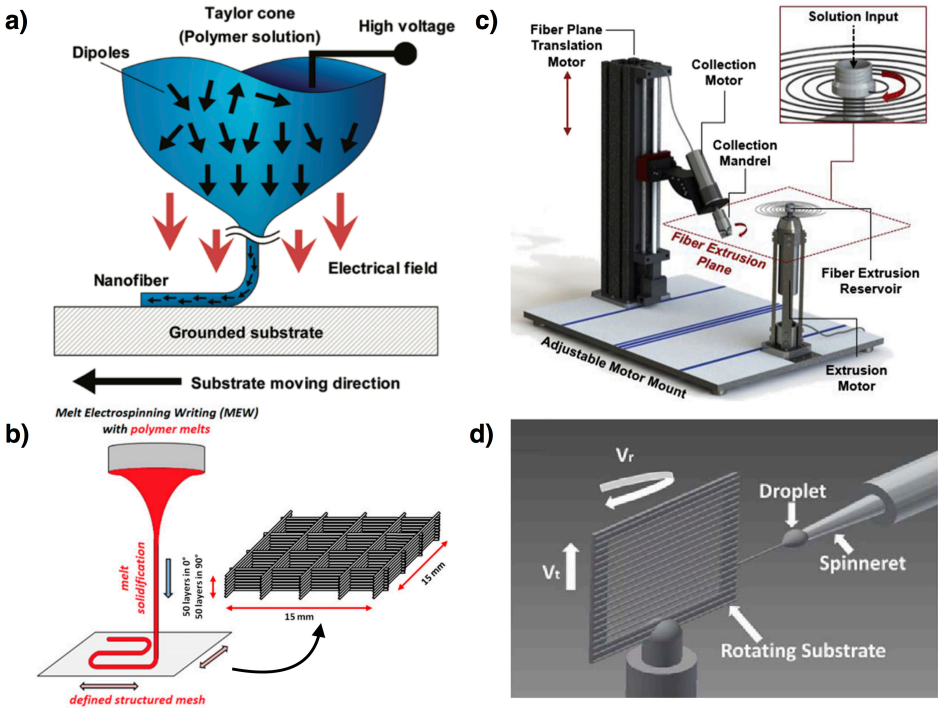


Figure 3: Schematics of nanofiber fabrication processes, including: a) near-field electrospinning (adapted from [84]), b) melt electrospinning (adapted from [85]), c) rotary jet spinning (adapted from [86]), and d) Spinneret-Based Tunable Engineered Parameters (STEP) technique (adapted from [87]).

centration, and process-specific manufacturing parameters. However, there exist a wide variety of techniques that can be used to generate polymer nanofibers.

Current fiber-fabrication systems include electro-[64,88] (Figure 3a), melt[89,90] (Figure 3b), dry[91,92], or wet spinning[93,94] — all of which incorporate solution extrusion through an orifice in the presence of high temperature and pressure (melt, dry, and wet spinning) or electric field (5-20 kV, electrospinning)[64,88]. Once formed, the fibers can be collected and processed using external pumps, alternating applied electric fields, spinnerets, coagulation, and wash chambers, or heated drum rolls to form aligned functional materials[64,88,95,96]. The development of centrifugal force-based systems, such as rotary jet spinning (Figure 3c), and spinneret extrusion methods[97,98,87] (Figure 3d) have streamlined nanofiber production by reducing the number of process parameters and eliminating

the reliance on electric fields for fiber formation[99,100,101,102].

0.5 Contributions

The objectives of this dissertation are the examination of mechanical and chemical principles governing polymer nanofiber formation, and the use of these materials to enable novel grasping capabilities for soft robotic manipulators. Toward these goals, we investigated the relationship between processing parameters, fiber structure, and fabric mechanics. To improve our ability to regulate these properties, we developed nanofiber manufacturing techniques which yield highly aligned textile scaffolds and multi-material nonwoven sheets. We then incorporated nanofabrics into soft robotic actuators, and derived two analytical models to determine the impact of fiber orientation, actuator geometry, and input pressure on device curvature and motion. The utility of these robotic end effectors for delicate manipulation tasks was investigated through laboratory tank testing and pilot field studies. The results of these experiments demonstrate the ability of nanofiber-reinforced soft actuators to perform unprecedented gentle grasping tasks. These contributions can be briefly summarized as follows:

1. Establishment of novel methods for manufacturing nanofabrics with controllable composition, orientation, and mechanics.

2. Design of a nanofiber-reinforced soft actuator that is robust and reproducible.

3. Analytical models of composite actuator motion as a function of air pressure, nanofiber orientation, fiber and elastomer stiffness, and laminate structure.

4. Nondestructive grasping of ultra-low modulus (<1 kPa) substrates.

0.6 Thesis Outline

This dissertation explores the structure:function relationship of polymer nanofabrics, presents analytical tools for designing soft robotic actuators using nanofibers, and demonstrates the use of such actuators for gentle manipulation. Chapter 1 focuses on the design and validation of a nanofiber fabrication process capable of producing highly anisotropic fiber scaffolds with controllable mechanical and structural properties. We interrogated the critical processing parameters of this system, and assessed their impact on fiber morphology and tensile strength. Moreover, we presented two proof-of-concept studies demonstrating the efficacy for this process in synthesizing tissue engineering scaffolds and point-of-use apparel.

In Chapter 2, we further explored the structure:function relation of nanofibers by examining the composition and mechanics of bulk nanofabrics. Specifically, we developed a novel approach to manufacturing multi-material nanotextiles. This technique produced composite nanofabrics that display higher toughness than either of the constituent polymers alone. Moreover, we demonstrated the utility of this method to produce functional nanofabrics by fabricating a nonwoven using a piezoelectric polymer, an elastic fiber, and two immiscible solvents.

Chapter 3 describes the integration of nanofiber sheets into soft robotic actuators. We present a technique that combines rotary jet spinning with soft lithography to produce a fiber-reinforced micro-actuator. The purpose of the nanotextile is to limit strain during the pneumatic actuation of the device, biasing the bending motion toward one direction. The relationship between actuator geometry, fiber mechanics, and device curvature is explored both analytically and empirically. In addition, we discuss the potential to imbue soft actuators with a wider variety of motions by adjusting nanofiber orientation; this theme is explored more extensively in the following chapter.

Chapter 4 builds upon our developing understanding of the composite actuator design space, and presents a more comprehensive analytical model for actuator motion. Using this framework, we

ascertained the relationship between fiber alignment and actuator stiffness, and described a platform for predictive design of soft devices with coupled bending modes. As a case study, we examined bending-twisting coupled motion, and derived the relation between fiber orientation and actuator twist.

In Chapter 5, we demonstrate the grasping capabilities of soft nanofiber-reinforced actuators. To understand the parameter space in which they operate, we mapped the region of acquisition, assessed the actuators' resistance to perturbations during a grasp, and evaluated the effect of retraction speed on gripping ability. Finally, we validated the ability of our soft actuators to perform nondestructive grasping of ultra-soft substrates (<1 kPa) through a pilot study featuring gelatinous marine species.

Finally, we conclude with a brief discussion of future avenues for nanofiber research and soft robotic development. This section highlights challenges and capability gaps within advanced fiber manufacturing and recommends potential strategies to address them. We propose paths to build upon the work presented in this thesis and describe applications and features for next-generation soft robotic devices.

1

Controlling anisotropy and mechanics of polymer nanofibers

1.1 Introduction

Advanced manufacturing of nanofiber constructs requires the ability to tune network composition, orientation, and structure under ambient conditions using minimal processing parameters.

Several electrospinning techniques have been developed to control fiber deposition and structure, producing aligned fibrous nanostructures by minimizing the distance between a charged nozzle and grounded collector[103,104,105,106,107,108]. While these modifications enable geometries which were previously unattainable for electrospun fibers, the technique remains limited in both speed and the range of materials used. Furthermore, harsh reaction environments, low production rates, and lengthy post-processing steps challenge existing systems to rapidly produce point-of-use fibrous materials.

To overcome these limitations, techniques incorporating extrusion-based spinning, such as spinneret-based tunable engineered parameters technique (STEP)[97,98], rotary jet-spinning (RJS)[99,100,101,102], and touch-spinning[109] have emerged as alternatives to the established voltage- or temperature-dependent fiber manufacturing. These systems extrude polymer solutions to form nanofibers either via axial stretching and capillarity (STEP, touch-spinning) or viscous and centrifugal forces (RJS). While STEP and touch-spinning have been optimized to control the deposition and formation of high aspect ratio fibers, they do so at low production rates (550 rpm in STEP and 2500 rpm in touch-spinning). Also, the production of free-standing fibers using these techniques is difficult, as nanofibers are generally suspended along or collected on a fixed substrate. Previously, we developed a rotary jet-spinning system as a high-throughput nanofiber fabrication technique[99,100,101,102]. Unlike STEP or touch-spinning, RJS uses a high-speed (up to 75 000 rpm) rotating motor to extrude a non-woven nanofiber network from a micrometer-sized orifice. This method produces circumferentially aligned fiber networks and is amenable to a range of solvents and materials previously unexplored in fiber manufacturing[99,100,101]. However, a portable system is required for point-of-use nanofiber production.

We asked whether we could build a portable nanofiber manufacturing device that enables both high-speed fiber production and precise control of fiber orientation. In this chapter, we describe the design and utility of a nanofiber fabrication system termed pull spinning, which incorporates a high-speed (up to 45,000 rpm) rotating bristle that pulls a polymer solution from a static droplet

to a nanofiber. Specifically, the dependence of fiber radius and morphology on system parameters such as rotational speed, collector distance, and solution viscosity are investigated under ambient conditions. Ease of use and functionality are demonstrated for two proof-of-concept applications in muscle tissue engineering (natural precursor materials) and point-of-wear apparel (synthetic polymer materials). The capabilities of the pull spinning system will inform design and process choices in subsequent chapters.

1.2 Experimental Setup

1.2.1 Pull spinning apparatus

The pull spinning apparatus consists of a high-speed air-powered grinder (McMaster-Carr, Elmhurst, IL) with calibrated speeds up to 45,000 RPM. The pneumatic motor was regulated through a pressure gauge that enabled the direct read-out and calibration of the system under variable pressure. The collector may be, for example, two static posts fixed to a static base board or a rotating cylinder that functions as a spool to collect the fibers projected from the reservoir. The collector was connected to a DeWALT DC 720 1/2" cordless drill driver, operating at 1700 rpm.

1.2.2 Polymer materials

Combinations of polymers PCL (Mn 70,000-90,000; Sigma-Aldrich, St. Louis, MO), gelatin Type A (300 bloom; Sigma Aldrich, St. Louis, MO), Fibronectin (BD Biosciences, San Jose, CA), polyurethane (McMaster-Carr, Princeton, NJ), nylon (Nylon 6, Sigma-Aldrich, St. Louis, MO) and solvent 1,1,1,3,3,3-hexafluoro-2-propanol (Sigma-Aldrich, St. Louis, MO) were used in the fiber manufacturing experiments.

1.2.3 Fiber Image Analysis

Varying concentrations of polymers and proteins were spun onto fixed scanning electron microscopy stubs and imaged using a field emission scanning electron microscope (Carl Zeiss, Dresden, Germany). Samples were sputter coated using an Au target (Denton Vacuum, Moorestown, NJ) prior to imaging. All image analysis was done using ImageJ software (National Institutes of Health, Bethesda, MD). Between 150-450 fibers were analyzed (4-7 random fields of view per sample, 2-4 samples per condition). Percent beading was calculated by manually identified beads as individual regions of interest (ROIs). The area associated with the identified ROIs was then summed and the collective area was calculated as a function of total fiber area within a field of view. 2-D fast Fourier transform (FFT) analysis for nanofiber alignment was measured using the Directionality plug-in for Fiji (http://fiji.sc/Fiji, Ashburn, VA), according to previously established methods[110,111]. The Directionality plug-in calculates the spatial frequencies within an image given a set of radial directions. The method generated normalized histograms revealing the amount of fibers present between 0-180° with a bin size of 1°. Orientation order parameter (OOP) was calculated using a custom MATLAB plugin, according to previous studies[110]. A normalized OOP value of 0 represents an isotropic, random fiber network, and a value of 1 indicates a fully aligned, anisotropic fiber sheet.

1.2.4 Viscosity Measurements

Rheological measurements of varying solutions of polycaprolactone (PCL) were recorded using a viscometer (Model AR-G2, TA instruments, New Castle, DE) using a standard-size 40 mm cone and plate geometry. Measured viscosities were derived under steady state shear rates from 0.1 to 1000 s^{-1}.

1.2.5 Mechanical and Spectroscopic Characterization

Tensile properties of the fiber samples were measured in air using a uniaxial tension test (Instron 5566 mechanical tester, Norwood, MA). Before each measurement, the thickness and original length of the fiber sample was measured using a micrometer.

Infrared spectra of nanofiber samples were measured in air using Fourier transform infrared spectroscopy (Bruker Lumos FT-IR microscope, Billerica, MA) in attenuated total reflectance (ATR) mode. A resolution of 4 cm^{-1} and 16 scans was used.

1.2.6 Immunostaining and Image Analysis

Engineered tissues were fixed using 4% paraformaldehyde (Electron Microscopy Sciences, Hartfield, PA) and 0.5% Triton-X (Sigma-Aldrich, St. Louis, MO) for 5 min. Tissues were labeled with primary antibodies against sarcomeric α-actinin (Sigma-Aldrich, St. Louis, MO) or β3-tubulin (Sigma-Aldrich, St. Louis, MO), phalloidin (Life Technologies, Grand Island, NY), and 4',6-diamidino-2-phenylindole (DAPI) (Invitrogen, Carlsbad, CA). Immunostained samples were imaged using a Zeiss LSM 510 laser scanning confocal microscope.

1.2.7 Statistical Analysis

All error is reported as standard error of the mean (SEM). Analysis of variance (ANOVA) tests were used during statistical comparisons. For data that were not normally distributed, ANOVA on ranks followed by Dunn's or Tukey's pairwise comparison was used. *P*-values of less than 0.05 were used to measure statistical significance.

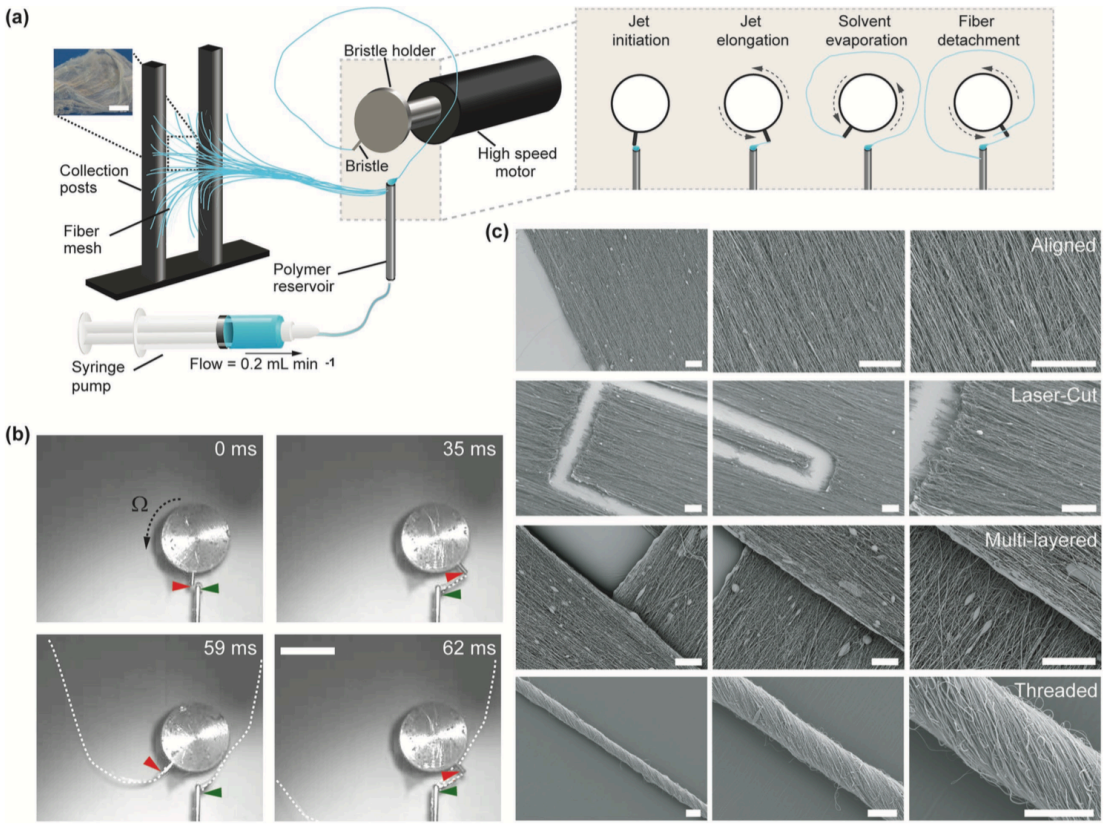


Figure 1.1: Design and function of the pull spinning system. a)Schematic of the pull spinning apparatus with a side view illustration of a fiber being pulled from the polymer reservoir. The pull spinning system consists of a rotating bristle that dips and pulls a polymer jet in a spiral trajectory. Scale bar: 100 mm. b) High-speed images capture the jet initiation as the bristle dips into a polymer droplet, jet elongation as the bristle pulls the droplet, solvent evaporation as the polymer jet solidi es, and fiber detachment from the bristle as the process begins again. The red arrow denotes the location of the bristle/fiber interface, the green arrow represents the location of the nozzle, and the dashed white line denotes a fiber formed throughout one revolution. Scale bar: 1 mm. c) Scanning electron microscopy images of various 6 wt%/vol% PCL:gelatin (3:1) scaffold structures and fiber alignments:aligned sheets (scale bars: 100 μm), laser cut cantilevers (scale bars: 200 μm), multilayered woven configurations (scale bars: 50 μm), and threads (scale bars: 50 μm).

1.3 Manufacturing Nanofibers Using Pull Spinning

The pull spinning system incorporates two components that work together to initiate nanofiber formation: a fixed polymer reservoir and a rotating bristle attached to a calibrated pneumatic motor (Figure 1.1a and Figure A.2). When the mandrel is rotated about its axis of symmetry and the bristle is in close proximity ($\sim$ 0.050 cm) to the reservoir, it dips and pulls an ejected polymer droplet into an elongated nanofiber. High-speed imaging captured during fiber formation suggests four stages: (1) initiation as the bristle contacts the polymer droplet, (2) elongation when the bristle pulls the polymer droplet into a jet, (3) solvent evaporation as the fiber solidifies during one revolution, and (4) detachment of the fiber from the bristle (Figure 1.1a,b). When the bristle is rotated at an angular speed (Ω) of 45,000 RPM, a polymer jet forms within 35 ms (Figure 1.1b). The extension of the jet as it is pulled by the rotating bristle is the most crucial stage of the process, without which fiber formation cannot be completed. This jet travels around the bristle holder in a spiral trajectory until one rotation is complete at 60 ms. Both ends of the fiber detach from the bristle at 60 ms as it draws a new droplet from the reservoir. The leading end of the fiber attaches to the reservoir below the droplet, while the trailing end continues rotating around the bristle holder until it travels toward the collector (Figure 1.1a,b). The resulting fibers can be collected across static posts or directly onto glass coverslips as aligned or threaded scaffolds, laser cut into custom configurations, or assembled as woven multilayered structures, illustrating the versatility of fibers generated using this process (Figure 1.1c).

The pull spinning apparatus consists of a bristle (length 0.531cm, diameter 0.1cm) that is fixed perpendicularly onto a rotating disk (0.877cm radius, S_0, Figure 1.2a). An external syringe pump fills the polymer reservoir at a constant rate of 0.2 mL/min. In this configuration, three variables dominate nanofiber formation: collector distance (R_c), angular speed of the bristle (Ω), and kinematic viscosity of the polymer solution (ν). We asked how these system parameters influence fiber radius

(r) and fiber morphology (% beading). First, R_c was varied on a $\log_2$ scale from 4 to 16 cm using a 6 wt%/vol% PCL solution in hexafluoro-2-propanol (HFIP), and fiber radius was measured at a constant Ω of 45,000 RPM (Figure 1.2b). Next, Ω was varied on a $\log_2$ scale from 8,000 to 32,000 RPM using the same 6 wt/v% PCL solution at fixed R_c of 10 cm (Figure 1.2c). We observe no significant differences in fiber radii under the various conditions, suggesting minimal dependence of fiber radius on collector distance and rotational speed within the specified ranges. The experiments were repeated using a 10 wt%/vol% nylon-6 solution in HFIP, and the same trend was observed (Figure A.3). Solution viscosity of PCL was varied, and fiber radius was measured at constant R_c of 10 cm and Ω of 45,000 RPM (Figure 1.2d-e). We observed that fiber radius increases significantly as a function of polymer concentration (Figure 1.2e). In spite of these trends, fibers exhibit less than 20% surface defects as evidenced by % beading along the fiber (Figure 1.2d). These findings were independent of collection time or polymer composition. We observed no significant changes in average fiber radius or % beading in 6 wt%/vol% PCL nanofiber samples collected after 1, 5, or 10 min of continuous fabrication (Figure A.4). Examination of nanofibers fabricated from a 6 wt%/vol% solution of PCL, polyurethane, or nylon further revealed fiber morphology to be smooth and uniform, without visible pores or defects at the sub-micrometer scale (Figure A.1). Collectively, these data suggest that while increasing solution concentration significantly increases fiber radius, variations in rotational speed, collector distance, or collection time do not over the ranges we tested.

1.4 Mechanism behind Fiber Formation

A previously reported scaling law describing jet extension using the RJS system elucidated how fiber formation is governed by a balance between viscous and centrifugal forces, where fiber radius scales with kinematic viscosity. Equation 1.1 describes this relation as[100]:

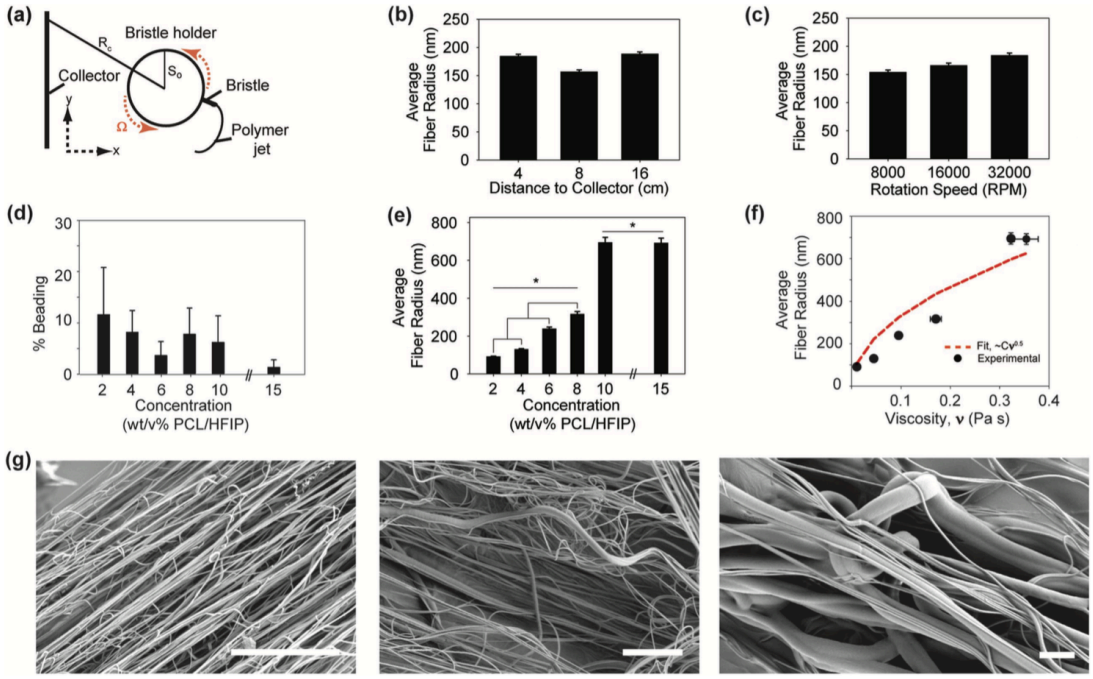


Figure 1.2: Characterizing structural properties of pull spun nanofibers and manufacturing system parameters. a) Side view of fiber being pulled using bristle rotating at speed Ω. R_c is collector distance ($\sim$10 cm), and S_o is the radius (0.877 cm) of the bristle holder. b) Radius of 6 wt%/vol% PCL fibers measured as a function of the distance to the collector (cm). Fibers were produced at a constant Ω of 45,000 RPM. c) Radius of 6 wt%/vol% PCL fibers measured as a function of the motor rotation speed (RPM). Fibers were spun at a constant R_c of 10 cm. d) Percent beading as a function of concentration of PCL in HFIP. e) Fiber radius as a function of polymer concentration. f) Identifying system parameters with varying concentrations of PCL in HFIP (2–15 wt%/vol%). Fiber radius measured as a function of viscosity and best fit by $\sim C\nu^{1/2}$, where $C = 1050.4$ m^2 s^1. g) Scanning electron images of nanofibers from PCL spun at 2 wt%/vol% in HFIP, 6 wt%/vol% in HFIP, and 15 wt%/vol% HFIP, respectively. Scale bars: 1000 nm. In all graphs, N is at least 200 fibers across four samples for each condition. Error reported as SEM. * indicates p <0.05.

$$r \sim \frac{aU^{1/2}\nu^{1/2}}{R_c^{3/2}\Omega} \tag{1.1}$$

In this expression, a is the initial jet radius, U represents the angular jet velocity, ν is the kinematic viscosity of the solution, R_c is the collector distance, and Ω represents the angular speed of the RJS polymer reservoir. We asked whether similar parameters can be applied to describe the pull spinning process. Pull spinning propels a polymer jet in a linear trajectory from a reservoir to a collector. Under these conditions, a, U, R_c, and Ω are fixed parameters. However, the reservoir is static, unlike the rotating one in RJS. In this configuration, the jet is pulled and projected toward one primary direction, and fiber formation occurs within a narrow time frame as centrifugal force is applied (0-60 ms at Ω = 45,000 RPM). In this time scale, centrifugal force is proportional to the bristle radius but vanishes beyond one rotation cycle because the fiber detaches from the bristle (Figure 1.1a,b). This suggests that the fiber thinning process ceases before the nanofiber is projected toward the collector. Experimentally, we observed that the maximum collector distance at which 6 wt%/vol% PCL nanofibers could be spun was 29 cm. ANOVA indicated that the average radius of these fibers (125.01 $\pm$ 7.22 nm) was not statistically different from that of fibers tested at closer ranges (Figure 1.2b). Thus, the distance between pull spinner and collector has a negligible effect on fiber radius for the given polymer concentration (Figure 1.2b).

Increasing solidification speed has been shown to increase fiber radius and to mitigate bead formation in the RJS system[102]. The use of a pneumatic motor in the pull spinning system introduces an external air flow to facilitate the fiber solidification process. Increasing angular velocity of the bristle results in two competing effects: a larger centrifugal force that accelerates fiber thinning and a higher air flow that hastens fiber solidification rates, thus slowing fiber thinning. These two processes cancel each other, and the change in fiber radius as a function of angular speed is negligibly

small, even as Ω increases fourfold (Figure 1.2c). One factor that does directly correlate with fiber radius is solution viscosity, which reduces the rate of fiber thinning and increases with polymer concentration (Figure A.5 and Figure 1.2e). The scaling relation between the fiber radius and the kinematic viscosity has been derived in the previous model for the RJS system as $r = C\nu^{1/2}$, where C is a dimensional constant with units of $(m^2\ s^1)$[100]. The constant C for the pull spinning system can be fit from the experimental relation between radius and viscosity (Figure 1.2f and Figure A.5), demonstrating that increasing solution viscosities contribute to larger nanofiber radii (Figure 1.2g) reported within the specified range.

1.5 Quantifying Anisotropy of Pull Spun Nanofibers

Point-of-use fiber production for biomedical and textile applications requires the capability to control nanofiber orientation. Previous force spinning methods utilized centrifugal force to regulate fiber orientation and anisotropy[101]. Electrospinning techniques decrease jet instability and control deposition by adjusting the electrode setup, collecting fibers between fixed plates, or minimizing distance between spinneret and collector[104,125,126,127]. However, significant decreases in throughput or disruption of fiber morphology can occur due to residual charge buildup, low collection speed, insufficient solvent evaporation, applied voltage, or polymer flow rate[108,127,128]. A comparison of these techniques, along with other nanofiber fabrication systems, is further summarized in Table 1.1.

We asked whether pull spinning is capable of generating free-standing anisotropic nanofibers in the absence of an underlying substrate or rotational collector. PCL nanofibers of various concentrations (6, 8, and 10 wt%/ vol% in HFIP) were collected in air at a distance of 10 cm from the bristle. Network fiber anisotropy was quantified by calculating OOP using a custom MATLAB script; OOP is a normalized parameter, in which 0 represents an isotropic network and 1 indicates a fully aligned sheet[110,129]. Nanofibers of all three polymer concentrations displayed OOP values

above 0.96, indicating the formation of free-standing, highly aligned nanofiber networks (Figure A.3c). While certain near-field[103,116,117] or capillary force-based[98,97,109] fiber manufacturing methods also provide control of nanofiber spacing and deposition, pull spinning generates highly aligned fiber scaffolds with increased throughput and scalability (details listed in Table 1.1). Although the production rate of pull spun nanofibers (0.15 g h^{1} for 6 wt%/vol% PCL/HFIP) does not equal that of previously established gyratory (6000 g h^{1})[119,120] or centrifugal force-based (60 g h^{1})[99,118] methods, fibers produced using this technique demonstrate greater alignment. Thus, pull spinning represents a balance between fiber production rate and precise control of fiber anisotropy.

1.6 Fiber Muscular Thin Films Support Contractility Measurements

Given the capability of the pull spinning system to rapidly manufacture anisotropic fiber scaffolds, we asked whether these fibers could be used to build a functional *in vitro* contractility assay to direct muscle formation and to support function of smooth and skeletal muscle. Previously reported muscular thin films (MTFs) have demonstrated the ability to model the structural and functional changes that occur in cardiomyopathy and allergic asthma, using hiPSCs and human-derived primary airway smooth muscle, respectively, and expand capabilities for drug evaluation[129,130,131]. However, these models are limited to formation of monolayer tissues on 2D polymeric thin films. Quantification of skeletal muscle contractility on a biomimetic nanofibrous substrate has not yet been demonstrated. Using the pull spinning system, we built anisotropic scaffolds (OOP, 0.95) composed of 6 wt%/vol% PCL:gelatin (75:25 in HFIP), a polymer:protein biohybrid known to promote proliferation and maturation of muscle tissue[101]. The scaffolds, termed fiber muscular thin films (fMTFs), were collected on 22 × 22 mm^2 glass coverslips, bound to the edges of the coverslip surface with PDMS, and laser engraved into cantilevers. In this configuration, one end of the cantilever remains anchored to the glass coverslip while the other end is free such that muscle contraction elic-

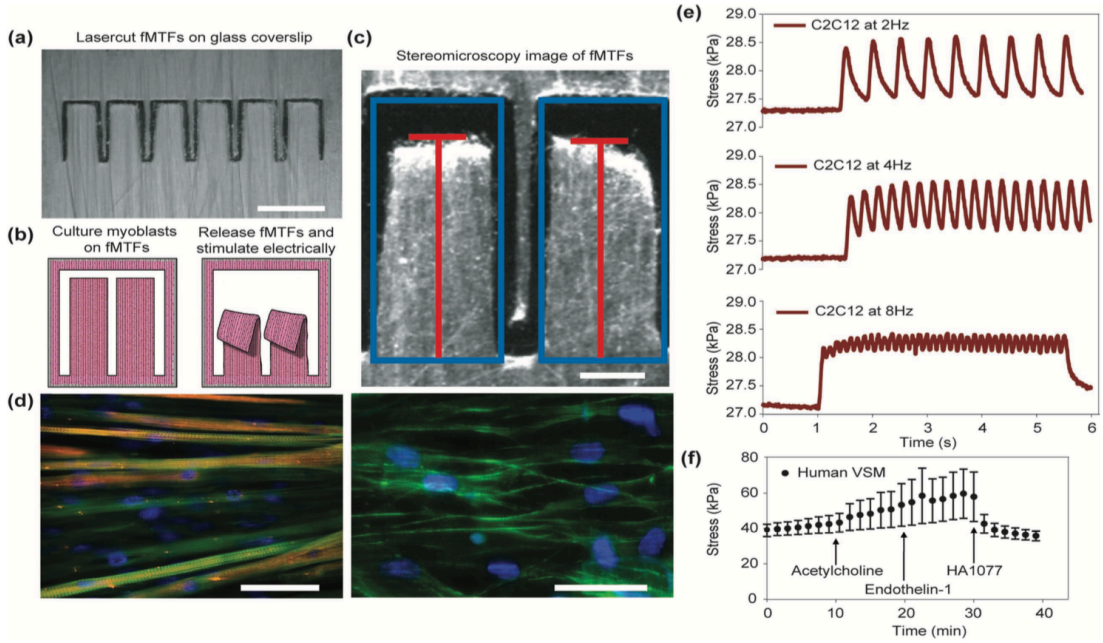


Figure 1.3: Proof-of-concept use of fiber muscular thin films (fMTFs) for *in vitro* functional testing of muscle tissue. a) Stereomicroscopy image of laser cut 6 wt%/vol% PCL:gelatin (75:25) fMTFs on a glass coverslip. Scale bar: 4 mm. b) Schematic of myoblasts cultured on fMTFs, subsequently released and stimulated electrically. Muscle contraction bends the cantilevers. c) Stereomicroscopy image of fMTF cantilevers. Blue lines indicate fMTF borders prior to their release from the glass coverslip. Horizontal red lines indicate the leading edge positions of the fMTFs during contraction. Scale bar: 500 μm. d) Immunofluorescence staining of murine skeletal muscle (left) and human vascular smooth muscle (right), cultured on fMTFs. Nuclei are stained blue (DAPI) and F-actin is stained green (Phalloidin 488) in both tissues. In murine skeletal muscle tissue, α-actinin is also stained red. Scale bars: 50 μm. e) Stress readouts from an fMTF cultured for 10 days in DMEM at various pacing frequencies: 2, 4, and 8 Hz. f) Stress trace of human vascular smooth muscle fMTFs serially treated with 10×10^6 m Acetylcholine after 10 min, 500×10^9 m Endothelin-1 after 20 min and 100×10^6 m HA1077 after 30 min. N = 1 chip, 6 films. All errors are reported as SEM.

its film bending (Figure 1.3a,b). fMTFs were fabricated through the following procedure: (1) thin semi-cured polydimethylsiloxane (PDMS) films were deposited on two ends of a glass coverslip, (2) PCL:gelatin (75:25, 6wt/v%) nanofibers were spun and collected on the coverslip, (3) fMTF cantilevers were cut using a CO_2 laser prototyping system (Epilog Laser, Golden, CO) with 3% power and 6% speed settings, (4) muscle cells were cultured for a desired time, and finally (5) fMTFs were released and electrically stimulated. The thickness of fMTFs was measured using an optical profiler (Veeco Wyko NT1100, Edina, MN).

Seeded with a murine myoblast cell line (C2C12; please see Appendix A for detailed protocol), the fMTFs supported myoblast fusion and maturation into functional muscle tissue, enabling measurable dynamic stress values with quantifiable twitch and tetanus curves (Figure 1.3c–e and Figure A.6). Immunofluorescence staining of α-actinin further confirmed the contractile phenotype of the engineered muscle tissue (Figure 1.3d).

Next, we asked whether the fMTFs could also be utilized to quantify the slow, sustained contraction, and relaxation of primary human vascular smooth muscle. Nanofiber scaffolds were seeded with human vascular smooth muscle and monitored over 4 days *in vitro* (Figure 1.3d). Our results indicated an increase in contractile stress when treated with the known vasoconstrictors acetylcholine and endothelin-1. Additionally, the engineered human vascular smooth muscle relaxed in response to rho kinase inhibitor HA1077 (Figure 1.3f). Both muscle cell types exhibited an extended morphology, proliferating along the fiber axis (Figure 1.3d). Collectively, these data demonstrate the ability of pull spinning to manufacture highly anisotropic, biocompatible fibrous scaffolds that recapitulate native muscle structure and function by supporting and directing the formation of engineered smooth and striated muscle.

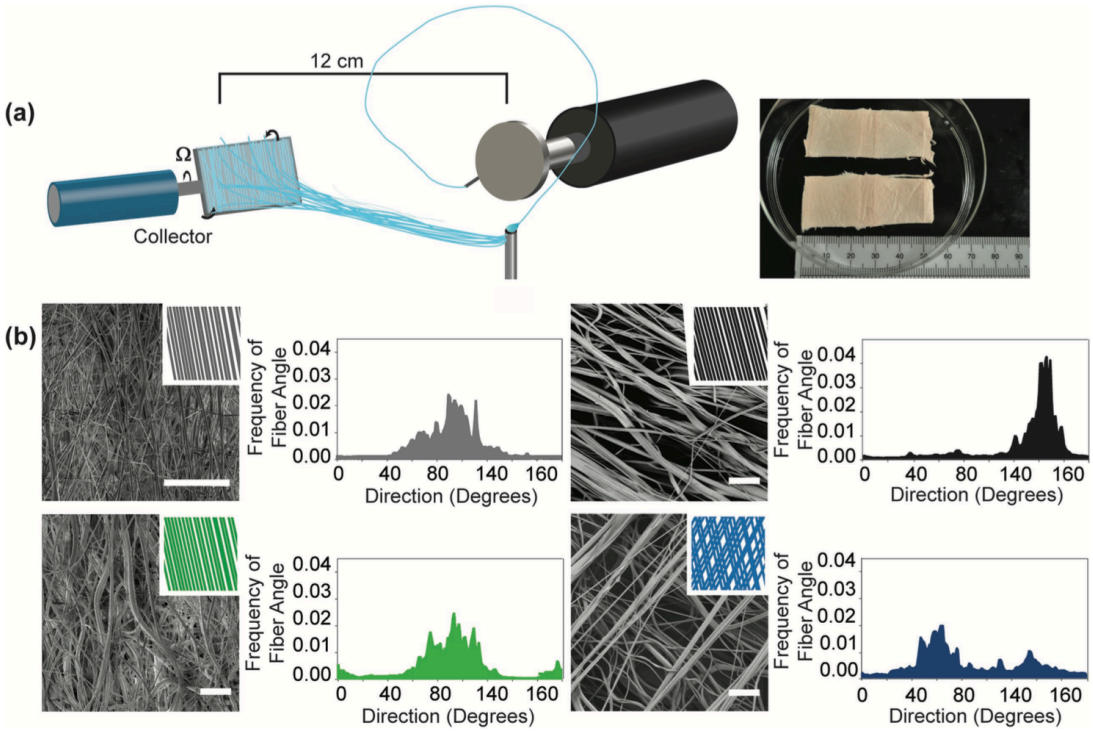


Figure 1.4: Pull spun nanofibers for proof-of-principle apparel design. a) Schematic of collection scheme and sample of 5:5 wt%/vol% polyurethane (PU):nylon (1:1) nanofiber swatches collected after pull spinning. b) Scanning electron images and histograms representing the fiber angle (alignment) as a function of the frequency of the angle of 10 wt%/vol% nylon (gray), 10 wt%/vol% PU (black), 5:5 wt%/vol% anisotropic PU:nylon (green), and 5:5 wt%/vol% PU:nylon crosshatched nanofibers (blue). A multimodal distribution denotes an isotropic mesh, whereas a unimodal distribution indicates uniaxial fiber alignment (N = 3–5 fields of view over two samples). Scale bar: 20 μm.

1.7 Nanofiber Anisotropy Influences Material Performance

Having demonstrated the capability of the pull spinning system to produce anisotropic nanofibers for tissue engineering, we asked whether fiber orientation impacts material properties in the context of apparel design. To test this, we built nonwoven nanofiber networks composed of 10 wt%/vol% nylon-6, 10 wt%/vol% polyurethane (PU), and a 5:5 wt%/vol% PU:nylon blend along a rotating collector (Figure 1.4a). Polyurethane and nylon were selected based on their widespread use in performance athletic wear[132]. The collector consisted of a drill driver attached to a metal rod terminated by a glass slide. The glass slide permitted continuous collection and facilitated control over fiber orientation, yielding reproducible network thicknesses of 220 ± 29 μm (N= 17). After a 15 min pull-spinning cycle, networks of nonwoven fibers were removed from the mandrel and analyzed using bright field (Figure 1.4a) and scanning electron microscopy (SEM, Figure 1.4b). Network isotropy of 5:5 wt%/vol% PU:nylon samples was manually varied by adjusting collection angles to produce anisotropic and crosshatched patterns (Figure 1.4b). Fiber alignment in the networks was quantified using Fast Fourier Transform (FFT) to measure preferred orientation of structures across multiple fields of view in both x and y directions[133,134]. FFT decomposes an image into constituent sine waves by considering the intensity of pixels to be signal intensity and the displacement in the x and y axes to be the frequency component. The output of this operation describes the intensity of the sine waves with specific frequencies in the Fourier transform; this information can be used to map the spatial information within an image and to provide insight on the patterns within it. In this study, FFT is a metric for fiber anisotropy, wherein a histogram with a narrow, unimodal peak represents perfectly aligned fibers, and the abundance or lack of peaks represents a completely isotropic sample. In our analysis, fibers that are collected as aligned networks have a unimodal histogram; whereas, samples collected in the crosshatched configuration display a bimodal distribution, representing two directions of fiber orientation (Figure 1.4b). These data suggest that pull spinning onto an ad-

justable collector at different angles can produce fibrous networks with distinct orientations. Unlike previous electrospinning techniques that have been used to control nanofiber orientation, pull spinning does not require additional devices such as auxiliary[104] or parallel[135] electrodes, perforated collectors[136], or controlled electrode geometries[137] to induce fiber alignment during deposition.

We then asked how fiber orientation and composition affect the bulk mechanical properties of nanofiber networks. Fiber networks were uniaxially loaded at a constant rate of 8 mm min^{1} until failure. The ultimate tensile strength (UTS, Figure 1.5a) and strain at failure (Figure 1.5b) for each of the four conditions are reported under tensile load. 5:5 wt%/vol% PU:nylon was the strongest material tested, exhibiting a UTS of 2.63 ± 0.19 MPa and strain at failure of 0.73 ± 0.06. The cross-hatched 5:5 wt%/vol% PU:nylon nanofabric displayed significantly lower ultimate tensile strength than the anisotropic 5:5 wt%/vol% PU:nylon sample. In contrast, low UTS (0.19 ± 0.01 MPa) and strain at failure (0.18 ± 0.02) values for the 10 wt%/vol% nylon networks suggest that nylon is the least resistant of the tested networks to mechanical load. The nylon fibers are also the thinnest, with an average radius that is nearly 40% less than that of the other samples (Figure 1.5c), suggesting that fiber structure and composition may contribute to bulk mechanical properties.

To further understand the role of molecular structure in bulk tensile strength, we used ATR-FTIR spectroscopy to examine the structural changes in the fiber networks as a function of polymer composition (Figure 1.5d). Characteristic vibration modes of both nylon and PU are evident in the spectra (Table A.1, Appendix A). Our analysis focused on the vibration peaks indicative of hydrogen bond formation— a sign of intrachain bonding. These peaks are represented by amide and carbonyl stretches: 1637 cm^{1} (amide I), 1547 cm^{1} (amide II), 1729 cm^{1} (carbonyl), and 3300 cm^{1} (amide). Hydrogen bonding between amide groups of nylon and urethane linkages of PU increases bulk tensile strength by reducing slippage between the anisotropic polymer chains. The increase in hydrogen bond formation is indicated by amide and carbonyl peak broadening and a downshift of N−H and C=O stretching (Figure 1.5d, black lines). Overall, the frequency peak positions of the IR data for

the three polymer compositions suggest that blending PU and nylon increases hydrogen bonding within the formed fibers. These interactions manifest on the macroscale through stronger tensile strength for the anisotropic 5:5 wt%/vol% PU:nylon blend. These data are compared against drop cast films of similar compositions (Figure 1.5d, red lines). Comparing the vibration modes of the cast films to those of the polymerized pull spun nanofibers reveals significant increases in hydrogen bonding after pull spinning (Figure 1.5d), further suggesting the role of this process in forming intrachain bonds.

Collectively, these data suggest that pull spinning can be used to fabricate point-of-use nanofibers whose mechanical performance can be customized according to the composition and structural properties of the starting material. This capability will enable us to tune fiber performance specific to a final material application, such as producing fabric on demand, reinforcing soft lithographic structures on the micro-scale, and directing motion of soft robotic structures by selectively limiting strain.

1.8 Point-of-Use Apparel Fabrication

A simple proof-of-principle application of the pull spinning system for apparel was demonstrated using the strongest tested polymer material, the 5:5 wt%/vol% PU:nylon blend, spun directly onto the knee joint of a 30 cm doll (Figure 1.5e). The knee was selected as an ideal trial area based on its high range of motion and nonuniform topography. We found that the nanofibrous textile conformed to the shape of the joint during pull spinning, demonstrating no delamination following fiber formation. The joint was extended from 0° to 135° through the full range of motion. The rate at which the knee is flexed was varied from 1 to 200 extensions min^{1}. Regardless of the rate of deformation, the nanofiber network remained intact during joint movement, exhibiting no tearing (Figure 1.5e). This preliminary trial suggests that pull spinning is a viable fabrication tool for point-of-

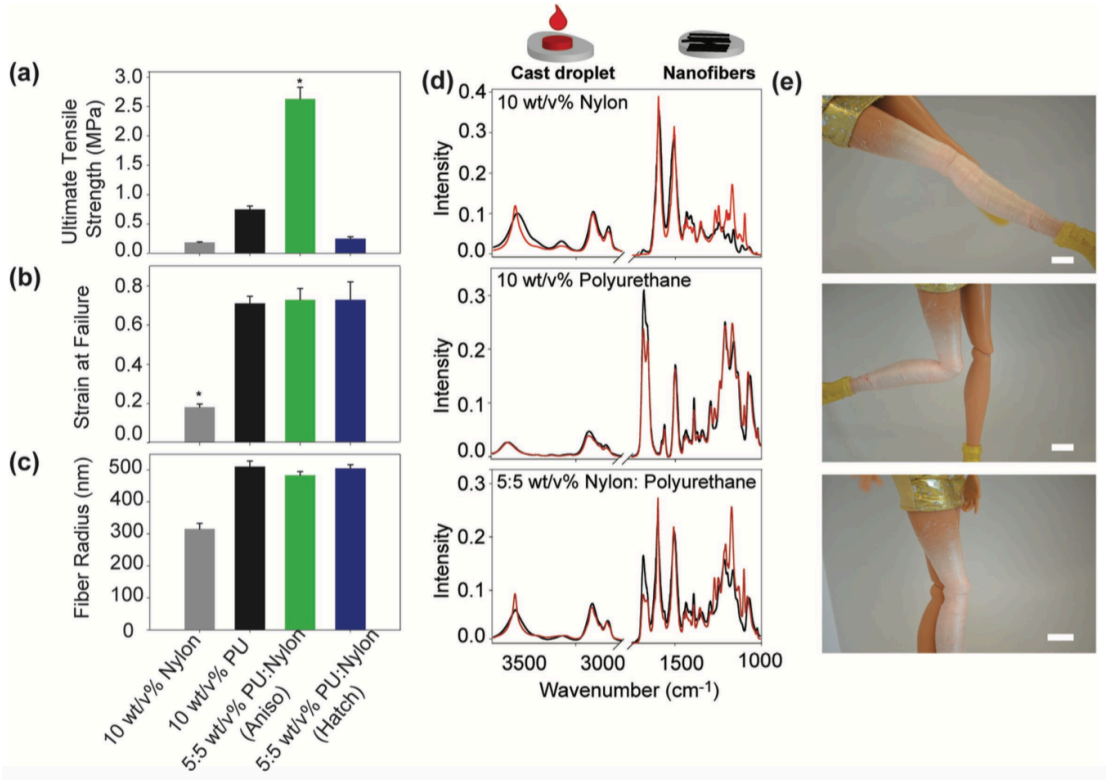


Figure 1.5: a) Ultimate tensile strength and b) strain at failure of each nanofiber network measured under tension. c) Fiber radius measured from SEM images (N = 200 fibers over four samples). d) ATR spectra of solution cast (red lines) polymer films and pull spun nanofibers (black lines). Data are averaged for n = 2 production runs per composition, with 4-6 FOVs per sample. e) Proof of concept demonstration of point-of-use apparel: a nylon/PU fiber network pull spun directly onto the knee joint of a 30 cm doll. Scale bars: 1 cm. All error is reported as SEM. * indicates $p < 0.05$.

wear manufacturing and for robotic actuation systems, which must sustain numerous cyclic strain cycles and large deformation motions without delamination.

1.9 Summary

In this chapter, we presented a compact nanofiber fabrication system that rapidly generates continuous anisotropic nanofibers independent of external system parameters. Like other well- established techniques, pull spinning works by extruding a polymer or protein droplet into a solid nanofiber that can be collected as single fiber-thick layers or as a nonwoven network on a static or rotating substrate. Unlike other processes, pull spinning is a "point-and-shoot" method that facilitates high-speed nanofiber fabrication while maintaining control of fiber orientation (OOP >0.96) and deposition. We highlighted two proof-of-concept applications for tissue engineering and textile design, illustrating the versatility of the pull spinning system for nanomaterials manufacturing. Moreover, we demonstrated the effect of rotational speed, collection time, collector distance, polymer concentration, and composition on the radius and morphology of pull spun polymer nanofibers. Further, we analyzed the structural, chemical, and mechanical properties of centrifugally spun polymer nanofibers. We adapted a scaling law to describe how centrifugal force and kinematic viscosity influence nanofiber formation, and established upper and lower limits for fiber radius based on solution viscosities. In the next chapter, we will further apply this knowledge of nanofiber formation kinetics to investigate strategies for multi-material nanofabric manufacturing.

Table 1.1: Comparative advantages, limitations, and nanofiber formation mechanisms for several state-of-the-art nanofiber manufacturing processes, including pull spinning, electrospinning (ES), and melt spinning

Process	Mechanism	Production Specifications	Output [g h^{-1}]	Process Advantages	Process Limitations	Ref.
Pull spinning	Axial, rotational stretching	45,000 rpm	0.15	Portable; Point-of-use fabrication; Amenable to wide range of polymers; High throughput; Control of fiber orientation; Ease of use	Lower throughput than previous force spinning processes	112
ES	Electric field	<30 kV	0.01 - 0.1	Amenable to wide range of polymers	Low throughput; Requires high V power supply; Alignment not inherent to process (additional tools required)	104,113,114,115
Near field ES	Electric field	0.2 – 1.8 kV	N/A	Amenable to wide range of polymers; Precise control of fiber alignment and deposition	Low throughput; Requires high V power supply; Short distance to collector impedes fiber solidification	103,116,117
Rotary jet (force) spinning	Centrifugal force	Up to 75,000 rpm	60	High throughput; Amenable to wide range of polymers; Ease of use	Bench-top system: not easily portable; Fibers formed circumferentially; Requires post-processing for use as scaffolds	99,102,101,118
STEP	Capillary force	550 rpm	N/A	Performs in air; Formation of high aspect ratio fibers; Precise control over fiber spacing	Low-throughput, based on production rates; Not easily scalable	97,98
Touch spinning	Axial stretching	500-2500 rpm	N/A	Amenable to wide range of polymers; Performs in air; Control of fiber orientation, Ease of use	Low throughput, based on production rates	109
Brush spinning	Axial stretching	3000 rpm	N/A	Performs in air; Control of fiber orientation, Ease of use	Removing sheets from brush may damage loose fibers; Requires post-processing for use as scaffolds	109
Pressurized gyration	Centrifugal force, solution blowing	Up to 35,000 rpm	6000	High production rate	Gas pressure contributes to fiber elongation; Requires volatile solvents	119,120
Pressurized melt gyration	Centrifugal force, high temperature	Up to 36,000 rpm	N/A	Eliminates dependence on volatile solvents; Crystalline polymers formed using gyration technique	Requires high temp.; Unsuitable for biopolymers; Limited to microfiber production	121
ES Rapid Prototyping	Electric field	3.2 kV	N/A	Amenable to wide range of polymers; Precise control of fiber deposition and orientation	Requires high V power supply; Vibration of collector affects fiber morphology; Incomplete fiber solidification between layer deposition distorts fiber morphology	108
Centrifugal melt spinning	Centrifugal force, high temperature	11,000-13,630 rpm	N/A	Amenable to wide range of polymers; Eliminates dependence on volatile solvents	Unsuitable for biopolymers	122
Gas jet nanofibers	Axial stretching, gas blowing	N/A	0.09-8.6	Scalable process is amenable to multiple fiber morphologies	Low production rate; Requires volatile solvents for nanofiber formation	123
Melt ES	Electric field, high temperature	5-100 kV	12.5	Highly uniform and reproducible fiber diameters	Unsuitable for biopolymers; Only applicable for nonconductive polymers	106,115,122,124
Direct write melt ES	Electric field, high temperature	Up to 12 kV	N/A	Control over fiber deposition and orientation; Produces complex multilayered structures	Requires high V power supply; Lag between jet and collector speed yields errors over time; Unsuitable for biopolymers; Limited to microfiber production	106

2

Fabricating Multi-Material Nanofabrics using Rotary Jet Spinning

2.1 Introduction

Nanofiber composite textiles based on two or more distinct fiber types would facilitate tuning material, physical, and chemical properties, and combining base materials that require the use of im-

miscible solvents. On the microscale, reinforcing fibrous constructs with fibers of disparate elastic moduli is used to control the elastic modulus (resistance to elastic deformation) and toughness (ability to absorb energy without fracturing) of the composite structure[138,139]. Integrating multiple types of polymer fibers at the nanoscale will enable the development of scaffolds whose toughness and elasticity can be easily regulated through material selection and the ratio of components.

However, current fiber fabrication techniques are challenged by applications requiring multiphase nanotextiles or orthogonal solvents. Recent approaches to fabricating multi-material nanotextiles are either limited to adjoining biphasic (Janus-type) fibers[140], constrained by charge interference from adjacent spinnerets[141], or produce highly delineated sheets rather than well-integrated multimodal textiles[142]. These arrangements limit customizability of the final nanofabric by requiring the use of similar solvents and processing parameters for both solutions[143]. The centrifugal force-based rotary jet spinning (RJS) system has the potential to overcome these limitations by eliminating the reliance on electric fields for fiber formation and reducing the number of processing parameters[66,99,102].

In this chapter, we describe the fabrication of tough multi-material polymer nanofabrics using a custom-designed dual chamber RJS reservoir. We study the influence of reservoir chamber and nanofabric composition on fiber structural and mechanical properties, respectively. Our results show that composite multi-material nanofabrics are tougher than either individual component, as well as single fiber blends of both materials. Further, both polymers are heterogeneously distributed across a composite nanofiber sheet. Finally, we demonstrate that this method can be used to manufacture multi-modal nanotextiles from distinct polymers that require the use of orthogonal solvents.

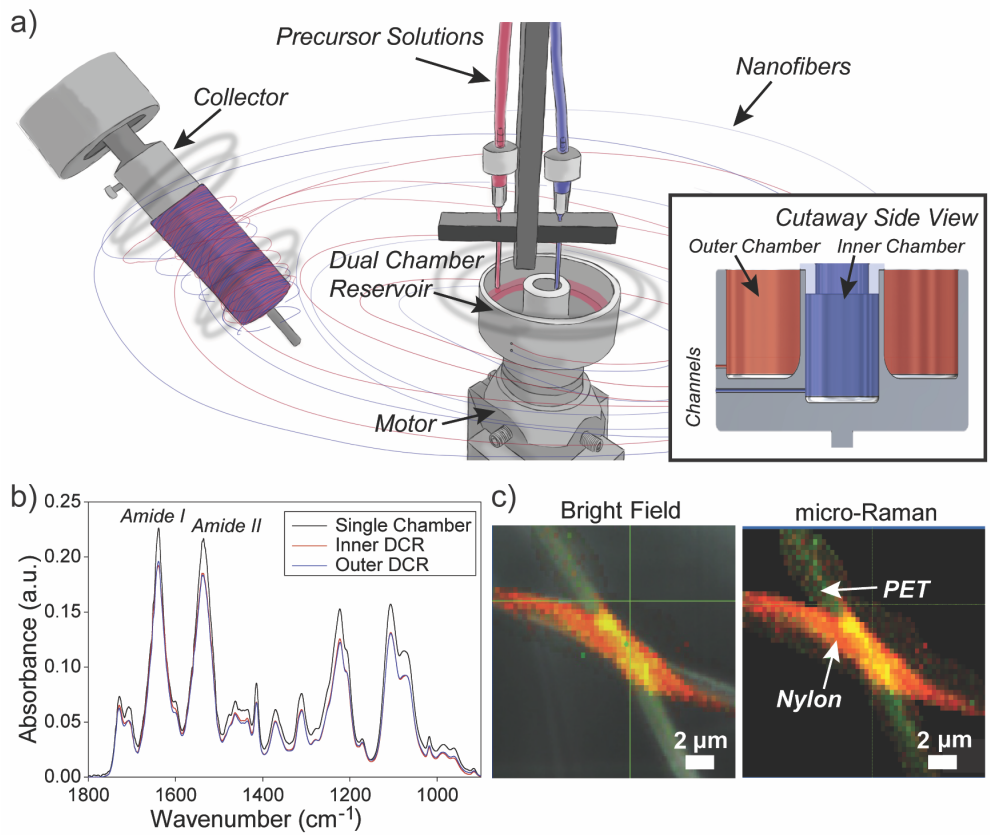


Figure 2.1: a) Illustration of multi-material nanofabric fabrication using rotary jet spinning (RJS) and the dual chamber reservoir (DCR). Inset: Cutaway side view of the DCR. Inner and outer chambers are denoted in blue and red, respectively. b) FTIR spectra of single and dual chamber nanofabrics. Data are averaged for n = 3 production runs per condition, with 16 random FOVs per sample. c) Bright field with spectra overlay and micro-Raman images displaying distinct nylon and PET nanofibers. The nylon and PET nanofibers are indicated in red and green, respectively.

2.2 Experimental Setup

2.2.1 Materials

Precursor solutions for nanofiber fabrication were prepared by dissolving nylon (Nylon 6, Sigma-Aldrich, St. Louis, MO), polyurethane (Lubrizol, Cleveland, OH) and/or polyethylene terephthalate (PET, McMaster-Carr, Princeton, NJ) in 1,1,1,3,3,3-hexafuoro-2-propanol (Sigma-Aldrich, St. Louis, MO). Poly(vinylidenefluoride-co-trifluoroethylene) (PVDF-TrFE, Sigma-Aldrich, St. Louis, MO) solutions were prepared using dimethylformamide (DMF, Sigma-Aldrich, St. Louis, MO) and acetone (Avantor Performance Materials, Center Valley, PA) as solvents.

2.2.2 Reservoir Design and Fiber Fabrication

The RJS system consists of a brushless DC servo motor (Maxon Motor Company, Fall River, MA) attached to a custom-designed aluminum reservoir rotating at 30,000 RPM. The single chamber reservoir contains one 340 μm sidewall orifice. The dual chamber reservoir (DCR) consists of two concentric cavities, each containing a 500 μm aperture. Infusion rate of precursor solutions into the reservoir was regulated using an external syringe pump. All solutions were infused at a constant rate of 5 mL min^{-1}. Fibers were collected on a rotating cylindrical collector (3000 RPM) mounted on a linear motor.

2.2.3 Fiber Image Analysis

Various concentrations of polymer nanofibers were sputter coated using a Au target (Denton Vacuum, Moorestown, NJ), and then imaged using a field emission scanning electron microscope (Carl Zeiss, Dresden, Germany). Image analysis was performed using ImageJ software (National Institutes of Health, Bethesda, MD). 300 fibers were analyzed, including 4 random fields of view (FOVs) per

sample and 3 samples per condition.

2.2.4 Mechanical Characterization of Fibers

A uniaxial tension test (CellScale BioTester, Waterloo, ON, Canada) was used to measure the mechanical properties of nanofiber sheets in air. Prior to each test, the thickness, width, and gauge length of the fiber sample were recorded using a micrometer.

2.2.5 Spectroscopic Nanofiber Analysis

Infrared spectra of nanofabric samples were recorded in air using Fourier transform infrared spectroscopy (Bruker Lumos FTIR microscope, Billerica, MA) using the attenuated total reflectance (ATR) technique. A resolution of 4 cm^1 and 16 scans was used for both local spectra sampling and 2D contour mapping. For contour mapping, data was normalized to maximum intensities.

Raman spectra of nanofiber samples were acquired in air using a confocal Raman microscope (LabRAM HR Evolution, Horiba Scientific, Edison, NJ). A 532 nm Ar-ion laser was used to excite the sample with a 100x objective. The spectra were processed using LabSpec 6 software.

2.2.6 Statistical Analysis

All error was reported as standard error of the mean (SEM). Analysis of variance (ANOVA) tests were performed during statistical comparisons. *P*-values below 0.05 were considered statistically significant.

2.3 Fiber Structure Conserved across Reservoirs

We developed a dual chamber reservoir (DCR, Figure 2.1a) to fabricate multi-material nanofabrics using rotary jet spinning. The reservoir contains circular (inner) and annular (outer) compartments,

which are separated and vertically offset to prevent solution mixing (Figure 2.1a, inset). The sidewall apertures of the two chambers are aligned vertically relative to each other to limit contact of nanofiber jets during fiber fabrication. Precursor solutions of nylon-6 and polyurethane (PU) in 1,1,1,3,3,3-hexafluoro-2-propanol (HFIP) were simultaneously infused into the DCR and were continually fed during fiber manufacture. (Figure 2.1a). During high speed reservoir rotation, centrifugal force propels each solution through its respective orifice. As these polymer jets elongate and the volatile solvent evaporates, two discrete nanofibers are formed and accumulate on a rotating collector (Figure 2.1a).

First, we asked whether the choice of DCR chamber (inner or outer) influenced nanofiber structure, and whether these fibers differed from those fabricated by the single chamber reservoir used in previous RJS studies[99]. A blended 5 wt/v% nylon / 5 wt/v% PU solution was injected individually into the inner and outer DCR chambers. Fourier transform infrared spectroscopy (FTIR) was used to assess the structural properties of polymer nanofibers as a function of the DCR fabrication process. Vibrational peaks corresponding to both nylon (Amide I, 1641 cm^{-1}) and PU (Amide II, 1547 cm^{-1}) are evident in the spectra recorded for nanofibers fabricated using both chambers (Figure 2.1b). No peak shifts are observed between spectra acquired for the inner and outer chambers, indicating no significant differences between the structure of polymer nanofibers fabricated using either compartment. Further, FTIR verified that DCR fiber fabrication does not significantly affect the structural properties of nylon/PU nanofabrics, in comparison with the conventional single chamber reservoir (Figure 2.1b).

In a similar test, a multi-material nanofabric was manufactured by simultaneously infusing a 10 wt/v% nylon solution into the inner DCR chamber and a 5 wt/v% PET solution into the outer chamber, both using HFIP as the solvent. Micro-Raman spectroscopy confirmed that both nylon and PET nanofibers were independently present in a composite multi-material nanofabric (Figure 2.1c). Collectively, these results indicated that fiber formation was consistent across both channels,

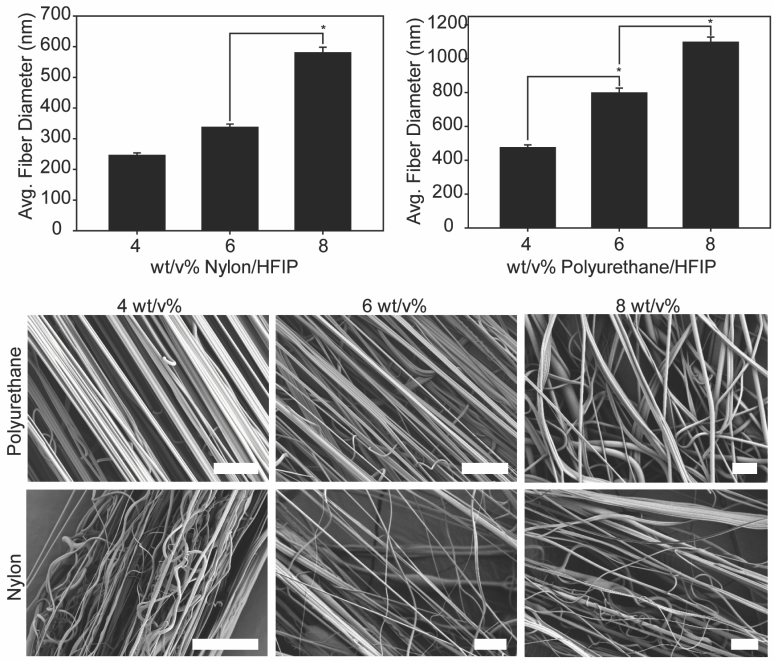


Figure 2.2: a) Average diameter and b) Scanning electron images of nylon and polyurethane nanofibers spun at 4 wt/v%, 6 wt/v%, and 8 wt/v% in HFIP. Data are averaged for n = 3 production runs per condition, 3 samples per run, and 300 fibers across 4 FOVs. * indicates $p < 0.05$. All scale bars: 10 μm.

no structural artifacts were introduced during chamber selection, and distinct polymer nanofibers were produced from each chamber.

2.4 Fabric Composition Influences Material Mechanics

We then investigated the impact of nanofabric composition on network mechanical properties by comparing the toughness and specific elastic modulus of multi-material, blend, and single-component polymer nanofibers. Nylon and polyurethane were selected for this analysis based on the significant difference between their elastic moduli. First, the concentration of nylon and PU solutions was varied from 4 to 8 wt/v% in HFIP in increments of 2 wt/v%, and nanofiber diameter was measured for each condition (Figure 2.2a-b). Next, multi-material nanofabrics were manufactured by infusing a

6 wt/v% PU solution into the inner DCR chamber, and a 6 wt/v% nylon solution into the outer chamber. Single fiber polymer blends were fabricated by mixing nylon and PU into one 6 wt/v% solution. As a control, pure 6 wt/v% nylon and pure 6 wt/v% PU nanofibers were each spun individually using the outer and inner DCR compartments, respectively. The samples were loaded uniaxially until failure at a constant elongation rate of 8 mm min^{-1}.

Multi-material nylon/PU nanofabrics manufactured using this technique are tougher than either material alone (Figure 2.3a). Equally important, they displayed increased specific elastic modulus (Figure 2.3b), in comparison with single fiber polymer blends. Moreover, these parameters can be tuned by adjusting the concentration and relative ratio of each component in a multi-modal nanofabric. Because 4-6 wt/v% solutions yielded nanoscale fibers for both polymers, these concentrations were used to assess the influence of polymer ratio on network mechanical properties. Using various combinations of 4 wt/v% and 6 wt/v% nylon and PU solutions, the nylon:PU ratio in multi-material samples was varied from 1:1 to 3:2 and 2:3. Due to the higher toughness and lower elastic modulus of PU relative to nylon, we predicted that higher concentrations of the elastomer would increase the toughness and decrease the tensile modulus of the overall composite. As expected, multi-material fabrics with a lower nylon:PU ratio and larger PU nanofibers exhibited higher toughness and lower specific elastic moduli than those with higher ratios or thinner elastomer fibers (Figure 2.3c-d). The difference in mechanical properties between single fiber blends and multi-material composite samples may be influenced by whether nylon and PU are both localized in each fiber (blend) or in separate fibers (multi-material). To further explore the dispersion pattern of both polymers in a nanofiber sheet, we used FTIR to generate 2D contour maps. Two characteristic vibrational modes for nylon and for PU were selected, and the intensity of these peaks was recorded to map the location of each polymer across 75 regions of interest on a 10 mm2 nanofiber sheet (Figure 2.4a). The normalized intensity of each polymer at a given location was illustrated using a color gradient from red to blue, with red indicating higher polymer concentrations and blue denoting lower

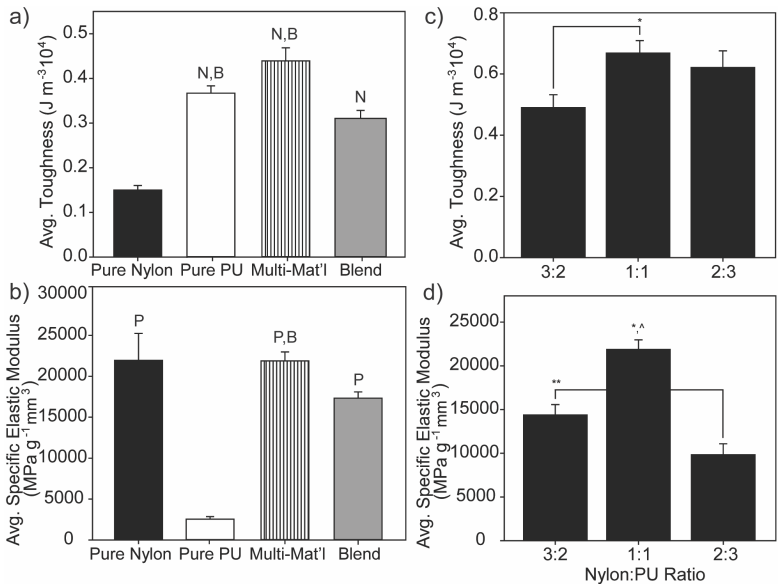


Figure 2.3: Comparative a) toughness and b) specific elastic modulus of pure Nylon and PU, single fiber Nylon/PU blend, and multi-material Nylon/PU nanofabrics. Varying Nylon/PU ratio and concentration enables us to tune the c) toughness and d) specific elastic modulus of a multi-material nanofabric. *,**, N, B, and P indicate p <0.05. N, B, and P denote significant difference from Pure Nylon, Pure PU, and Blend, respectively. For all conditions, n = 3 production runs and 3 samples per run.

local concentrations. In our analysis, 2D FTIR contour maps indicate that nylon and PU nanofibers are well-integrated in the multi-material sheet (Figure 2.4b), and suggest that their dispersion is more heterogeneous on the network level than in the blend sheet (Figure 2.4c). This stratification may account for the higher toughness of the multi-material nanofabric by facilitating load transfer from stiffer nylon fibers to more elastic PU fibers.

2.5 Manufacturing Composite Nanofabrics using Orthogonal Solvents

Finally, we asked whether the DCR could be used to fabricate multi-material nanotextiles using orthogonal solvents. To explore this question, we chose the piezoelectric co-polymer PVDF-TrFE as a proof of concept. Unlike nylon and polyurethane, PVDF-TrFE has limited solubility in most of the organic solvents used for RJS. Moreover, although the co-polymer is less brittle than more com-

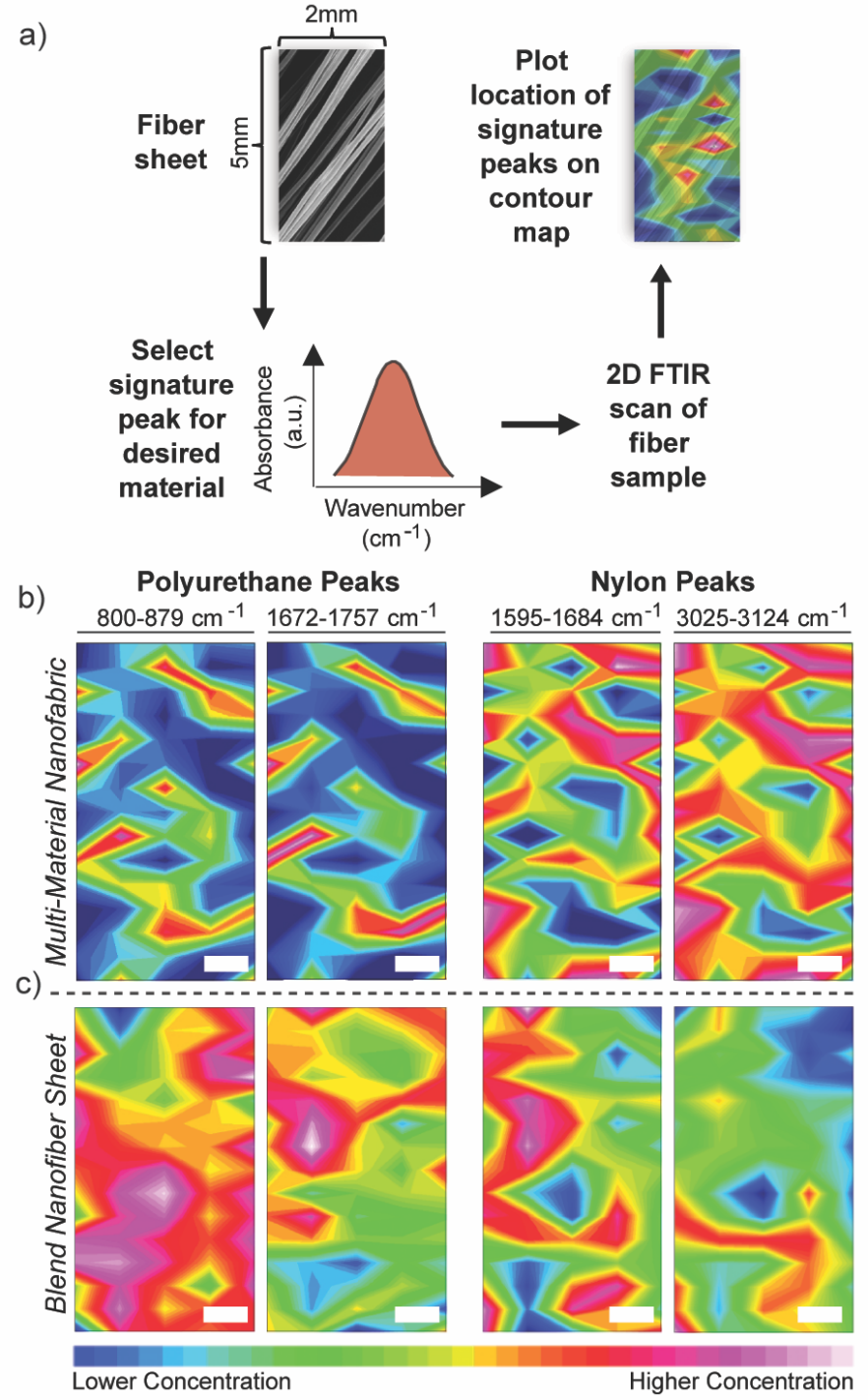


Figure 2.4: a) Schematic of experimental setup used to analyze dispersion of polymer components in nanofabrics. 2D FTIR contour maps of Nylon and PU dispersion in b) multi-material nanofabrics and c) blend nanofibers. The normalized intensity is indicated using a color gradient. Red regions signify higher polymer concentrations, while blue indicates lower concentrations. For each condition, n = 3 production runs, with n = 3 samples and 75 FOVs per sample. Representative contour maps are shown. Scale bars: 0.5 mm.

monly used inorganic piezoelectric ceramics (e.g. lead zirconate titanate), many PVDF-TrFE-based sensors rely on sandwiching nanofiber mats between elastic sheets to increase flexibility[144]. Thus, by producing a composite nanofabric using PVDF-TrFE and PU, this method has the potential to preserve the piezoelectricity of the co-polymer while incorporating an elastomer on the nanoscale as a mechanical support.

Precursor solutions of 6 wt/v% PU in HFIP and 15 wt/v% PVDF-TrFE in DMF:acetone (1:1) were infused into the inner and outer DCR chambers, respectively. Relevant vibrational modes of PVDF-TrFE (crystalline β phase, 840 cm^{-1}) and PU (C-O-C stretch, 1162 cm^{-1}) were examined using FTIR. Composite nanofabric spectra were compared to those of pure PU nanofibers and of PVDF-TrFE cast films (Figure 2.5). Both characteristic peaks are present in the multi-material PU/PVDF-TrFE nanofabrics, indicating the presence of both types of polymer nanofibers. This data suggests the ability of this technique to fabricate composite nanofabrics using two materials with orthogonal solvents. Future research may investigate the mechanical and electrical properties of PU/PVDF-TrFE composites and explore the impact of component ratio on bulk piezoelectricity.

2.6 Summary

In this chapter, we demonstrated a novel technique to manufacture multi-material polymer nanofabrics using rotary jet spinning. Taken collectively, our data suggest that adding a dual chamber reservoir to the RJS system provides three key advantages for fiber fabrication: (1) mechanical properties can be controlled by tuning the ratio and concentration of each component, (2) both fiber types are well dispersed throughout the nanofabric, and (3) multiple polymers can be spun into the same nanofabric regardless of solvent compatibility (e.g. orthogonal solvents can be used for each individual material). This method simplifies the process of generating multi-phase nanofabrics using two polymers and/or immiscible solvents. In the next chapter, we will utilize the toughness and flexibil-

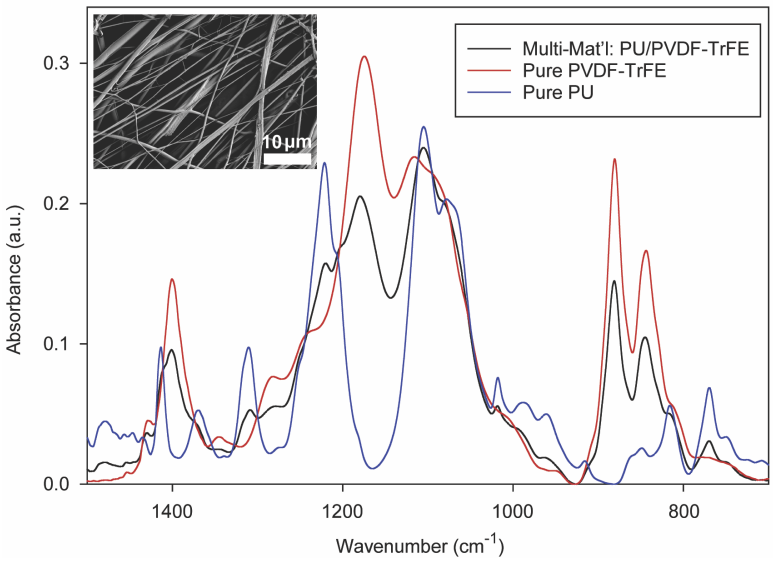


Figure 2.5: FTIR spectra of pure PVDF-TrFE, pure PU, and multi-material PVDF-TrFE/PU nanofabrics. Data are averaged for n = 3 samples, with 16 FOVs per sample. *Inset*: Scanning electron micrograph of multi-material PVDF-TrFE/PU nanofabric.

ity of rotary jet spun nanofabrics to reinforce soft robotic actuators.

3

Nanofiber-Reinforced Soft Fluidic Micro-Actuators

3.1 Introduction

In the previous two chapters, we have discussed methods for manufacturing and characterizing polymer nanofibers. In this chapter, we will examine their utility as strain-limiting materials and demon-

strate the integration of nonwoven nanofiber sheets into composite micro-actuators.

Micro-scale soft actuators may be classified according to their expansion method, namely: membrane deflection (Figure 3.1a), bellows expansion (Figure 3.1b), balloon inflation (Figure 3.1c), or contraction-based artificial muscles (Figure 3.1d)[39]. Currently, state-of-the-art soft micro-actuators are fabricated using processes such as soft lithography, dip-coating, casting, and additive manufacturing[52,50,62,145]. The bending modes of balloon-type micro-scale actuators manufactured through these methods are controlled by varying the air channel angle[146,58], thickness or elastic modulus of layers surrounding the channel[44,57,147,148], and device geometry[51,52]. However, the curvature and full actuation pressure of elastomer-based micro-actuators are limited by the thickness of the strain limiting layer[62]. Reinforcing soft actuators with a strain limiting fiber has successfully bridged this capability gap for larger, centimeter-scale pneumatic actuators[59,149,26,150]. Fibers are an effective reinforcement layer for fluidic actuators because: 1) their inherent anisotropy facilitates directional control of actuator bending and mechanical properties, and 2) their flexibility and porosity are compatible with existing soft lithography techniques. However, yarn and woven fiber-based reinforcements used in macro-scale devices are too large to act as a strain limiting layer for micro-scale actuators. A lightweight, yet tough fibrous material is needed to regulate micro-scale bending without significantly increasing the actuator size, reducing compliance, or impairing its interaction with delicate objects.

Nanofibers are a promising reinforcement material for soft micro-actuators due to their flexibility, high specific strength, customizable size and mechanical properties, and ease of processing[151,64]. Nonwoven nanofabrics have previously been established as a basis for a wide range of applications, including: tissue engineering scaffolds[152,86], artificial muscles and bio-actuators[153,154], filtration membranes[155,156], flexible sensors[157,158], and textiles[112]. Using fabrication processes such as rotary jet spinning and electrospinning, it is possible to regulate the mechanical and material properties of nanofabrics and to manufacture uniform fiber sheets with customizable fiber diameter and orien-

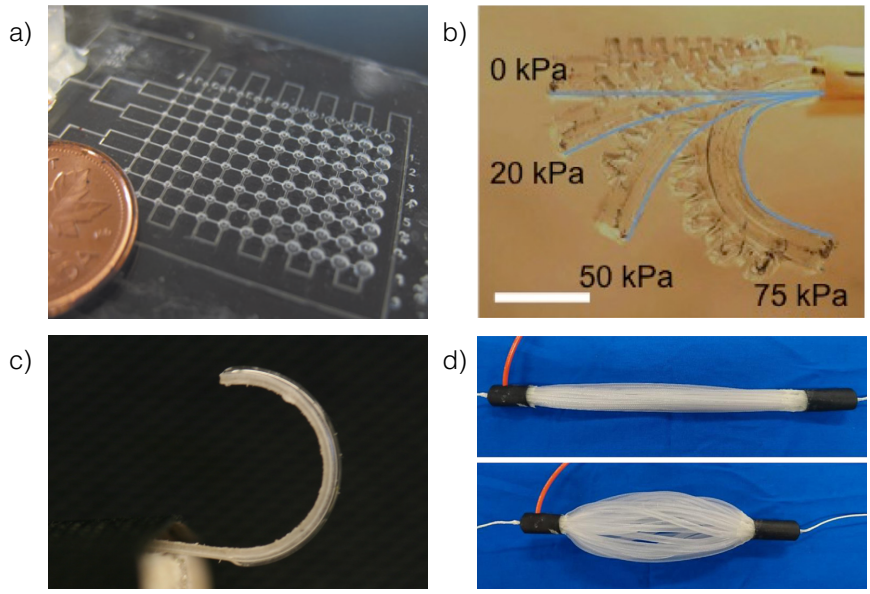


Figure 3.1: Classification of soft actuators. a) Membrane deflection. Reproduced with permission from [159] with permission from the Royal Society of Chemistry. b) Bellows expansion. Reproduced with permission from [50]. c) Balloon inflation. d) Contraction-based artificial muscles. Reproduced with permission from [150].

tation [99,102,125,104]. Despite their compliance, robustness, and controllable morphology, nanofibers have not yet been integrated into soft robotic devices.

To overcome the limitations of existing elastomer-based micro-actuators, we present a novel fabrication process for nanofiber-reinforced pneumatic actuators. In this chapter, we demonstrate manufacturing of composite PDMS-nanofiber actuators using a combination of rotary jet spinning and soft lithography. Furthermore, we examine the influence of layer design and nanofiber orientation on actuator curvature, bulk mechanical properties, and actuation pressure. Finally, we highlight the ability of this method to replicate two benchmark bending modes of macro-scale fiber reinforced actuators: bending and bending-twisting. Our data reveal that composite micro-scale actuators are tougher and stronger than pure elastomer devices, while displaying comparable elongation.

3.2 Experimental Methods

3.2.1 Nanofiber fabrication using rotary jet spinning

Nonwoven nanofiber sheets were manufactured using rotary jet spinning, following a previously reported protocol[99,86]. A solution of 3 wt./v% nylon-6 (Nylon 6, Sigma-Aldrich, St. Louis, MO) / 3 wt./v% polyurethane (McMaster Carr, Princeton, NJ) was prepared in 1,1,1,3,3,3-hexafluoro-2-propanol (HFIP, Sigma-Aldrich, St. Louis, MO), and infused into the reservoir for one minute at a rate of 5 mL min^{-1} (Figure 3.2a). The resulting nanofiber sheets were collected using a rotating cylindrical mandrel attached to a linear motor. Following fiber fabrication, samples were compressed to remove creases and to improve uniformity during the subsequent soft lithography process. Each sheet was pressed for 10 min at 3000lbs (applied over an area of 132 cm^2) and 50°C using a laboratory hydraulic molding press (Carver Laboratory Press, Wabash, IN).

3.2.2 Actuator design and fabrication

Composite nanofiber micro-actuators were fabricated using a four step process. First, PDMS was formulated by combining Sylgard 184 (Dow Corning, MI, USA) elastomer base and curing agent in a 10:1 ratio. The mixture was spin coated onto an embossed silicon wafer at 300 rpm, de-gassed in an vacuum chamber for 10 min, thermally cured for two hours at 65 °C, and then removed from the wafer (Figure 3.3a). Next, a PDMS layer was spin coated at 100 rpm onto an unpatterned silicon wafer, de-gassed, and partially crosslinked for ten minutes at 75°C. Using a film applicator, a nanofiber sheet was coated with 20 μm uncured PDMS. The fiber sheet was placed on the semi-cured PDMS wafer, spin coated at 200 rpm, thermally cured for 30 minutes, and removed from the wafer (Figure 3.3b). At this stage, the soft lithography-based work flow can be easily adapted to construct other laminate configurations. In addition to the three-layer (air channel, passive PDMS layer,

nanofiber layer) actuator, we fabricated a four-layer composite (air channel, passive PDMS layer, nanofiber layer, passive PDMS layer) to test the effect of the nanofiber layer position with respect to the neutral axis on actuator curvature. The four-layer laminate was fabricated by spin coating an additional layer of PDMS onto the nanofiber sheet before the 30min cure stage. The fabrication process for three- and four-layer actuators was identical following this step: the patterned and unpatterned layers were irreversibly bonded together using an oxygen plasma treatment (65 W for 30 s). The resulting composite actuators were machined in the desired geometry using a custom DPSS laser, then removed from the bulk sheet (Figure 3.3c). Lastly, catheter tubing (MicroRenathane Catheter Tubing, Braintree Scientific, Inc., MA, USA) was inserted and sealed (Scotch-Weld 1838 B/A, 3M) into the channel of each micro-actuator.

3.2.3 Modeling bending of composite soft actuators

An analytical 2D model was derived to better understand the effect of layer design and composition on bending behavior of multi-layer composite micro-actuators. Our model includes the following assumptions: 1) perfect bonding and no slippage between layers, 2) each layer is homogeneous, with known properties, 3) the PDMS matrix and membrane are incompressible, 4) the bending moment of a pressurized actuator is constant along the actuator length, 5) the Young's moduli of PDMS and polymer nanofibers remain constant during pressurization, 6) the strain limiting layer is inextensible, and 7) gravity is neglected during actuator bending.

Here, a pressurized micro-actuator was considered to be a clamped-free cantilever beam (Figure 3.4a), and modeled as an incompressible Neo-Hookean material. The assumption of incompressibility yields the following invariant relationship between the three principal stretch ratios (λ_1, λ_2, λ_3):

$$\lambda_1\lambda_2\lambda_3 = 1 \tag{3.1}$$

The longitudinal stretch was represented by $\lambda_1 = \frac{dl}{dL}$, in which L indicates the initial length of the actuator and l is the length in the deformed state. Here, we set $\lambda_1 = 1$ under the assumption that longitudinal deformation is negligible compared to axial and circumferential expansion. Thus, the circumferential (λ_2) and axial (λ_3) stretches can be related as $\lambda_3 = \lambda_2^{-1}$. Further, circumferential stretch was defined as $\lambda_2 = \frac{s}{2a}$, where s denotes the arc length of the inflating air channel and $2a$ indicates the width of the inflated channel. Using geometry,

$$\lambda_2 = \frac{s}{2a} \tag{3.2}$$

$$= \frac{r\vartheta}{2a} \tag{3.3}$$

$$= \frac{r}{a}\arcsin\frac{a}{r} \tag{3.4}$$

Here, r represents the radius of curvature of the circular sector. Next, the axial stretch was defined as $\lambda_3 = \frac{t}{T}$, in which T represents the thickness of the upper channel membrane prior to inflation (measured using scanning electron microscopy as 0.103 mm), and t is the thickness of the inflated air channel membrane. Using the incompressibility condition, we can express both λ_3 and t in terms of λ_2:

$$\lambda_3 = \frac{t}{T} = \frac{1}{\lambda_2} \tag{3.5}$$

$$t = \lambda_3 T \tag{3.6}$$

$$= \frac{aT}{r \arcsin \frac{a}{r}} \tag{3.7}$$

Therefore, only one independent stretch is present for this geometry. As the actuator inflates, the relationship between radius of curvature of the air channel membrane and input pressure (P) was calculated by equating the hoop stress of a thin-walled cylindrical pressure vessel in terms of the applied pressure ($\sigma_2 = \frac{Pr}{t}$) and the principal stretch ratios ($\sigma_2 = \mu(\lambda_2^2 - \lambda_3^2)$):

$$P = \frac{\mu}{r} \frac{T}{\frac{r}{a} \arcsin \frac{a}{r}} \left((\frac{r}{a} \arcsin \frac{a}{r})^2 - (\frac{1}{\frac{r}{a} \arcsin \frac{a}{r}})^2 \right) \tag{3.8}$$

In this expression, μ represents the shear modulus of the PDMS membrane. For the purposes of this analysis, we assume $E_m = 3\mu$ (where E_m is the membrane Young's modulus) to be constant throughout pressurization; however, future studies will reflect the instantaneous elastic modulus as the elastomeric membrane strains and stiffens. Although the inflating membrane is monolithic, the stiffness of PDMS samples undergoes a shift from bulk behavior to dimension dependence below a thickness of 200 μm. Below this inflection point, the Young's modulus of PDMS samples is greater than 1.2 MPa[160]. As the thickness of the inflating membrane is within this range, we assume $E_m =$ 1.2 MPa for Equation (3.8). However, the bulk elastic modulus (recorded as 0.6 MPa,) was used for calculations involving the thicker, passive PDMS layers in the actuator.

As per Euler-Bernoulli beam theory, the curvature (ϱ^{-1}) of a composite beam is given by:

$$\frac{1}{\rho} = \frac{\mathcal{M}}{EI_i + E_m I_m} \tag{3.9}$$

where E is the effective Young's modulus of the composite beam, I_i is the total area moment of inertia for the passive PDMS and fiber lamina, E_m is the Young's modulus of the inflating PDMS membrane, I_m is the area moment of inertia of the membrane, and $\mathcal{M}$ is the bending torque of the actuator due to air pressure on the distal cap. The Young's modulus of 3 wt./v% nylon / 3 wt./v% polyurethane nanofiber sheets embedded longitudinally and transversely in 20 μm PDMS layers were measured to be 1.5 MPa and 0.741 MPa, respectively (Figure A.7a).

The area moment of inertia for the composite laminate structures can be calculated using a parallel axis theorem:

$$I = \sum_{i=1}^{l} (I_i + \mathcal{A}_i d_i^2) \tag{3.10}$$

In this expression, I_i is the moment of inertia for an individual layer, $\mathcal{A}_i$ is the layer's cross-sectional area, and d_i is the distance from the layer's centroid to the actuator centroid. The summation index i represents each layer in the composite structure, and l is the total number of layers in a given actuator. The moment of inertia for rectangular layers of PDMS and nanofibers was calculated using the following equation:

$$I_i = \frac{b_i h_i^3}{12} + b_i h_i d_i^2 \tag{3.11}$$

in which b_i and h_i represent the width and height, respectively, of a given layer in a laminate. For composite laminates with disparate elastic moduli, the width of the stiffer layer is typically scaled

using an expansion factor, $n = \frac{E_1}{E_2}$, in which $E_2 < E_1$. Thus, the width of the nanofiber layer was determined by multiplying the expansion factor $n = \frac{E_{\text{fiber}}}{E_{\text{PDMS}}}$ by the measured width of the fiber lamina. The inflated air channel was considered to be a hollow circular sector, and its area moment of inertia was calculated as follows:

$$I_i = \frac{\alpha}{4}(R^4 - r^4)(1 - \frac{\sin\alpha\cos\alpha}{\alpha}) \tag{3.12}$$

In this equation, α is one half the circular sector angle, and R and r denote the outer and inner radii of curvature of the inflated channel, respectively (Figure 3.4a)[161]. Thus, I_m were calculated using Equations (3.10) and (3.12). Using Equations (3.9)-(3.12), the moments of inertia of each layer were summed to determine the total moment of inertia for the composite actuator.

Finally, the bending torque of internal air pressure ($\mathcal{M}$) was calculated. Based on Assumption (4), the bending moment is constant along the longitudinal axis of the actuator. In this analysis, $\mathcal{M}$ was derived with respect to the cap (Figure 3.4a) with which the air channel terminates at the distal end of the actuator. The bending torque of internal air pressure on the distal cap was determined by multiplying the applied air pressure (P), the summed cross-sectional areas of the inflated channel and the original area of the air channel ($\mathcal{A}_{\text{in}}$), and the lever arm of the inflated area with respect to the total actuator centroid (d_{in}):

$$\mathcal{M} = P\mathcal{A}_{\text{in}}d_{\text{in}} \tag{3.13}$$

We assume that the cross-sectional area of the inflated section is constant along the length of the actuator, and that the distance between the distal cap and the end of the actuator is negligibly small

with respect to the total device length. Using this analytical framework, the actuator curvature was calculated as a function of pressure and compared with empirical results.

3.2.4 Nanofiber image analysis

Nanofiber samples were affixed to carbon-taped scanning electron microscopy stubs, and subsequently sputter coated using a Pt/Pd target (Denton Vacuum, Moorestown, NJ). Coated stubs were imaged using a field emission scanning electron microscope (Carl Zeiss, Dresden, Germany). Image analysis was performed using Fiji (http:// ji.sc/Fiji, Ashburn, VA). For each case, 135 fibers were analyzed using three random fields of view per sample and three samples per condition.

3.2.5 Mechanical characterization of composite actuators

Rectangular samples of PDMS (length = 20 mm, width = 10 mm), monolithic nanofabrics coated in 20 μm PDMS (length = 20 mm, width = 10 mm), and composite PDMS-nanofiber laminates (length = 20 mm, width = 0.78 mm) were laser cut from bulk samples. For fibrous materials, 2 mm on either side of each sheet was sealed using epoxy and tape to prevent slippage of fibers in the Instron clamps. Using a uniaxial tensile test (Instron 5544A, Norwood, MA), specimens were extended in air at a rate of 8 mm/min until failure. Before each run, the gauge length, width, and thickness of each sample were recorded using a micrometer. Following the measurement, materials were weighed; uniform density was assumed for each sample.

3.2.6 Actuator bending characterization

The curvature of composite micro-actuators was recorded in air. First, each actuator was fixed at a distance of 12 cm from a Canon Eos Rebel Ti. Next, the actuators were pressurized using a syringe pump at a rate of 1 mL/min until failure. Actuators were photographed every 0.1 bar; the resulting

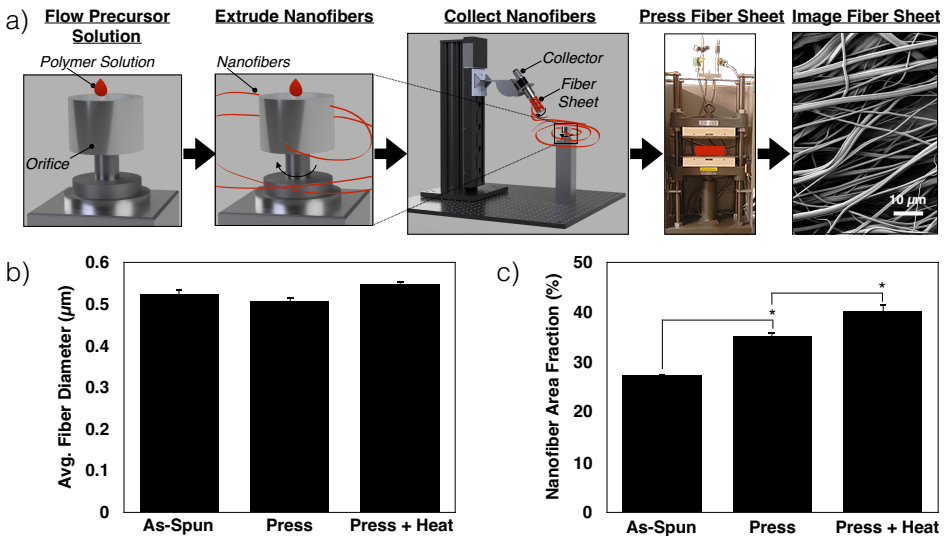


Figure 3.2: a) Schematic of the fiber fabrication process using the rotary jet spinning system, post-processing using a hydraulic press[162], and a scanning electron micrograph of 6 wt./v% Nylon/Polyurethane (1:1) nanofibers, b) Average diameter and c) porosity of as-spun, pressed, and pressed/heated nanofiber sheets. n = 3 production runs per condition, one sample/run, three random fields of view/sample. Error is reported as SEM. * indicates p <0.05.

images were analyzed using Fiji.

3.3 Nanofiber Morphology is Independent of Post-Processing

Prior to assembling the composite micro-actuators, we examined whether fiber post-processing steps (e.g. compression molding and heating) alter the fiber diameter or porosity of nanofiber networks. First, nanofiber sheets were manufactured via rotary jet spinning (Figure 3.2a), as described in Section 3.2.1. Average fiber diameter (Figure 3.2b) and fabric porosity (reported in Figure 3.2c as the fiber area fraction) were measured for as-spun nanofiber sheets, and compared to those of samples that had been pressed, and both pressed and heated. Samples were heated for 30 min at 75°, to simulate the conditions under which PDMS is cured. While neither post-processing step significantly impacted the average fiber diameter, the area fraction of fibers increased after both pressing and heating. This result is logical, as the compression process reduces the area between adjacent

nanofiber layers. The lack of damage to fiber sheets during post-processing confirms our capability to regulate fiber morphology during the nanofiber manufacturing processes, and the ability of nanofibers to withstand post-processing steps for soft lithography.

3.4 Effect of Nanofiber Orientation and Actuator Design on Bending

Having established a consistent method to control nanofabric morphology, we then investigated whether the position of the nanofiber layer relative to the neutral axis impacts actuator radius of curvature and pressurization range. Composite actuators were fabricated using a four step method, detailed in Section 3.2.2 and illustrated in Figure 3.3. This process was used to assemble three- and four-layer devices, varying the location of the nanofiber sheet. As a control, two-layer actuators were fabricated using only PDMS (Figure 3.4b). Three-layer actuators featured the fiber sheet as the outer layer of the device (Figure 3.4c), while four-layer actuators incorporated an additional PDMS layer around the nanotextiles (Figure 3.4d). To understand the impact of fiber orientation on actuator bending, nanofiber sheets were positioned at either 0° or 90° relative to the longitudinal axis of the actuator.

Using the analytical framework discussed in section 3.2.3, actuator curvature was modeled as a function of pressure and compared to empirical data. All actuators were pressurized from rest (0 bar) to failure. To ensure consistent statistical analysis among each sample set, averaged experimental values are shown for the range between the onset of inflation (constant within each device layout) and the earliest failure point within that category; analytical values are displayed within the same range for each actuator design (Figure 3.5). Figure 3.5a displays theoretical and empirical results for the control two- layer actuators, composed only of PDMS. Nonlinearity in the relation between pressure and curvature is due to that of the pressure-stretch and pressure-area relations (Figure A.8), as well as the balance between membrane thinning and material stiffening during inflation[163,164]. As

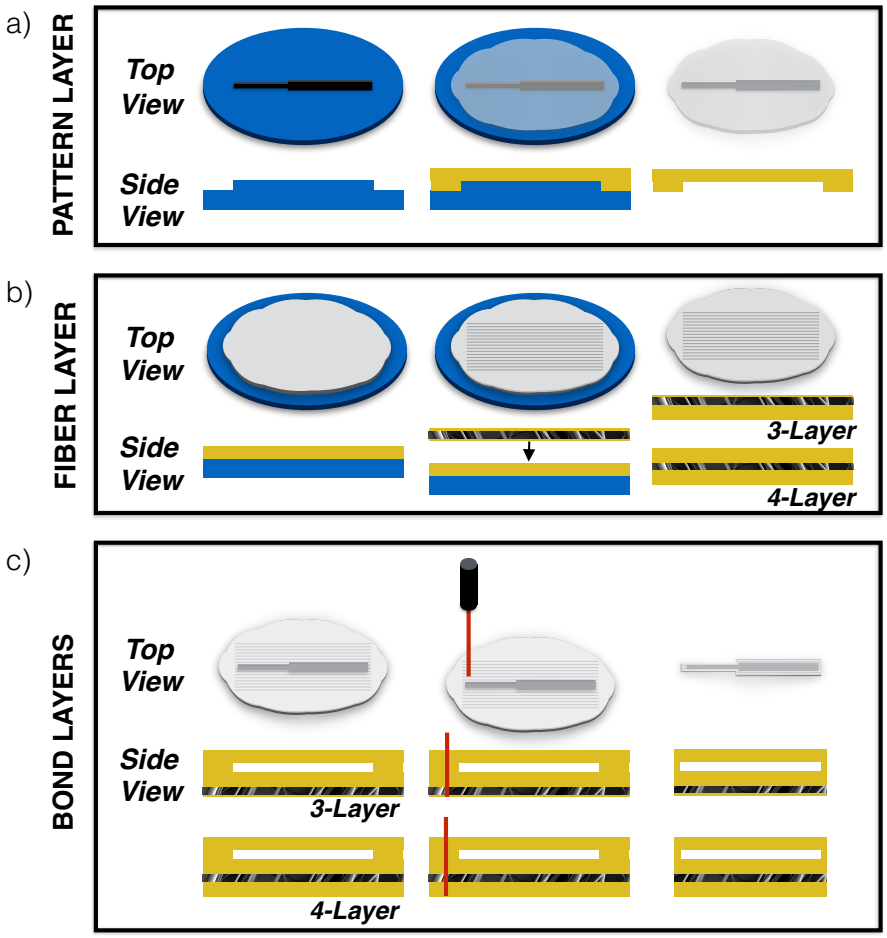


Figure 3.3: Fabricating composite soft actuators. a) PDMS (yellow) is coated, cured, and peeled from a patterned wafer (blue). b) PDMS and fiber (striped) layers are coated, cured, and removed from a blank wafer. c) Sub-laminates are plasma bonded and the actuator is laser-cut.

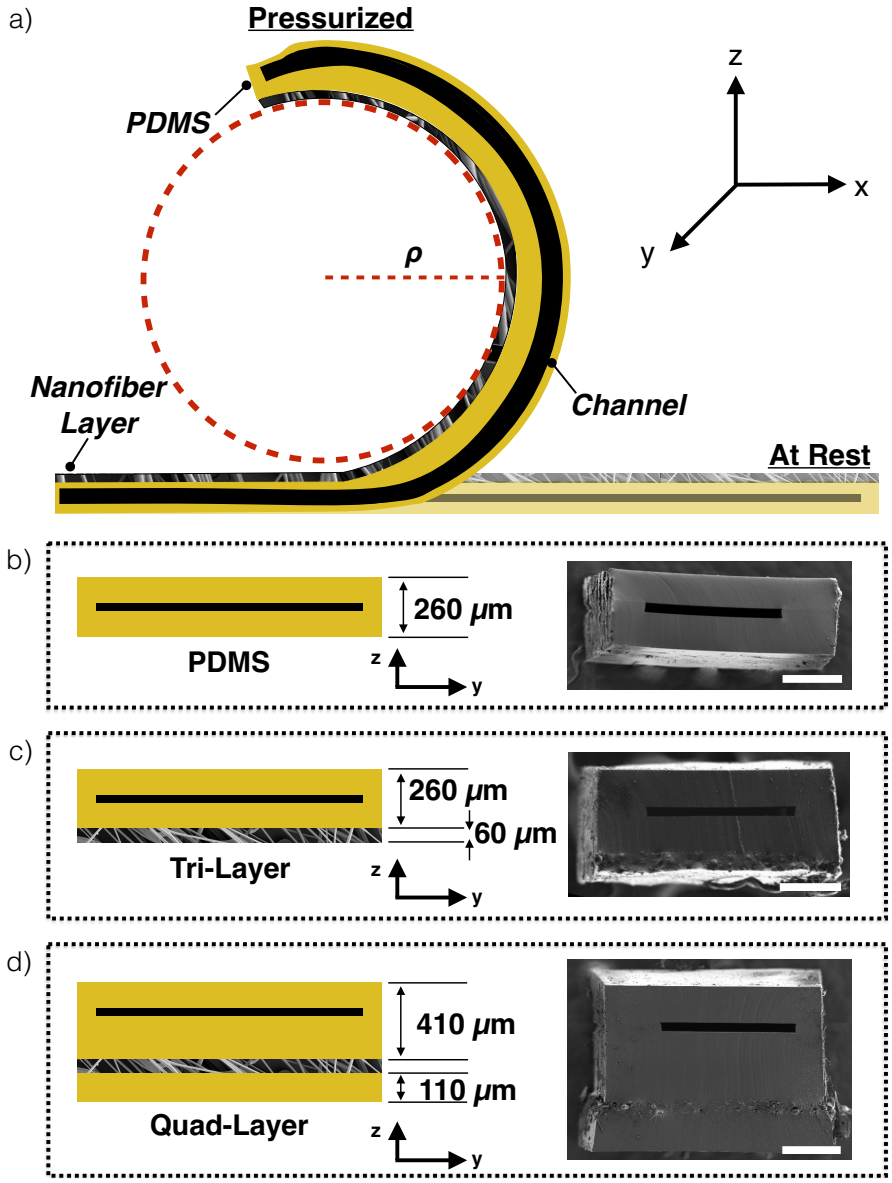


Figure 3.4: a) Illustration of at-rest and inflated three-layer actuator. The left end of the actuator is fixed, while the distal end moves freely. Isotropic view and cross-sectional schematic of the distal tip of an inflated 3-layer composite actuator. Cross-sectional diagrams and scanning electron micrographs of b) PDMS, c) Three- and d) four-layer laminates. Scale: 200 μm

the air channel is pressurized, curvature will first increase rapidly as the elastomeric membrane inflates and its thickness decreases; thinning of the inextensible membrane can be assumed according to assumption (3). At higher pressures, membrane thinning will outweigh the impact of the material stiffening, and the rate of change of the curvature will decrease before the membrane ruptures. Similar trends are evident for three-layer composite actuators with nanofibers oriented parallel (Figure 3.5b)) and perpendicular (Figure 3.5c) to the longitudinal axis, and four-layer actuators with parallel fibers (Figure 3.5d). The analytical model addresses this nonlinearity by assuming the reference state of the actuator air channel to be inflated, and considering small perturbations from this deformed geometry. Generally, the model predicts the experimental trends well, though we expect that future analyses will increase the accuracy of analytical predictions by accounting for membrane stiffening during inflation (i.e. determining the instantaneous Young's modulus rather than assuming $E_m = 3\mu$, where μ is the shear modulus).

Figure 3.6a compares the pressure-curvature relationship for PDMS-only and three-layer fiber-reinforced micro-actuators. Curvature is inversely proportional to actuator stiffness; thus, the fully elastomeric actuators are more sensitive than fibrous devices to pneumatic pressure and display greater curvature for a given pressure. However, this correlation does not apply between composite actuators with parallel (Young's modulus: 1.5MPa) and perpendicularly (Young's modulus: 0.741MPa) oriented nanofibers. For both parallel and perpendicularly oriented nanofibers, the rate of change for actuator radius of curvature is inversely proportional to applied pressure (Figure 3.6b). Experimentally, actuators with fibers oriented at 90° (labeled perpendicular) begin inflating at a slightly higher pressure, as compared to those with fibers placed at 0° (labeled parallel). Although the perpendicular nanofibers have a lower Young's modulus when encased in PDMS, it appears that the stiffer parallel fibers are more sensitive to applied pressure and experience more deflection for a given pressure. Decreasing stiffness of the strain limiting layer in the bend direction shifts the laminate's centroid upwards toward the inflating membrane, thus inhibiting bending at low pressures.

Moreover, the orientation of nanofibers orthogonal to the air channel potentially stiffens the inflation chamber, limiting its ability to expand. While the analytical model presented here predicts this behavior, the deformation of the inflated channel due to directional stiffening may be explored in future studies using finite-element method modeling.

Empirical data for three- and four-layer actuators reinforced by parallel fibers is shown in Figure 3.6c. While both devices initiate bending at a similar pressure, three-layer devices display slightly higher curvature under moderate pressure, and four-layer actuators sustain significantly higher pressurization before failure. This result indicates that while movement of the neutral axis toward the air channel inhibits bending, positioning the fibrous layer within the actuator increases robustness of the device. Finally, Figure 3.6d displays the pressure-curvature relations for all four actuator varieties.

Overall, all composite actuator designs displayed a significantly larger curvature compared to pure PDMS actuators. Moreover, composite designs were able to withstand up to 30% higher pressure before failure (rupture at the side of the channel). The average maximum pressurization of fiber-reinforced actuators was between 2.5–3.25 bar, on par with that of existing elastomer-based micro-[62,148] and centimeter-scale pneumatic actuators[56]. This range of maximum pressure is approximately 3–12 times higher than recently proposed PDMS actuators fabricated using 3D printing (0.95 bar)[50], soft lithography (0.25 bar)[31], spin coating (1 bar)[58], and inverse-flow injection (1 bar)[165]. Collectively, these results indicate that by modulating the position and orientation of nanofiber sheets, we can both conserve and modulate the curvature of elastomeric micro-actuators while extending the pressurization range.

3.5 Composite structure influences bulk mechanical properties

On the macro- and mesoscale, it is well known that incorporating comparatively stiffer reinforcement fibers in a compliant matrix increases bulk strength and toughness by transferring tensile load

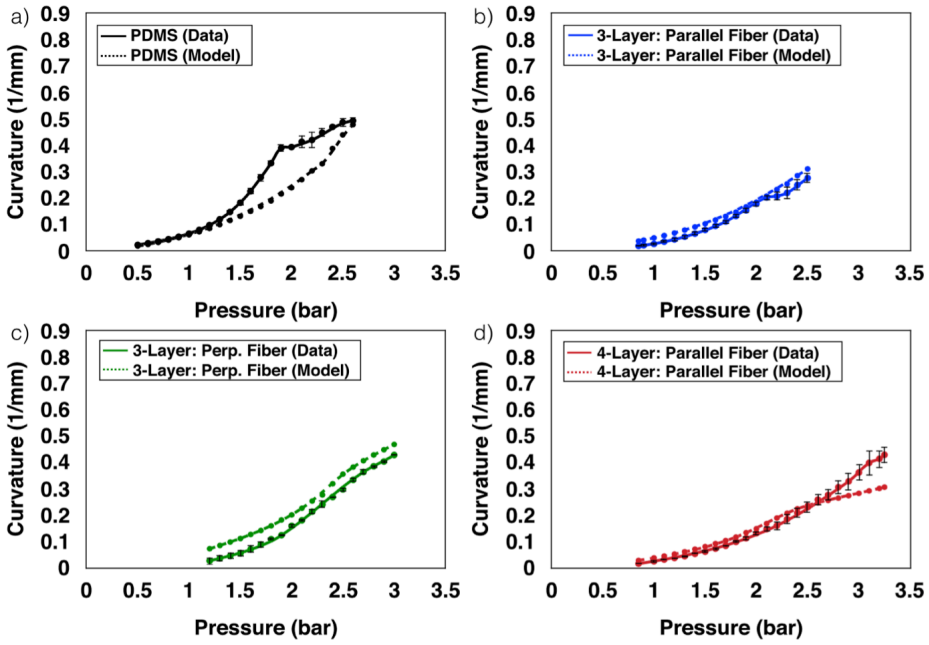


Figure 3.5: Analytical and experimental results for the curvature of a) tri-layer, b) quad-layer, and c) pure PDMS micro-actuators. d) Comparison of empirical data for three-layer composite and PDMS actuators. n = 2-3 actuators per condition. All error is reported as SEM.

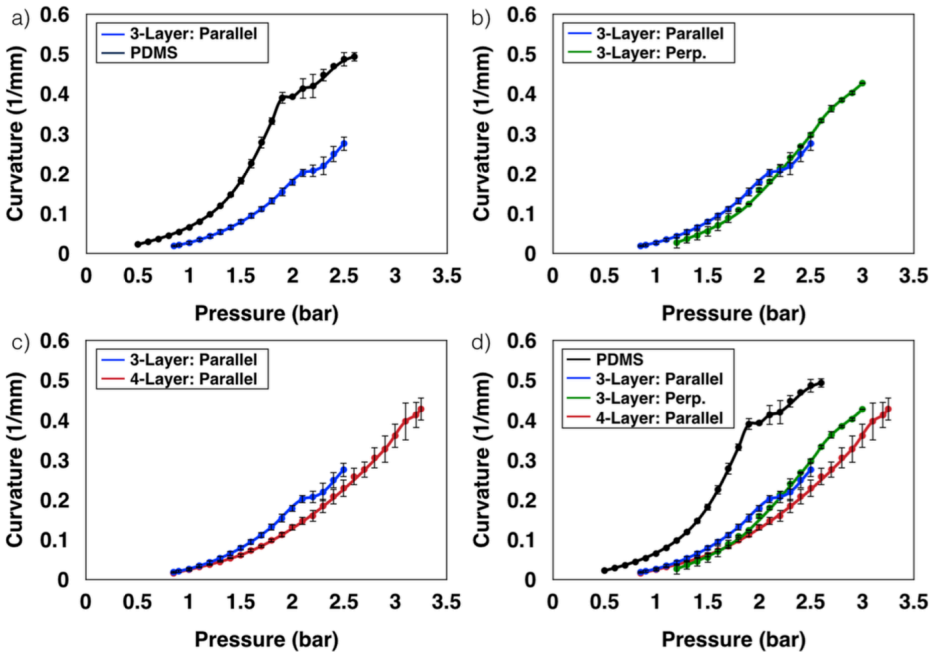


Figure 3.6: Curvature of (a) pure PDMS and three-Layer composite device with nanofibers parallel to actuator, (b) Three-Layer composite actuators with parallel and perpendicular fibers, (c) Three- and four-Layer PDMS-nanofiber actuators with fibers oriented parallel to device, and (d) Comparison of curvature for three- and four-layer composite and PDMS-only actuators. n = 2–3 actuators per condition. All error is reported as SEM.

from the matrix to the reinforcement material[26,166,167,168]. We expected to observe a similar trend by reinforcing micro-scale PDMS actuators with nanofiber sheets. To understand the effect of laminate design and fiber orientation on device mechanics, tensile properties of composite and PDMS-only actuators were quantified using Instron uniaxial testing (Figure A.7b).

Both three- and four-layer actuators reinforced by parallel nanofibers displayed higher toughness (Figure 3.7a), specific ultimate tensile strength (Figure 3.7b), and specific elastic modulus (Figure 3.7c) than pure PDMS. This increased stiffness explains, in part, the lesser curvature of composite actuators relative to PDMS-only devices. However, three- layer actuators were significantly tougher and stronger than four-layer actuators with fibers in the same respective configurations. Furthermore, unlike four-layer constructs, three-layer laminate devices maintained the elongation of pure

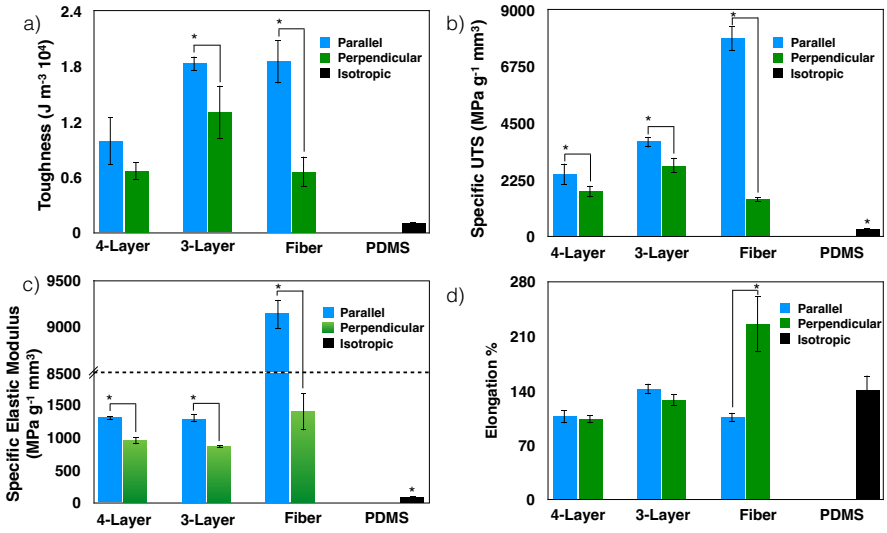


Figure 3.7: Mechanical properties of composite and elastomer actuators. a) Toughness, b) Specific ultimate tensile strength (UTS), c) Specific Elastic Modulus, and d) Elongation of three- and four-layer composite actuators, nanofiber sheets embedded in a 20μm PDMS layer, and pure PDMS actuators. n = 3 samples per condition. All error reported as SEM. * indicates p <0.05.

PDMS (Figure 3.7d). Lastly, a three-layer design with 0° nanofibers displayed a similar toughness to that of a pure nanofiber sheet of the same orientation; this value was 2.3 times greater than the toughness of PDMS alone. Taken as a whole, this data indicates that a three-layer actuator design increases toughness while preserving desired extensibility of elastomer actuators. Based on these results, the three-layer composite design was selected for use in future devices. Examination of samples under a scanning electron microscope revealed no deformation between the nanofiber sheet and PDMS matrix (Figure A.7c-d). As the composite sheet was extended to failure, cracks formed normal to the tensile stress plane and fracture occurred in the plane of fiber fracture. This failure mode is consistent with a reinforcing material that is stronger and more brittle than the matrix material, and with the lack of fiber de-bonding from the surrounding PDMS[169]. It is also possible that the high surface area of nanofibers resists de-bonding of the fiber layer from the surrounding matrix.

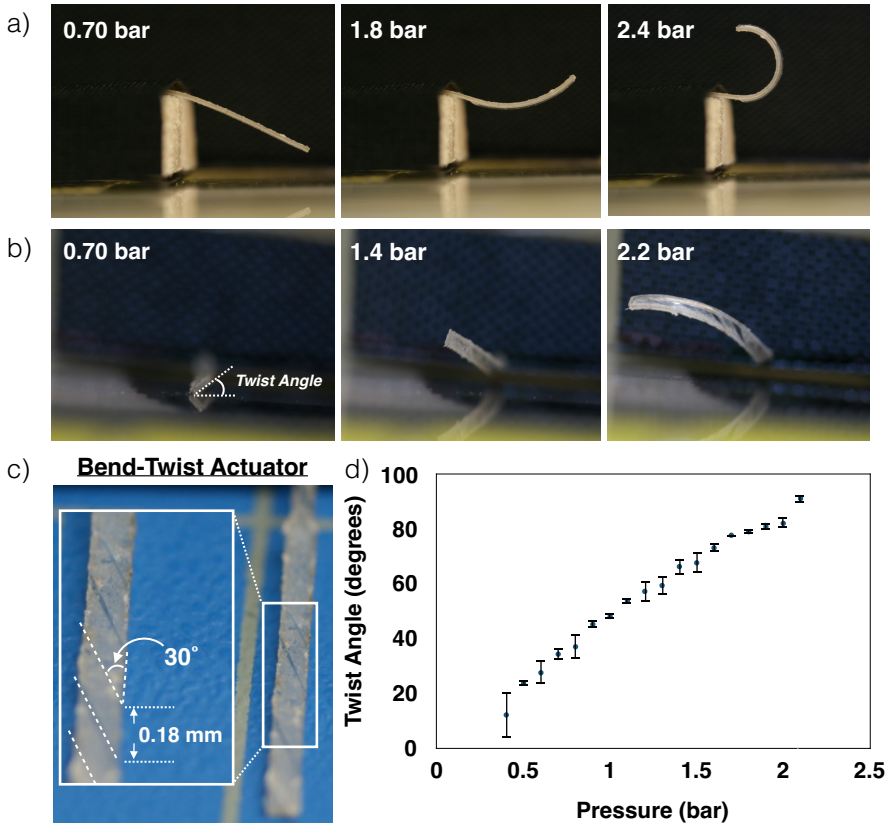


Figure 3.8: Composite micro-actuators. a) Pure bending, b) Bend-twist coupling c) Line pattern on bend-twist actuator d) Twist angle as a function of pressure. Error reported as SEM. n = 2 actuators.

3.6 Regulating actuator bending using nanofiber orientation

After demonstrating that nanofiber-reinforced composite actuators bend controllably under pneumatic pressurization (Figure 3.8a), we investigated whether varying fiber patterns could be used to achieve more complex bending modes. One mode of interest is the combination of bending and twisting. Prior studies on macro-scale fiber reinforced actuators have demonstrated that the twisting motion of a pneumatic actuator depends upon fiber orientation[59,149,170]. Similarly, Finio et al demonstrated that the maximum twist of a piezoelectric micro-actuator occurred when the anisotropic fibrous laminate was oriented at 45°; zero twist and torque were present at 0° or 90°[171]. Embedding monolithic fiber sheets oriented between 0° and 90° did not induce a twisting mode in composite micro-actuators. We hypothesized that the anisotropy of these sheets was too low to measure a twist. Thus, we predicted that incising a linear pattern onto a uniform nanotextile would induce a bending-twisting mode by reducing cross-coupling in the nonwoven fiber sheet, thereby amplifying anisotropy. To test this hypothesis, we fabricated a composite micro-actuator capable of bend-twist coupling by laser micromachining a pattern of parallel lines on the enclosed nanofiber sheet (Figure 3.8b). This approach was selected because laser cutting provided consistent control of line spacing and pattern uniformity.

Using a custom DPSS laser, lines spaced 0.18 mm apart were inscribed on a monolithic nanofiber sheet (Figure 3.8c). A three-layer actuator was prepared using the soft lithography process described in section 3.2.2. The sub-laminate containing the laser-cut fiber sheet was plasma bonded to the patterned layer at an angle of 30° from the longitudinal axis of the air channel. Although a 30° angle was chosen as a demonstration in this study, the relationship between fiber orientation angle and actuator twist will be analytically modeled and further discussed in the next chapter. The twist angle of bend-twist coupled composite actuators as a function of pressure is shown in Figure 3.8d (device was not tested to failure). This preliminary study suggests the potential for using laser patterning to

combine multiple actuation modes on the micro-scale. Future chapters will build upon this principle to generate multiple curvatures in a single actuator by varying fiber orientation.

3.7 Summary

In this chapter, we presented a novel class of fiber-reinforced soft micro-actuators. To fabricate these actuators, we used a novel manufacturing process combining soft lithography and rotary jet spinning. To our knowledge, this is the first demonstration of polymer nanofibers as a strain-limiting layer for micro-actuation. Our results indicate that the mechanical properties and radii of curvature for composite micro-actuators are impacted by nanofiber layer location and bulk fiber orientation. Three-layer fiber-reinforced devices were up to 2.3 times tougher than pure PDMS, while simultaneously preserving the elongation of the elastomer. Although composite actuators can be pressurized 30% higher than pure PDMS devices, no delamination is observed between the strain limiting nanofiber sheet and the PDMS matrix. Finally, by incising an angled pattern into monolithic nanofiber sheets, bend-twist coupling can be achieved for three-layer actuators. In subsequent chapters, we will: 1) expand our analytical model of nanofiber motion to capture additional actuator bending modes, 2) scale nanofiber-reinforced actuators from the microscale to the mesoscale, and 3) investigate the use of fiber-reinforced soft actuators in delicate grasping tasks.

4

Model-Driven Design of Nanofiber-Reinforced Soft Fluidic Actuators Capable of Complex 3D Motions

4.1 Introduction

Soft actuators are well-suited for manipulation, physiotherapy, and delicate grasping tasks due to their smooth motion, ease of fabrication, and compliant substrates[53]. The structure of such devices generally consists of an elastomeric bladder enclosing a hollow channel. As the actuator is pressurized (e.g., pneumatically or hydraulically), the channel expands and the actuator moves. This motion is directed using features such as an anisotropic cross-section, in which one side of the bladder is thicker or stiffer than the other (Figure 4.1a)[56,57]; the inclusion of stiff fibers or polymers[55,172] (Figure 4.1b-c); and a sleeve wrapped around the bladder[37,149] (Figure 4.1d). Incorporating yarns and fibers as strain-limiting structures is a simple method to control the motions that a soft actuator can achieve. Previous studies have used circumferentially positioned fibers to constrain radial expansion[60,173,36,174,55] (Figure 4.1c) and layered stiff filaments (e.g., glass fibers) in a more compliant matrix material to program bending using geometric anisotropy[175,176]. By varying the pitch[37,59,177], stiffness gradient[178], and material properties[179] of reinforcing fibers, it is possible to prescribe specific patterns of motion, including extension, radial expansion, contraction (Figure 4.1c), bending (Figure 4.1d), and twist (Figure 4.1b).

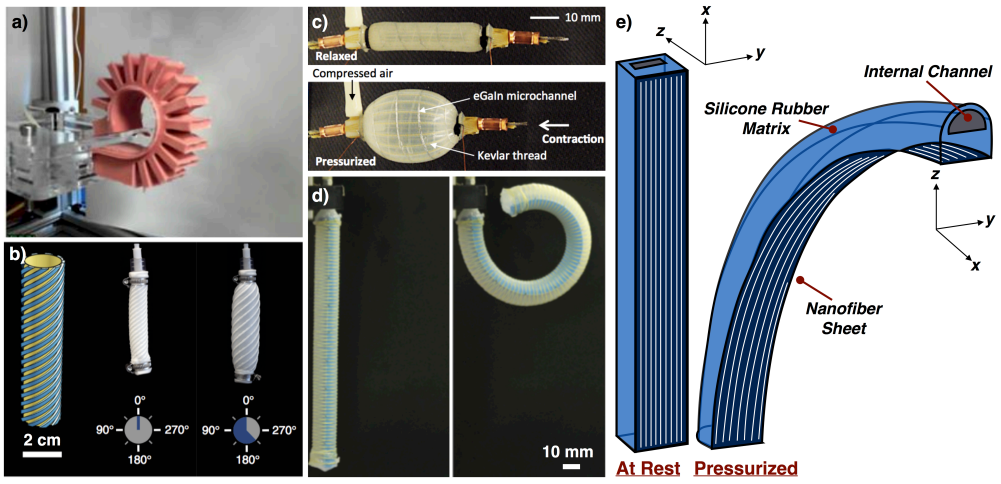


Figure 4.1: a) Bellows-style silicone rubber actuator exhibiting pure bending. Adapted from[56]. b) A 3D printed silicone actuator contracts due to reinforcement by stiffer polymer filaments. Adapted from[55]. c) Pneumatic elastomeric actuator reinforced with Kevlar fiber. Adapted from[172]. d) Cylindrical bending actuator whose motion is directed by Kevlar fiber wound helically around the exterior of the actuator. Adapted from[37]. e) Schematic of a nanofiber-reinforced silicone actuator. As the actuator is pressurized, the internal channel inflated and the device bends toward the (comparatively) stiff nanofiber sheet. In this illustration, a fiber orientation angle of 0° is shown.

Three-dimensional fiber integration strategies often require precise control of fiber pitch and placement; for example, a pair of antisymmetric yarns may be wound around a cylindrical bladder to induce bending or bending-extension coupling. Compared to this approach, it is more straightforward to incorporate two-dimensional textile sheets into actuator molding and soft lithographic manufacturing processes. Planar laminate structures (Figure A.10a) execute planned motions simply by varying the orientation of an anisotropic fiber array[180,177]. This approach has been used to develop flexible piezoelectric[171,181] and shape memory alloy[175,182,183,184] actuators featuring anisotropic carbon or glass fibers.

To extend the utility of composite laminate actuators into domains necessitating less rigid reinforcement fibers, we have demonstrated the fabrication and analytical modeling of soft nanofiber-reinforced fluidic actuators[180]. Previously, we derived an analytical model that facilitated design of actuators undergoing pure bending by correlating laminate geometry, input pressure, and actua-

tor curvature. To guide the development of soft actuators capable of both a wider range of motions (e.g., twisting, extension) and coupled behaviors (e.g., bend-twist coupling), a more comprehensive analytical model is needed. Here, we present a laminate plate theory model for nanofiber-reinforced elastomer actuators, demonstrate the correlation between analytical twist data and empirical results, and present proof-of-concept designs for actuators exhibiting multiple motions. This framework represents a simple, modular approach to designing and fabricating soft robotic devices with a variety of fiber orientations, layup designs, and bending motions.

4.2 Experimental Methods

4.2.1 Nanofiber fabrication using rotary jet spinning

Polymer nanofiber sheets were fabricated using rotary jet spinning. A solution of 3 wt./v% nylon-6 (Sigma-Aldrich, St. Louis, MO) / 3 wt./v% polyurethane (McMaster Carr, Princeton, NJ) in 1,1,1,3,3,3-hexafluoro-2-propanol (HFIP, Sigma-Aldrich, St. Louis, MO) was infused into a rotating reservoir using a syringe pump at a rate of 5 mL min^{-1}. A rotating cylindrical mandrel attached to a linear motor was used to collect uniform sheets of nonwoven fibers, as outlined in previous studies[99,86,180]. After collection, each sheet was removed from the mandrel and pressed for 10 min at 3000 lbs (applied over 132 cm^2) and 50°C using a laboratory compression molding press (Carver Laboratory Press, Wabash, IN). This process facilitates the integration of nanotextiles in the actuator manufacturing process by smoothing the fabric surface and removing wrinkles that form as the fiber sheet is removed from the collector.

4.2.2 Actuator design and fabrication

Nanofiber-reinforced actuators, illustrated in Figure 4.1e, were manufactured using a combination of molding and co-bonding, as shown in Figure 4.2. First, uncured silicone rubber (Dragon Skin 20,

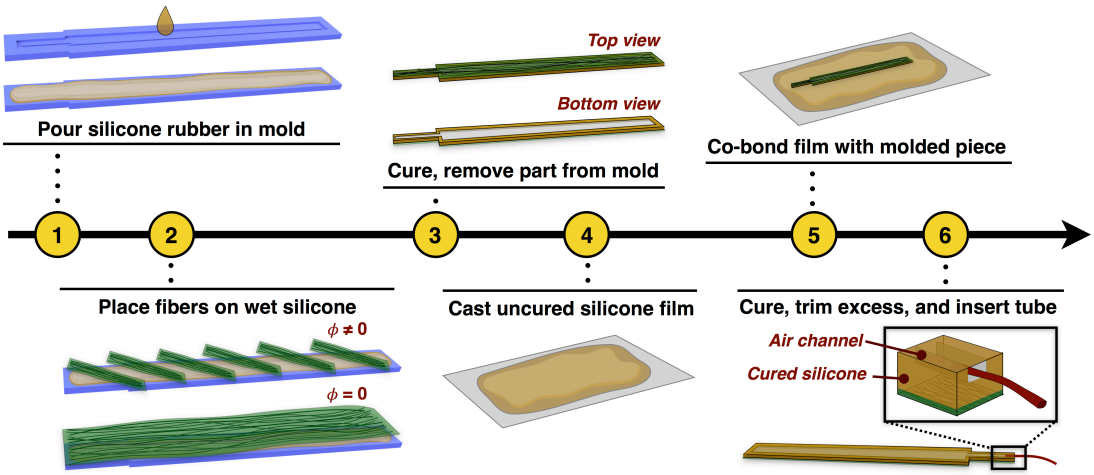


Figure 4.2: The manufacturing process of fiber-reinforced actuators involves molding silicone rubber components with oriented rotary jet spun polymer nanofiber sheets. Uncured silicone is poured into a 3D printed mold, and nanofibers are subsequently layered above it. After thermally curing the concave fiber/silicone structure, it is removed from the mold, co-bonded with a thin layer of uncured silicone, and thermally cured a second time. This step creates the internal hollow channel that will expand when the actuator is pressurized. Finally, a tube is inserted into the air channel of the completed actuator, and the surrounding aperture is sealed with epoxy.

Smooth-On Inc, Easton, PA) is poured into a custom-designed 3D printed mold. The mold is degassed in a vacuum chamber to remove residual air pockets, and a nanofiber sheet is then placed on top of the uncured silicone. If the fiber orientation angle (φ) is equal to 0 or 90 degrees, a solid fiber sheet is placed parallel or perpendicular, respectively, to the longitudinal axis of the mold. However, if $0° < \varphi < 90°$, strips of monolithic nanofabric are incised using a razor and placed at the desired angle. This approach is used because the anisotropy of a pristine nanofabric is too low to generate twist. Next, the assembly is thermally cured for 15 minutes at 75° C. The molds are subsequently removed from the oven, and the part is removed and cleaned. A thin layer of uncured silicone rubber is then deposited using a film applicator, and the molded part is co-bonded to this layer. This process seals a concave segment of the molded part, forming an internal air channel that will be used to pressurize the finished actuator. Finally, the co-bonded assembly is thermally cured (15 minutes, 75° C), and a tube is inserted and sealed into the air channel.

4.2.3 Laminate plate model for composite soft actuators

An analytical model was developed to describe the relationship between the laminate structure and bending motion of nanofiber-reinforced soft actuators. This composite laminate plate theory framework accounts for the material and mechanical properties of both the hyperelastic polymer matrix and the nonwoven textile reinforcement layer, as well as the input pressure to actuate the device. The assumptions included in this model are as follows: 1) perfect bonding and no slippage between lamina; 2) each layer is homogeneous, with known properties (the fiber layer is assumed to be orthotropic); 3) the elastomer matrix is incompressible; 4) the Young's moduli of the matrix and reinforcing fibers remain constant during pressurization; 5) the strain limiting layer is inextensible; and 6) gravity is neglected during actuator bending.

The midplane strains and curvatures ($\{\varepsilon^0\}$ and $\{\varepsilon^1\}$) of a cantilever actuator can be described by defining the relationship between the applied forces ($[N]$) and moments ($[M]$), and the laminate compliance matrix.

$$\begin{bmatrix} \{\varepsilon^0\} \\ \{\varepsilon^1\} \end{bmatrix} = \begin{bmatrix} A & B \\ B & D \end{bmatrix}^{-1} \begin{bmatrix} N \\ M \end{bmatrix} \tag{4.1}$$

The ABD matrix is a 6x6 matrix composed of three unique 3x3 matrices containing the following terms: extensional stiffnesses (A_{ij}), bending-extensional coupling stiffnesses (B_{ij}), and bending stiffnesses (D_{ij}).

$$\begin{bmatrix} \varepsilon^{o}_{xx} \\ \varepsilon^{o}_{yy} \\ \gamma^{o}_{xy} \\ \varepsilon^{I}_{xx} \\ \varepsilon^{I}_{yy} \\ \gamma^{I}_{xy} \end{bmatrix} = \begin{bmatrix} A_{11} & A_{12} & A_{16} & B_{11} & B_{12} & B_{16} \\ A_{12} & A_{22} & A_{26} & B_{12} & B_{22} & B_{26} \\ A_{16} & A_{26} & A_{66} & B_{16} & B_{26} & B_{66} \\ B_{11} & B_{12} & B_{16} & D_{11} & D_{12} & D_{16} \\ B_{12} & B_{22} & B_{26} & D_{12} & D_{22} & D_{26} \\ B_{16} & B_{26} & B_{66} & D_{16} & D_{26} & D_{66} \end{bmatrix}^{-1} \begin{bmatrix} N_x \\ N_y \\ N_{xy} \\ M_x \\ M_y \\ M_{xy} \end{bmatrix} \tag{4.2}$$

The components of these matrices are defined as follows (schematic shown in Figure A.10):

$$A_{ij} = \sum_n [\overline{Q}_{ij}]_n (z_n - z_{n-1}) \tag{4.3}$$

$$B_{ij} = \frac{1}{2} \sum_n [\overline{Q}_{ij}]_n (z_n^2 - z_{n-1}^2) \tag{4.4}$$

$$D_{ij} = \frac{1}{3} \sum_n [\overline{Q}_{ij}]_n (z_n^3 - z_{n-1}^3) \tag{4.5}$$

where the z-axis is positioned orthogonally to the laminate plane, z_n indicates the height of the n^{th} laminate layer with respect to the midplane of the structure, and $[\overline{Q}_{ij}]$ represents the transformed reduced stiffness matrix of the laminate. To calculate this matrix, we begin by defining the reduced stiffness matrix $[Q_{ij}]$ for a laminate material:

$$[Q_{ij}] = \begin{bmatrix} Q_{11} & Q_{12} & 0 \\ Q_{12} & Q_{22} & 0 \\ 0 & 0 & Q_{66} \end{bmatrix} \tag{4.6}$$

For an isotropic material, the following relations for the stiffness matrix coefficients are well-known. In these equations, E is the Young's modulus of the matrix, ν represents the Poisson's ratio,

and G is the shear modulus.

$$Q_{11} = Q_{22} = \frac{E}{1 - \nu^2} \tag{4.7}$$

$$Q_{12} = \frac{E\nu}{1 - \nu^2} \tag{4.8}$$

$$Q_{66} = \frac{E}{2(1 + \nu)} = G \tag{4.9}$$

Similarly, for an orthotropic material:

$$Q_{11} = \frac{E_1}{1 - \nu_{12}\nu_{21}} \tag{4.10}$$

$$Q_{12} = \frac{\nu_{12}E_2}{1 - \nu_{12}\nu_{21}} \tag{4.11}$$

$$Q_{22} = \frac{E_2}{1 - \nu_{12}\nu_{21}} \tag{4.12}$$

$$Q_{66} = G_{12} \tag{4.13}$$

Using the rule of mixtures, the longitudinal (E_1) and transverse (E_2) elastic moduli of the composite laminate can be calculated as:

$$E_1 = E_f V_f + E_m(1 - V_f) \tag{4.14}$$

$$E_2 = \frac{E_f E_m}{E_f(1 - V_f) + E_m V_f} \tag{4.15}$$

in which E_f and E_m are the Young's moduli of the nanofiber layer and elastomer matrix, respectively, and V_f is the volume fraction of the fiber layer. As the local angle of the embedded fiber sheet does not always coincide with the global coordinate axes of the laminate, a transformation matrix ($[T]$) was used to convert the compliance matrix between the local and global coordinate systems. Thus,

for fiber angle ϑ, $m = \cos\vartheta$, and $n = \sin\vartheta$, the transformed reduced stiffness matrix is defined as:

$$[T] = \begin{bmatrix} m^2 & n^2 & 2mn \\ n^2 & m^2 & -2mn \\ -mn & mn & m^2 - n^2 \end{bmatrix} \tag{4.16}$$

$$[\overline{Q}_{ij}] = [T]^{-1}[Q_{ij}][T]^{-T} \tag{4.17}$$

The individual fourth order terms of the 3x3 $[\overline{Q}_{ij}]$ matrix can be expressed as follows in expanded form:

$$[\overline{Q}_{ij}] = \begin{bmatrix} \overline{Q}_{11} & \overline{Q}_{12} & \overline{Q}_{16} \\ \overline{Q}_{12} & \overline{Q}_{22} & \overline{Q}_{26} \\ \overline{Q}_{16} & \overline{Q}_{26} & \overline{Q}_{66} \end{bmatrix} \tag{4.18}$$

$$\overline{Q}_{11} = Q_{11}\cos\vartheta^4 + 2(Q_{12} + 2Q_{66})\cos\vartheta^2\sin\vartheta^2 + Q_{22}\sin\vartheta^4 \tag{4.19}$$

$$\overline{Q}_{12} = \overline{Q}_{21} = Q_{12}(\cos\vartheta^4 + \sin\vartheta^4) + (Q_{11} + Q_{22} - 4Q_{66})(\cos\vartheta^2\sin\vartheta^2) \tag{4.20}$$

$$\overline{Q}_{16} = \overline{Q}_{61} = (Q_{11} - Q_{12} - 2Q_{66})\cos\vartheta^3\sin\vartheta - (Q_{22} - Q_{12} - 2Q_{66})\cos\vartheta\sin\vartheta^3 \tag{4.21}$$

$$\overline{Q}_{22} = Q_{11}\sin\vartheta^4 + 2(Q_{12} + 2Q_{66})\cos\vartheta^2\sin\vartheta^2 + Q_{22}\cos\vartheta^4 \tag{4.22}$$

$$\overline{Q}_{26} = \overline{Q}_{62} = (Q_{11} - Q_{12} - 2Q_{66})\cos\vartheta\sin\vartheta^3 - (Q_{22} - Q_{12} - 2Q_{66})\cos\vartheta^3\sin\vartheta \tag{4.23}$$

$$\overline{Q}_{66} = (Q_{11} + Q_{22} - 2Q_{12} - 2Q_{66})\cos\vartheta^2\sin\vartheta^2 + Q_{66}(\cos\vartheta^4 + \sin\vartheta^4) \tag{4.24}$$

Next, we consider the resultant force and moment of the inflating actuator, which will be included in the matrix $\begin{bmatrix} N \\ M \end{bmatrix}$. Because the resultant force describes actuator bending about the y-axis (orthogonal to the longitudinal x-axis of the device, as marked in Figure 4.1e), we assume that the

resultant force only incorporates forces applied along the x-axis. Thus, $N_y = N_z = 0$. N_x is defined by considering a static balance between the pressure (P) applied on the distal end cap and a traction force (σ_t, within the inflating membrane) that opposes this pressure. In the following expressions, s represents the arc length of the segment, t_m is the membrane thickness, and A_i indicates the total area of the inflating channel (schematic shown in Figure A.10). By considering the pressurized actuator as an incompressible Neo-Hookean material, we can derive σ_t using the invariant relationship between the three principal stretch ratios: $\lambda_1\lambda_2\lambda_3 = 1$. As outlined in a previous analysis[180] (and in Section 3.2.3), we assume that longitudinal expansion is negligible compared to axial and circumferential deformation and thus set $\lambda_1 = 1$. The circumferential (λ_2) and axial (λ_3) stretches are defined in terms of the geometry of the inflating membrane, where r indicates the radius of curvature of the circular sector defined by the inflating membrane, s indicates the membrane arc length, and $2a$ represents the width of the internal channel:

$$\lambda_2 = \frac{s}{2a} \tag{4.25}$$

$$= \frac{r\vartheta}{2a} \tag{4.26}$$

$$= \frac{r}{a}\sin^{-1}\frac{a}{r} \tag{4.27}$$

$$\lambda_3 = \frac{1}{\lambda_2} \tag{4.28}$$

Thus, the traction force can be written in terms of the principal stretches:

$$\sigma_t = \mu(\lambda_1^2 - \lambda_3^2) \tag{4.29}$$

$$= \mu(1 - (\frac{a}{r\sin^{-1}\frac{a}{r}})^2) \tag{4.30}$$

μ represents the shear modulus of the silicone membrane, defined using the relation $E_m = 3\mu$ (E_m is the membrane Young's modulus). Here, we assume that the shear modulus is constant throughout actuator pressurization. Therefore, the resultant force is defined as:

$$N_x = PA_i - \sigma_t s t_m \tag{4.31}$$

$$= PA_i - \mu(1 - (\frac{a}{r\sin^{-1}\frac{a}{r}})^2) s t_m \tag{4.32}$$

$$\tag{4.33}$$

The resultant moment, $\mathcal{M}_y$, can be expressed as the product of the resultant force (N_x) and its associated lever arm (d_r). To derive $\mathcal{M}_y$, we consider the moments produced by the pressure and traction forces. In the following equations, d_p represents the distance between the centroid of A_i to the neutral axis and d_t is the lever arm associated with the traction force within the inflating membrane. Using known values for d_p and d_t, we first solve for d_r and then calculate $\mathcal{M}_y$.

$$N_x d_r = PA_i d_p - \sigma_t s t_m d_t \tag{4.34}$$

$$d_r = \frac{PA_i d_p - \sigma_t s t_m d_t}{N_x} \tag{4.35}$$

$$= \frac{PA_i d_p - \mu(1 - (\frac{a}{r\sin^{-1}\frac{a}{r}})^2) s t_m d_t}{PA_i - \mu(1 - (\frac{a}{r\sin^{-1}\frac{a}{r}})^2) s t_m} \tag{4.36}$$

$$\mathcal{M}_y = N_x d_r \tag{4.37}$$

$$\tag{4.38}$$

Using the framework of this model, it is possible to design soft composite actuators with a variety of motions, including: pure bending, bend-twist coupling, and pure extension. To program a

specific actuator motion, we can vary laminate geometry (e.g., layer thickness, relative position) and the orientation of the strain-limiting nanofiber layer. Furthermore, by spatially controlling sections of the fiber orientations, we can create hybrid actuators that involve serial connections of different bending/twisting motions all connected to the same pressure source.

4.2.4 Actuator twist characterization

The curvature of nanofiber-reinforced actuators was recorded in air. Each actuator was positioned in a clamped-free configuration and pneumatically inflated using a pressure control apparatus. Images were taken at intervals of 1 psi using a Nikon D810, and analyzed using Fiji[185].

4.3 Results and Discussion

4.3.1 Examining Coupled Bending Modes

Our laminate plate theory framework facilitates design of composite actuators with a variety of single and coupled bending motions. By adjusting the geometric and material properties of the actuator and the nanofiber layer, we can tune the laminate compliance and achieve a desired movement. In a previous study, we derived an analytical model to predict actuator curvature as a function of laminate layup and material properties. The theoretical framework presented here extends predictive capabilities to motions other than pure bending. Specifically, we demonstrate the ability to design devices with coupled modes, such as bending-extension and bending-twisting.

It is possible to classify the bending mode exhibited by an actuator by examining the laminate compliance matrix. For a given laminate design and fiber orientation, the extensional (A_{ij}), bending-extensional coupling (B_{ij}) and bending stiffnesses (D_{ij}) provide insight on the resulting actuator motion. A_{16} and A_{26} denote shear-extension coupling; if these coefficients are 0, a laminate is balanced and symmetric. However, if the B_{ij} or D_{ij} matrices (namely D_{16}, D_{26}) are nonzero, the device

Table 4.1: Impact of laminate layup on extensional, bending, and bending-extensional coupling stiffnesses.

Laminate Design	A_{16}, A_{26}	B_{ij}	D_{16}, D_{26}
No Nanofibers	0	0	0
+ Nanofibers ($\varphi = 0°$)	0	Nonzero	0
+ Nanofibers ($0° < \varphi < 90°$)	Nonzero	Nonzero	Nonzero

will display bend-extension coupling or bend-twist coupling, respectively. Table 4.1 displays details on the value of these three sets of terms for three soft actuator designs: no nanofibers (elastomer matrix only), with a nanofiber layer oriented at 0°, and with a nanofiber layer oriented between $0° < \varphi < 90°$. Without the strain-limiting nanofabric, and if the inflating chamber is placed at the neutral axis, the actuator is balanced and experiences no bend-extension or bend-twist coupling. When a fiber layer is added parallel to the longitudinal axis ($\varphi = 0°$), the laminate experiences nonzero bend-extension coupling, but no twist. Finally, incorporating an angled nanofiber sheet introduces bend-twist coupling.

4.3.2 Modeling Bend-Twist Coupling

To further understand the magnitude of coupling behavior that the actuator exhibits, it is necessary to perform additional calculations. Of the canonical coupling modes, we chose to examine bending-twisting because it is particularly challenging to achieve using soft composite laminates in the absence of anisotropic layers. We predicted bend-twist coupling of fiber-reinforced elastomer actuators using our analytical model and then validated these results empirically. In this analysis, we assumed a constant actuator curvature and focused on the angle of twist (ϑ) at the distal end of each fiber-reinforced actuator. ϑ can be defined using the midplane flexural strain (γ^1_{xy}) of the actuator, which relates to the device's vertical displacement along the z axis.

$$\vartheta = \tan^{-1}\left(\frac{\partial z}{\partial y}|_{x=L}\right) \tag{4.39}$$

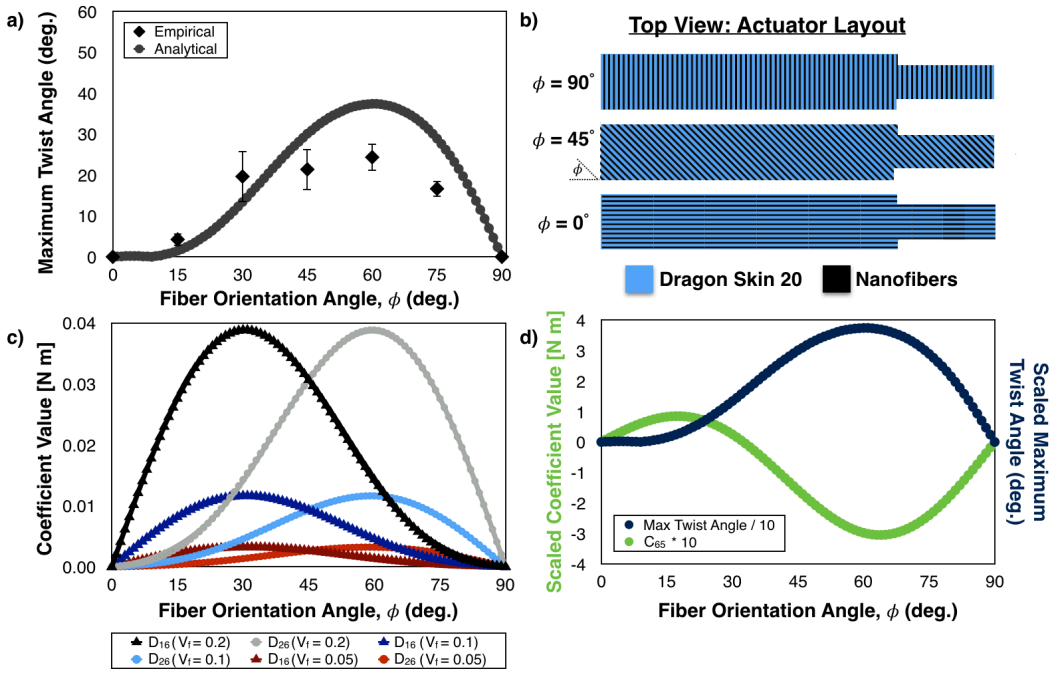


Figure 4.3: a) Theoretical maximum actuator twist angle as a function of nanofiber orientation. Error is shown as standard error of the mean. n = 2-3 actuators per condition. b) Illustration of various fiber alignment schemes. c) Bend-twist coupling coefficients as a function of fiber orientation angle (φ) and fiber volume fraction (V_f). d) Coefficient C_{65} and the maximum actuator twist as a function of fiber orientation angle. A higher magnitude for the C_{65} signifies greater actuator twist. To more easily visualize both data sets on the same plot, C_{65} is scaled up by a factor of 10 and the maximum twist is scaled down by the same factor.

Based on our assumption of constant curvature along the length (L) of each actuator, the integral used to calculate the slope at the distal tip simplified as per a previous analysis[171]:

$$\vartheta = \tan^{-1}\left(\int_0^L \gamma_{xy}^1 dx\right) \tag{4.40}$$

$$= \tan^{-1}(\gamma_{xy}^1 L) \tag{4.41}$$

For an actuator of fixed dimensions, outlined in Section 4.3.1, and an embedded nanofiber sheet with E = 5.23 MPa, we modeled the maximum twist angle as a function of fiber orientation. Nanofiber

orientation angle was varied from 0 to 90 degrees in 15 degree intervals, and the theoretical maximum twist angle occurs at 60 degrees (Figure 4.3a). Given that actuator stiffness is governed primarily by the laminate (and not the comparatively thin inflating membrane), we can assume that the degree and symmetry of actuator twist as a function of fiber orientation angle depends upon the stiffness matrix coefficients. While the model slightly overestimates the empirical data, the analytical results capture the trend, including the skewness toward higher ($\varphi > 45$ degrees) fiber orientation angles. A potential explanation for the minor overestimation may be the empirically derived material constants used as model inputs; this topic is discussed further in the Supplemental Materials (Figure A.11). Figure 4.3b illustrates the orientation of three sample fiber alignments, as defined by the model. To better understand the analytical trend, we examined the bend-twist coupling terms, D_{16} and D_{26}, in the laminate compliance matrix. As described in Section 3.1, a nonzero value for these coefficients indicates the presence of bend-twist coupling. Like the maximum actuator twist angle, the values of D_{26} are skewed slightly to the right with a peak at 60° (Figure 4.3c). A higher magnitude for this coefficient indicates that the actuator will experience a larger bending moment for a given twisting curvature. While the values of both coefficients increase with the volume fraction of nanofibers in the actuator (V_f), their trends remain similar. Since the volume fraction of fibers in the laminate is low (0.05), the difference between the twisting coefficients at $\varphi = 60$ degrees and at $\varphi = 0, 90$ degrees is also relatively low. However, the difference is more pronounced at higher fiber volume fractions.

To further examine the relation between the coupling terms, the curvatures, and resultant moments, we can refer to Eqn. 4.2. To simplify our discussion, let $[ABD]^{-1} = [C]$, the compliance matrix. Recall our assumptions that there are no resultant shear forces ($N_{xy} = 0$), and that the resultant normal force acts along the longitudinal (x) axis of the actuator ($N_y = 0$). Moreover, the asymmetric nanofibers lead to nonzero coupling elements in the ABD matrix, which will in turn reflect the twist generated as the actuator bends about the y-axis; thus, $M_y \neq 0$, and we assume

$M_x = M_{xy} = 0$.

$$\begin{bmatrix} \varepsilon^{o}_{xx} \\ \varepsilon^{o}_{yy} \\ \gamma^{o}_{xy} \\ \varepsilon^{I}_{xx} \\ \varepsilon^{I}_{yy} \\ \gamma^{I}_{xy} \end{bmatrix} = \begin{bmatrix} C_{11} & C_{12} & C_{13} & C_{14} & C_{15} & C_{16} \\ C_{21} & C_{22} & C_{23} & C_{24} & C_{25} & C_{26} \\ C_{31} & C_{32} & C_{33} & C_{34} & C_{35} & C_{36} \\ C_{41} & C_{42} & C_{43} & C_{44} & C_{45} & C_{46} \\ C_{51} & C_{52} & C_{53} & C_{54} & C_{55} & C_{56} \\ C_{61} & C_{62} & C_{63} & C_{64} & C_{65} & C_{66} \end{bmatrix} \begin{bmatrix} N_x \\ 0 \\ 0 \\ 0 \\ M_y \\ 0 \end{bmatrix} \tag{4.42}$$

Consequently, the calculation of γ^{I}_{xy} to determine the actuator twist angle is a function of only two elements in $[C]$: coefficients C_{61} and C_{65}. Thus, of the two elements governing bend-twist coupling, we can focus on C_{65} for our current analytical formulation. Figure 4.3d displays the values of this element and the maximum actuator twist as a function of fiber orientation angle. To more easily compare both data sets on the same plot, the inverted coefficient values are scaled up by 10 and the maximum twist values are scaled down by a factor of 10. A larger magnitude of C_{65} signifies a larger actuator twist. The highest magnitude for both the twist values and the inverted coefficient are both located around $\varphi = 60$ degrees.

To validate these analytical predictions, test actuators were fabricated with a fiber orientation angle of 60 degrees (Figure 4.4a) and pressurized pneumatically from 0 to 5 psi (Figure 4.4b-c). A 60 degree fiber angle was selected because the analytical model predicted a maximum twist for this value. To simplify photographic measurement of the tip twist angle, the middle region of a 15 cm actuator was gently clamped (memory foam lining the clamp facilitated channel inflation, but not bending) with 4 cm of the distal end exposed. This section was able to move and twist freely during pressurization. While the analytical model predicts a more rapid increase in twist angle as a function of pressure compared to the empirical results, the predicted twist angles (albeit the value at 1 psi) fall

within a 95% confidence interval. It is possible that the dynamics of actuator inflation become increasingly nonlinear in two regimes: under low pressure (∼1 psi) as the device begins to inflate, and as the actuator approaches maximum pressurization (∼5 psi). Although the model assumes homogeneous distribution of strain-limiting nanofibers, compliant actuators may be more sensitive to the location of the fiber strips during empirical trials, particularly at low input pressure. For example, a lack of fiber strips placed directly over the distal channel cap may enable the distal region to generate higher moment and potentially increase the tip twist under low applied pressure. Future work can eliminate the potential for such variation between samples by using precision dowel pins to position nanofiber strips on the silicone matrix. Within the range of moderate actuator inflation (2-4 psi), the theoretical twist values capture the trend of the experimental data. This analytical model assumes that actuator inflation occurs symmetrically and only at the top of the internal channel; these assumptions may result in the overestimate of actuator twist at high pressure, when the actuator is most inflated. In practice, the compliant nature of the silicone matrix results in distention across other areas of the actuator cross-section, including the bottom of the laminate. Inflation at both the top and bottom of the internal channel can be observed in Figure 4.4c when the actuator is pressurized at 5 psi. Future studies may further improve analytical modeling by assessing other nonlinear elastic models and examining the geometry of the pressurized actuator channel using finite element method simulations.

4.3.3 Fabricating Actuators with Complex Motions

By varying the orientation of the nanofiber layer, we can bias the motion of composite actuators along specific directions. In addition to tuning fiber alignment with respect to the longitudinal actuator axis, it is possible to design and fabricate actuators with multiple discrete regions along the length of each device. Figure 4.5a depicts two examples: i) a pure bending region adjacent to a bending-twisting region, and ii) two distinct bending-twisting zones. While our analytical model

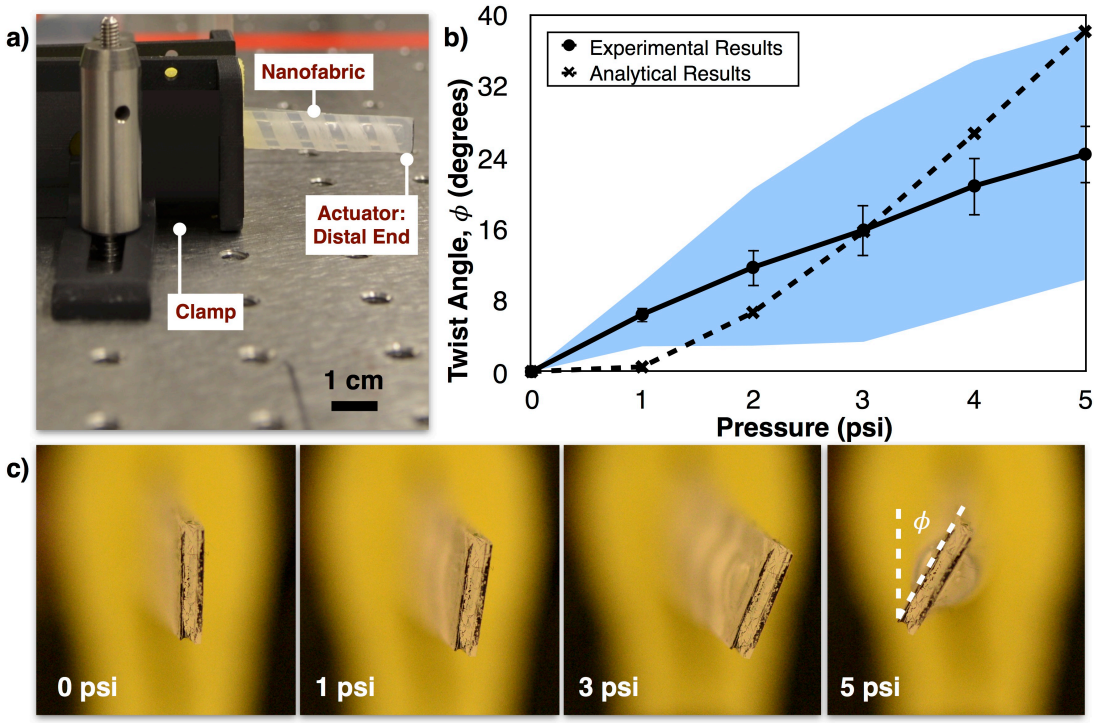


Figure 4.4: Twisting nanofiber-reinforced actuators. Twisting nanofiber-reinforced actuators. a) Setup of soft actuator for empirical testing. In this experiment, the fiber orientation angle for all actuators was 60 degrees. b) Theoretical and empirical results for actuator twist angle (φ) as a function of pressure. n = 3 actuators, error is calculated as standard error of the mean. 95% confidence interval shown in blue. c) Images of actuator distal tip during pressurization and twisting. The distal tip of the actuator is marked with black ink to more clearly delineate its position.

neglects gravity, Figure 4.5 shows these proof-of-concept actuators in a suspended configuration to display their motion more clearly. Both hybrid actuators are partially pressurized to 1-2 psi. A solid nanofiber sheet oriented at 0° experiences pure bending when inflated, while diagonal fiber strips allow the distal actuator tip to twist out of plane (Figure 4.5b). In this setup, suspension of the actuator has resulted in reduced bending of the top section due to gravitational forces. By juxtaposing pure bending and bending-twisting regions, mixed bending modes can be incorporated on the same actuator for grasping tasks. Moreover, reinforcing an actuator with fibers in two separate orientations (Figure 4.5c) generates twist in two opposing directions. Under the low operating pressures (1-2 psi) imposed in this preliminary study, the distal tip angle remained approximately constant.

In this configuration, the actuator remains asymmetric and would also bend under higher pressure. These proofs-of-concept represent only a few examples of the myriad combinations that can be fabricated by varying nanofabric orientation. Based on a specific task, it is possible to design an actuator to achieve the desired bending modes, to predict motion of each discrete segment using the model presented here, and to fabricate the structure accordingly.

4.4 Summary

In this chapter, we have presented an analytical model for soft nanofiber-reinforced fluidic actuators that correlates fiber orientation angle and laminate geometry with motions such as bend-twist coupling. This laminate plate theory framework can be used to predict both simple (e.g., pure bending) and coupled (e.g., bend-twist, bend-extension) actuator motions as a function of applied pressure, fiber and matrix stiffness, device geometry, and nanofiber orientation. Experimental validation of actuator twist demonstrates good agreement with theoretical results. To perform empirical tests, we have also developed a novel fabrication process for mesoscale soft actuators, using polymer nanofibers as a strain-limiting layer. The model derived here can be used to design composite actuators with arbitrary fiber orientations to fit specific motions or material criteria. These capabilities facilitate development of soft robotic actuators for a wide range of applications, tasks, and domains of use. In the following chapter, we will combine several composite soft actuators to form a gentle gripping device, characterize its performance using laboratory tank testing, and demonstrate its effectiveness for delicate manipulation of fragile objects.

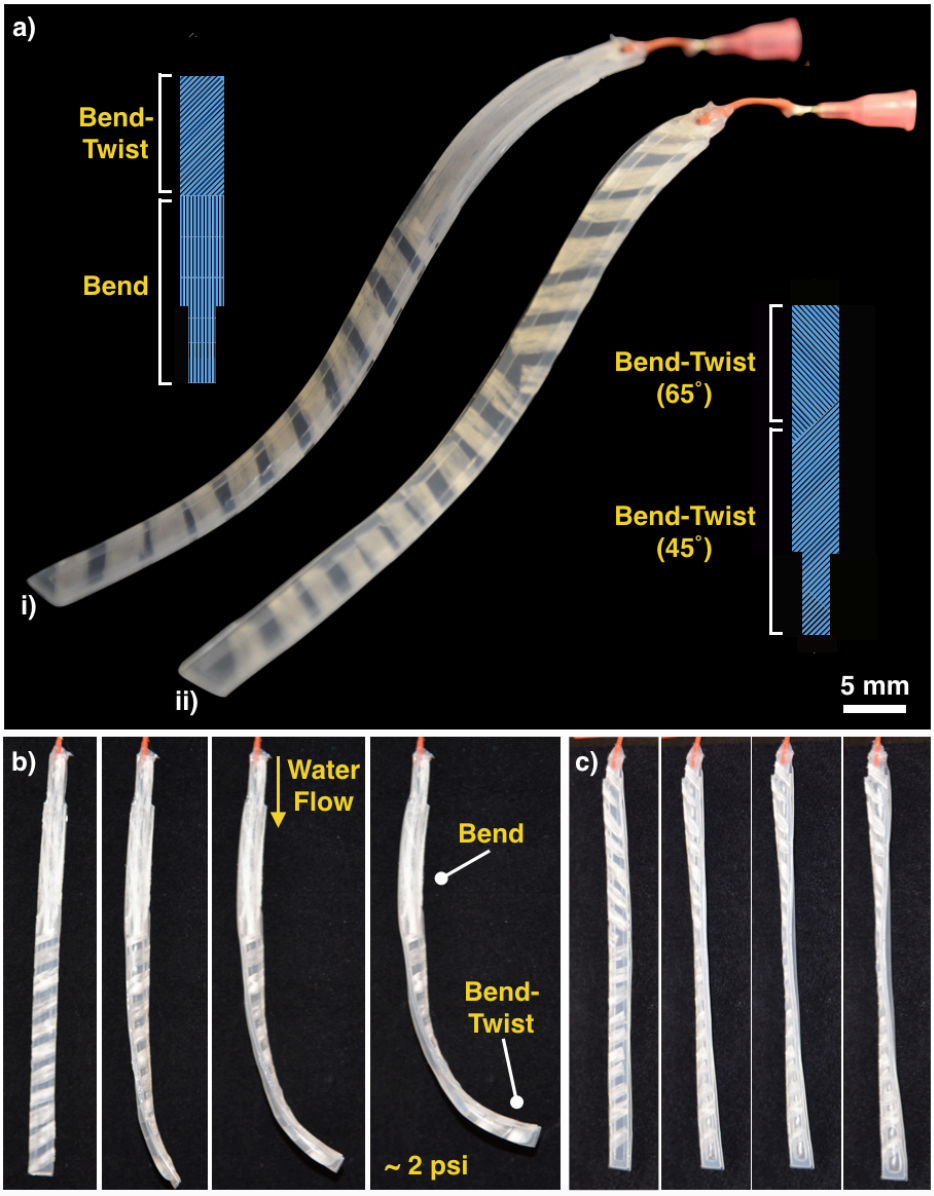


Figure 4.5: a) Hybrid motion actuators with, from left: (*i*) bend and bend-twist sections, and (*ii*) bend-twist coupling with two fiber orientations. b) Diagonally oriented fiber strips enable the distal end to twist, while a solid fabric sheet restricts the opposite end from twisting. Actuator pressurized from rest to $\sim$ 2 psi. c) Placing fibers in opposing orientations allows actuators to twist bi-directionally. Device pressurized from rest to $\sim$ 1 psi.

5

Ultra-Gentle Manipulation of Delicate Structures using a Soft Robotic Gripper

5.1 Introduction

The marine environment has long been a deep well of bioinspiration for novel materials and structures[186,187,188], and cutting-edge medical treatments[189,190], but it is less common for these inventions

to also have practical applications toward the biology and ecology of the animals that are the source of bioinspiration. Gelatinous macroplankton including cnidarian medusae, ctenophores and pelagic tunicates are becoming increasing recognized as key ecosystem consumers of energy and nutrients[191,192] and are estimated to constitute a global biomass of 38.3 Tg C[193]. For many years gelatinous zooplankton were overlooked by marine scientists, largely due to lack of delicate equipment to study them, and have been referred to as "forgotten fauna"[194]. Discoveries such as lifecycle reversal[195] and Green Fluorescent Protein[196,197] are two such examples of findings from gelatinous zooplankton that have cross-disciplinary impacts and demonstrate the importance of learning more about these lifeforms.

In spite of this vast potential, collecting intact samples of gelatinous organisms to study remains extremely challenging. Jellyfish are composed of over 95 percent water, and their mesogleal tissue has an extremely low stiffness (Young's modulus of 0.34-1.2 kPa)[198,199,200,201]. Capturing these delicate creatures in the ocean has been a challenge for the research community because existing technologies (e.g., nets and vacuum devices) frequently damage them in the grasping process[202,194]. The ideal grasping device for delicate materials in dynamic domains must incorporate a soft and flexible interface, compliant yet tough appendages, and a radius of curvature compatible with the target size. This work focuses on developing a soft gripper with such properties. The target organisms for this device are three small (roughly 7-10 cm) jellyfish species: *Aurelia aurita*, *Catostylus mosaicus*, and *Mastigias papua*. Jellyfish present extreme challenges for delicate grasping and manipulation, and lessons learned from this exploration can undoubtedly be transferred to other tasks involving fragile, gelatinous, or mixed-phase objects.

Currently, state-of-the-art aquatic grippers can be classified in five categories: 1) forked metal or plastic manipulators[203,204], 2) soft hydraulic actuators[30,205], 3) jamming grippers[206], 4) suction samplers[207], and 5) non-contact containers that close around a swimming animal. Metal or plastic grippers are the most widespread marine sampling method, but the rigid surface can snag or compress

gelatinous animals, and a fixed radius of curvature is unable to conform controllably to the shape of amorphous or soft-bodied animals[208]. Foam-coated hydraulic actuators have significantly improved nondestructive sampling of delicate benthic and midwater animals (e.g., coral, sea stars) by decreasing grip force while increasing pressure distribution[30]. However, the contact pressure exerted by foam-covered actuators (1-10 kPa) is too high to grasp gelatinous animals without causing harm (Figure A.12). While particle jamming grippers are capable of lifting sedentary objects, their operating mechanism is not well-suited for grasping floating organisms[15,206]. Suction samplers use a pump to draw an untethered animal through an inlet tube and into a storage container; however, delicate organisms can be damaged as they move through the tubing[209,210]. Finally, non-contact tools such as the Detritus Sampler ("D-Sampler") or the RAD (rotary-actuated dodecahedron) Sampler are open containers which are positioned near floating specimens and then closed around the organism. Use of the D-Sampler with remotely operated vehicles (ROVs) is challenging because the container is typically positioned by moving the entire vehicle[209,211]. Moreover, although the RAD Sampler[209] has successfully captured centimeter-scale squid and octopi, misalignment of the container can cleave the tentacles of fragile specimens. A flexible, compliant gripper is needed to bridge this capability gap, thereby achieving nondestructive grasping of gelatinous marine organisms. In this chapter, we report a novel approach for gentle grasping using nanofiber-reinforced soft actuators.

Our grasping device is composed of six composite actuator "fingers" connected to a 3D printed "palm" produced using a PolyJet-based printer (Objet Connex500, Stratasys, Edina, MN, USA). Each actuator contains an elastic yet tough silicone rubber matrix and a strain-limiting layer of flexible polymer nanofibers. The gripper is lightweight (123 g) and can be actuated using very low hydraulic pressure (1-6 psi). Upon pressurization, a channel within each actuator inflates and the appendage bends in the direction of the stiffer fiber-reinforced layer. Inflation of several actuators spaced around a marine organism enables the animal to be gently cradled by the soft silicone digits.

The actuators overlap and contact one another, forming a soft network which restricts the position of the target but does not fully immobilize it[212]; this caging grasp reduces the need to precisely control individual finger placement, and instead relies on collective inflation of all actuators. The low contact pressure exerted by each actuator (0.0455 ± 0.007 kPa) also facilitates nondestructive interaction. To better understand the device's performance space, we have empirically identified the region of acquisition using a synthetic target and quantified the resistance to forces on the object during a grasp. The soft gripper can be adapted both to deep-sea exploration using a remotely operated vehicle (Figure 5.1a) and to portable specimen collection in the shallower waters of the photic zone. Finally, we demonstrate the use of the portable device setup to successfully grasp three jellyfish species (Figure 5.1b-d).

5.2 Experimental Methods

5.2.1 Fabrication of Nanofiber-Reinforced Soft Actuators

The objective of this study is to design and fabricate a gentle gripper capable of nondestructive sampling of soft-bodied marine organisms. Previously, we developed flexible and robust micro-scale soft actuators composed of an elastomer matrix reinforced with polymer nanofibers[180]. Nanofibers were selected as the strain-limiting layer due to their ease of processing, high specific strength, and slim profile (the latter quality is important for micro-scale manipulation); the actuators underwent large deformations without requiring stiffer reinforcing materials, such as carbon or glass fibers. Furthermore, the nanofabric's high surface area facilitated bonding with elastomeric materials during the fabrication processes, and demonstrated no delamination from the matrix following tensile testing of the actuator to failure. Here, we leverage the scalability, durability, and flexibility of these materials by engineering meso-scale elastomeric hydraulic actuators using a silicone matrix reinforced by tough and elastic nylon/polyurethane nanofibers.

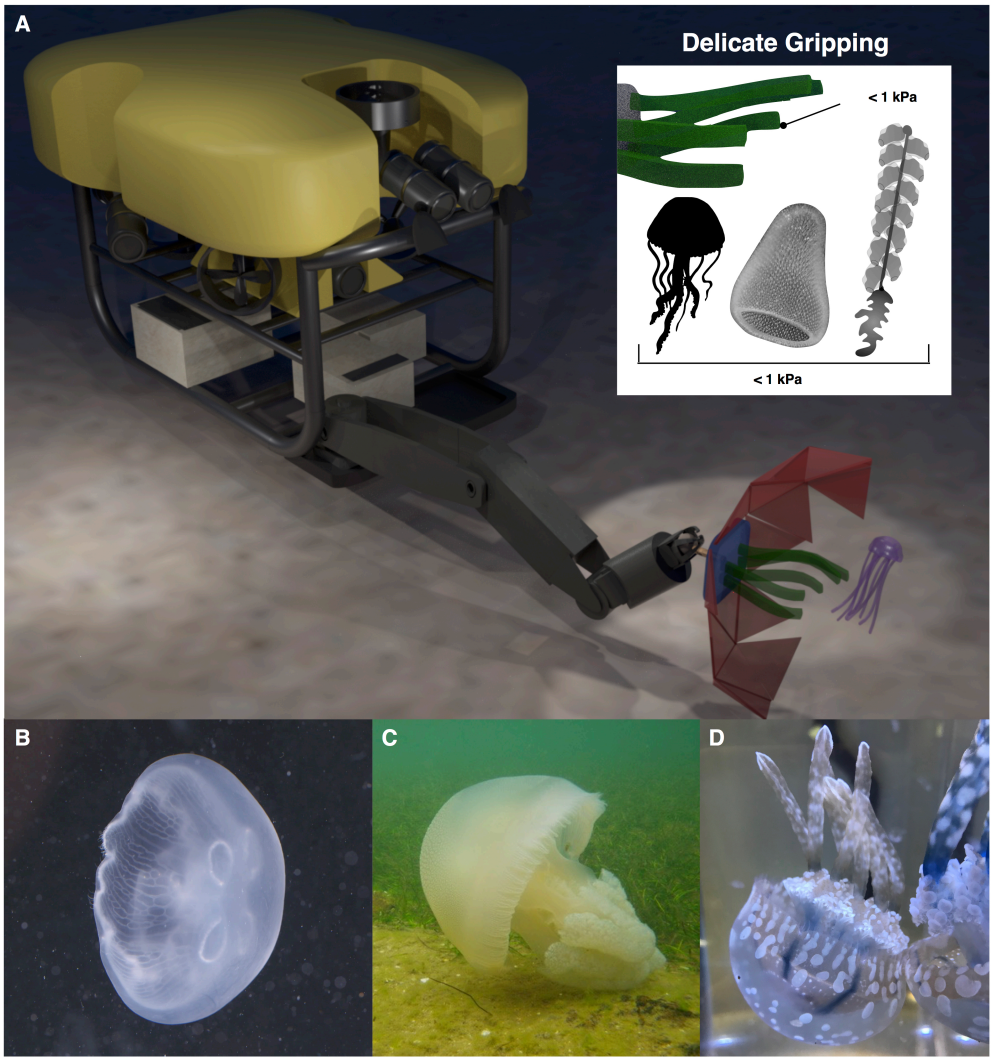


Figure 5.1: a) Illustration demonstrating soft robotic actuators (in green) attached to a remotely operated vehicle. These actuators are designed for ultra-gentle manipulation of delicate tissues, such as jellyfish and other gelatinous marine species. The target species for our soft gripper are: b) *Aurelia aurita*, c) *Catostylus mosaicus* (Courtesy of Peter Campbell in Wikimedia Commons), and d) *Mastigias papua*.

3 wt./v% nylon-6 (Nylon 6, Sigma-Aldrich, St. Louis, MO) / 3 wt./v% polyurethane (McMaster Carr, Princeton, NJ) nanofabric sheets were manufactured and post-processed according to protocols discussed in Section 3.2.1 and in previous studies[180,99,86]. Composite soft actuators were fabricated as per the approach outlined in Section 4.2.2 (Figure 5.2a). First, the lower portion of the actuator is fabricated. Uncured silicone rubber (Dragon Skin 20, Smooth-On Inc, Easton, PA) was poured into a custom-designed 3D-printed mold, and the assembly was de-gassed in a vacuum chamber for 10 minutes. Next, a nanofiber sheet was placed on the mold, enabling the uncured silicone to permeate the fabric. For all tank and field studies, pristine fiber sheets were embedded into soft actuators at a fiber orientation angle of 0 degrees (parallel to the longitudinal axis of the actuator). The component was thermally cured at 75°C for 15 minutes and removed from the mold. Then, the upper portion of the actuator (a thin membrane enclosing the internal channel) was fabricated. A layer of uncured silicone was generated using a film applicator, and the cured component was placed onto this film. By co-bonding the upper and lower parts together, we formed the internal channel that will be pressurized to actuate each device. Finally, the components were thermally cured (75°C, 15 minutes), tubing was inserted into the channel opening, and the area around the tubing was sealed with epoxy (Sil-Poxy, Smooth-On Inc, Easton, PA). For selected field tests, several drops of Smooth-On Silc Pig silicone dye was added to the uncured Dragon Skin 20 during actuator production; the purpose of this pigment was to improve the visual contrast between the soft actuators and surrounding water. The minute volume of dye added to the mixture did not impact thermal curing of the silicone rubber.

5.2.2 Laboratory Evaluation of Gripper Performance

We evaluated the performance of our ultra-gentle robotic gripper using a custom-built testing platform designed for repeated testing of underwater grasping operations. The underwater environment is a glass tank of approximately 60 cm wide by 180 cm long by 75 cm tall filled with tap water.

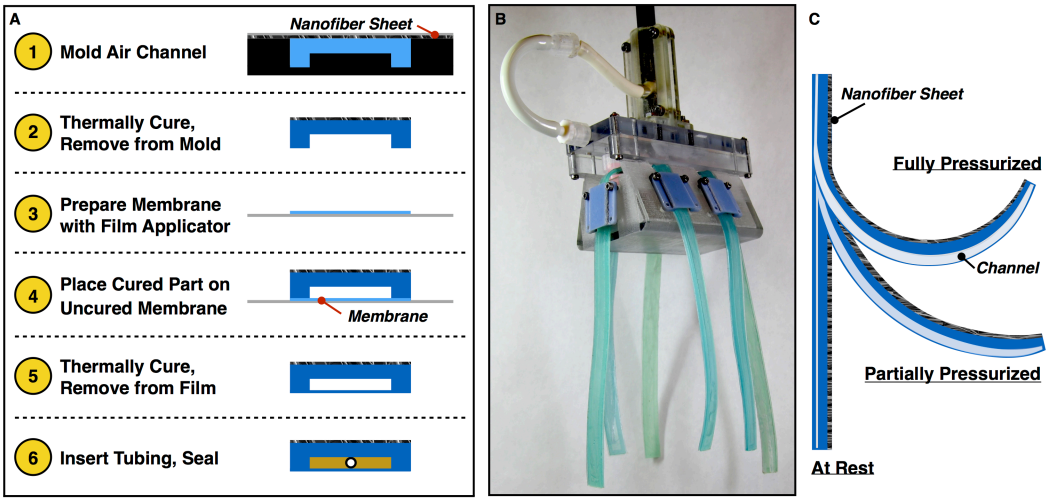


Figure 5.2: a) Nanofiber-reinforced soft actuators are manufactured using molding and co-bonding (cross-sectional view shown). b) Six soft actuators connected to a 3D printed hub. c) As an actuator is pressurized, the internal channel inflates and the device bends toward the strain-limiting nanofiber layer.

To position the gripper in three-dimensional space, a custom three-axis gantry is mounted above the tank, with an arm extending down into the tank. The gripper is mounted to this arm, and can be positioned within a 100 by 40 by 50 cm region inside the tank. The soft actuators are driven hydraulically with a custom control system that supplied the actuators with precise input pressure. The target object (a synthetic jellyfish made of soft silicone rubber) is positioned away from the walls of the tank using a thin tube connected to a positioning wall. Finally, to ensure precise re-positioning of the target object before each grasp attempt, the target object was mounted on a Kevlar tether which is routed out of the tank via a low-friction pulley system. When force is applied to the tether, the target is moved back to its initial position. Robot Operating System (ROS,[213]) was used to coordinate motion, pressure control, and a camera for documentation purposes.

5.3 Design Criteria for Ultra-Gentle Gripper

The objective for this device is to perform nondestructive grasping of gelatinous marine organisms in the marine environment. We can identify several performance requirements to ensure successful function. First, since the gripper will be fully submerged in the ocean during operation, it must be composed of materials that are resistant to corrosion in salt water. To fulfill this aim, we selected a silicone rubber matrix, nylon and polyurethane reinforcing fiber, PolyJet palm chassis, and stainless steel fasteners, each of which is undamaged by seawater immersion[214,215,216]. Second, the materials must withstand use at typical ocean temperatures, which reach a minimum of 0-3°C in the deep sea (several thousand meters) and a surface average of 17°C. The operational range of all the materials listed above is within this window; for example, silicone rubbers are highly resistant to low temperatures and possess an embrittlement temperature between -20 and -30°C[217]. Due to the design of the hydraulic pump used to inflate the soft fingers[30], pressure within the actuators is equalized to that of the surrounding waters and is therefore not a barrier to operation.

The following design criteria relates to the organisms that the gripper will be required to interact with. The actuator length must be determined by the average size of the intended object or species. While gelatinous animals exist in a variety of shapes and sizes, we selected three of the most widely studied jellyfish species to serve as models: *Aurelia aurita* (also called the "moon jellyfish"), *Catostylus mosaicus* (the "blue blubber"), and *Mastigias papua*. The average bell diameter for these species is 7-10 cm[218,219]. The total length for our composite soft actuators must exceed this amount, and was set at 15 cm. However, the size of the actuators may be easily scaled to accommodate larger or smaller organisms. Larger actuators may require thicker nanofiber sheets near the distal tip to maintain uniform curvature throughout the length of the actuator; during extended operation, a small amount of air can become trapped in this location, leading to higher local inflation of the membrane and lower curvature at the distal end. Finally, to execute a nondestructive grasp, the contact pressure ex-

erted by each actuator should be below 1kPa, the current state-of-the-art for soft marine grippers[30]. We will evaluate the pressure exerted by our composite actuators in a subsequent section.

5.3.1 Robotic Palm Design

The soft robotic gripper includes six modular actuators attached to a custom-designed, 3D-printed hub (Figure 5.2b) composed of a transparent photopolymer (RGD720, Stratasys, Eden Prairie, MN). The appendages are individually attached to the central palm and may be removed or exchanged in the case of actuator failure or to experiment with different digit configurations. The set of actuators are pressurized hydraulically (Figure 5.2c) using a single channel at the back of the hub, which can be attached to a fluid source using quick-disconnect fittings. In the present configuration, the actuators are evenly spaced, with two on either side of a 78 mm rectangular palm and one on either end of the opposite 45 mm edge. This layout was chosen because adhesion and friction between actuators on either side of the hub results in a strong caging grasp (Figure A.14). The actuators placed at the top and bottom of the palm prevent a target object from being released on either end, and contribute to a caging grasp by overlapping the center actuators. Actuator position can be rapidly adjusted by modifying the hub design. The low cost of fabricating a palm using additive manufacturing supports iterative development of soft grippers with varying numbers and positions of actuators (e.g., a hexagonal hub with six actuators, or a circular palm with ten digits). This flexibility can enable further customization to support organisms with specific shapes and symmetries.

5.3.2 Actuator Design

Understanding the impact of geometric and process variables during actuator fabrication is crucial to regulating input pressure range and reducing manufacturing defects (e.g., nonuniform sections of cured silicone components). Three key metrics toward achieving these goals are: interior chan-

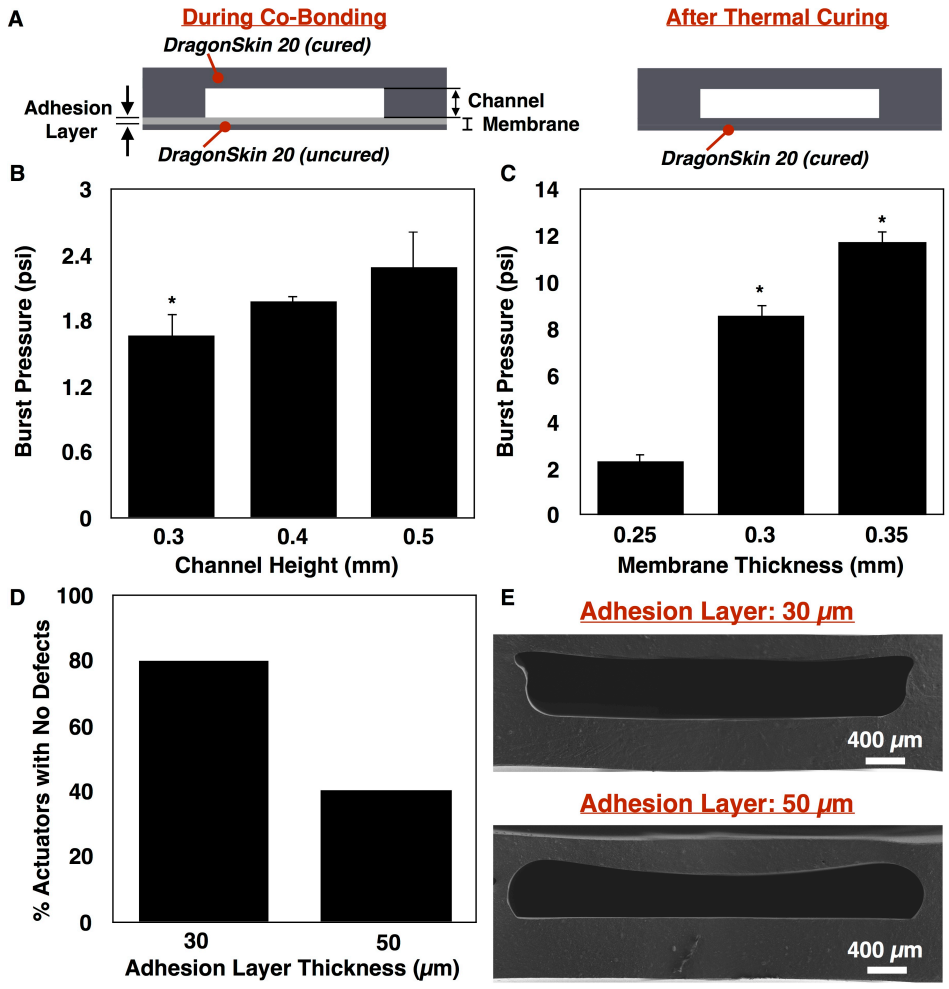


Figure 5.3: a) Co-bonding cured actuator section to uncured silicone layer. b) Actuator burst pressure as a function of internal channel height, with a constant membrane thickness of 0.25 mm (mean $\pm$ SEM, n = 4 actuators). c) Burst pressure as a function of membrane thickness (mean $\pm$ SEM, n = 4 actuators). d) % pristine actuators as a function of adhesion layer thickness (mean $\pm$ SEM, n = 5 actuators). e) Scanning electron micrographs of actuators with 30μm and 50 μm adhesion layers (cross-section).

nel height, thickness of the inflating membrane, and the thickness of the adhesive layer during the co-bonding process (illustrated in Figure 5.3a). Each of these metrics were compared against two variables: the failure pressure of the actuator and the number of channel defects observed during manufacturing. The primary defect took place during the process of co-bonding the cured portion of an actuator (the concave portion of the internal channel, as well as a thick silicone layer and the nanofiber layer) to a thin cast film of uncured silicone, which forms the upper membrane of the internal channel. The defects were small cylindrical pillar(s) spanning the top and bottom of the channel, which formed after the cured part was placed down onto the film. We hypothesized that these pillars formed as a result of surface tension drawing the uncured liquid toward the center of the channel, forming a Gaussian-shaped mound that eventually contacts the opposite side of the channel.

The height of the internal channel can be tuned by modifying the 3D-printed mold that is used to form the thicker portion of each actuator. Three molds were printed, with channel heights of 0.3 mm, 0.4 mm, and 0.5 mm. These molds were then used to fabricate fiber-reinforced actuators with defined thicknesses of the channel membrane and adhesion layer during co-bonding. The channel membrane thickness was varied from 0.25 mm to 0.35 mm in 0.5 mm increments. Adhesion layer thicknesses of 0.03 mm and 0.05 mm were fabricated for each set of parameters. For each batch of actuators, the total number of actuators with "pillar" defects was recorded. Furthermore, the burst pressure of each actuator under pneumatic actuation was also measured.

Of the tested channel heights, a 0.5 mm channel displayed the highest failure pressure (Figure 5.3b). Thus, we selected this height for all actuators moving forward. Burst pressure also increased with membrane thickness; a 0.35 mm membrane displayed significantly higher burst pressure than the two thinner options (Figure 5.3c). This is a logical result, as imposing a thicker barrier against applied pressure will require a higher pressure to induce a rupture. Finally, we compared the burst pressure of an actuator with a 0.5 mm internal channel and a 0.35 mm membrane using either a

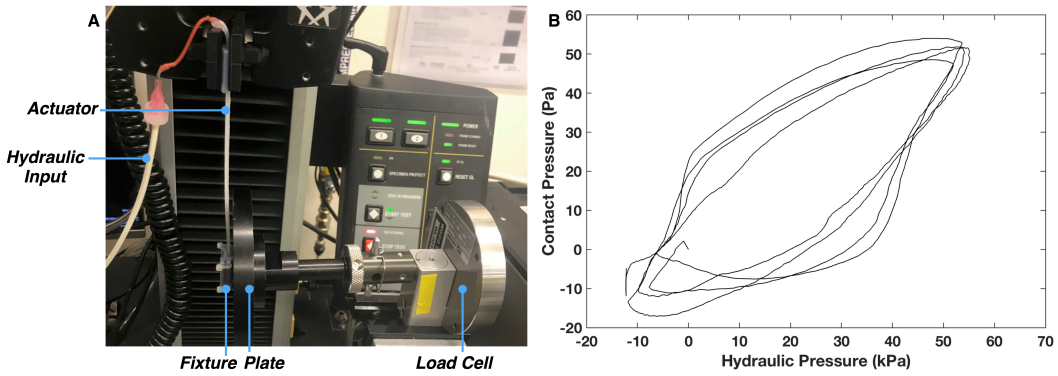


Figure 5.4: a) Contact pressure of the distal end of a nanofiber-reinforced soft actuator is measured during hydraulic inflation. The actuator tip is placed in a 3D printed fixture, which is attached to a plate connected to a 10 N load cell. Contact pressure is calculated using the blocked force recorded by the load cell and the area of the fixture. b) A representative actuator is pressurized and de-pressurized over four cycles. At the typical hydraulic operating pressure for nanofiber-reinforced soft actuators (6 psi, or 41.4 kPa), the average contact pressure was 0.0455 $\pm$ 0.007 kPa (45.5 $\pm$ 6.7 Pa). Error was calculated as mean $\pm$ SEM for n = 3 actuators, and 4 cycles per actuator.

0.03 mm or 0.05 mm adhesive layer during co-bonding. The 0.03 mm adhesive layer yielded a significantly higher burst pressure than the thicker layer, as well as a lower incidence of pillar defects during fabrication (Figure 5.3d). Scanning electron micrographs of actuator cross-sections revealed that the thinner adhesive layer yields a uniform membrane thickness across the width of the channel (Figure 5.3e). In contrast, capillary action resulted in a non-uniform membrane when a 0.05 mm adhesive layer is used. Thus, we selected the following parameters for all subsequent soft actuators: 0.5 mm internal channel height, 0.35 mm channel membrane thickness, and 0.03 mm adhesion layer thickness. We also noted that the failure pressure of pneumatically pressurized nanofiber-reinforced actuators was significantly higher than that of silicone-only actuators (both fabricated with the previously listed parameters, Figure A.9).

5.3.3 Characterizing Contact Pressure Exerted by Individual Actuators

One benefit of utilizing soft robotic actuators for gentle manipulation is that the contact pressure exerted by each appendage is lower than that of traditional rigid (e.g., plastic or metal) end effectors.

To gauge contact pressure of our device, the blocked force exerted by the tip of each actuator (the part likely to make contact with a target object) was measured using a stationary 10 N load cell connected to a plate. To minimize gravity effects, actuators were mounted vertically with the distal tip pointing downward (Figure 5.4a). This end was secured in a 3D printed fixture, which was attached to the plate. Each actuator was then pressurized hydraulically, and the blocked force exerted by the actuator tip on the fixture was recorded using Instron Bluehill 3 testing software (Instron 5544A, Norwood, MA). Finally, the contact pressure exerted by an actuator was calculated using the area of the fixture and the measured force. At their typical operating pressure of 6 psi (41.4 kPa), nanofiber-reinforced soft actuators exerted an average contact pressure of 0.0455 $\pm$ 0.007 kPa (mean $\pm$ SEM), which is well below the target of <1 kPa. A representative plot of one actuator being hydraulically pressurized and de-pressurized over four cycles in shown in Figure 5.4b. These results confirm that our soft actuators exert a low, safe pressure on target objects and organisms.

5.4 Evaluation of Underwater Grasping Performance

The performance of our ultra-soft robotic gripper was empirically evaluated using our underwater testing platform on the basis of two standard grasp quality metrics: the size of the region of acquisition [220], and the robustness to external forces on the object [221,222]. Both metrics can be used to inform end users (remotely operated vehicle pilots) about how to best utilize the capabilities of this gripper when mounted on a teleoperated ROV.

5.4.1 Mapping the Region of Acquisition

The region of acquisition of a grasping device or hand is defined as the set of all positions (relative to a target object) that the hand can be placed in order to reliably grasp the target [220]. For this ultra-gentle hand, we first made a rough map of a planar slice of this three-dimensional region, then per-

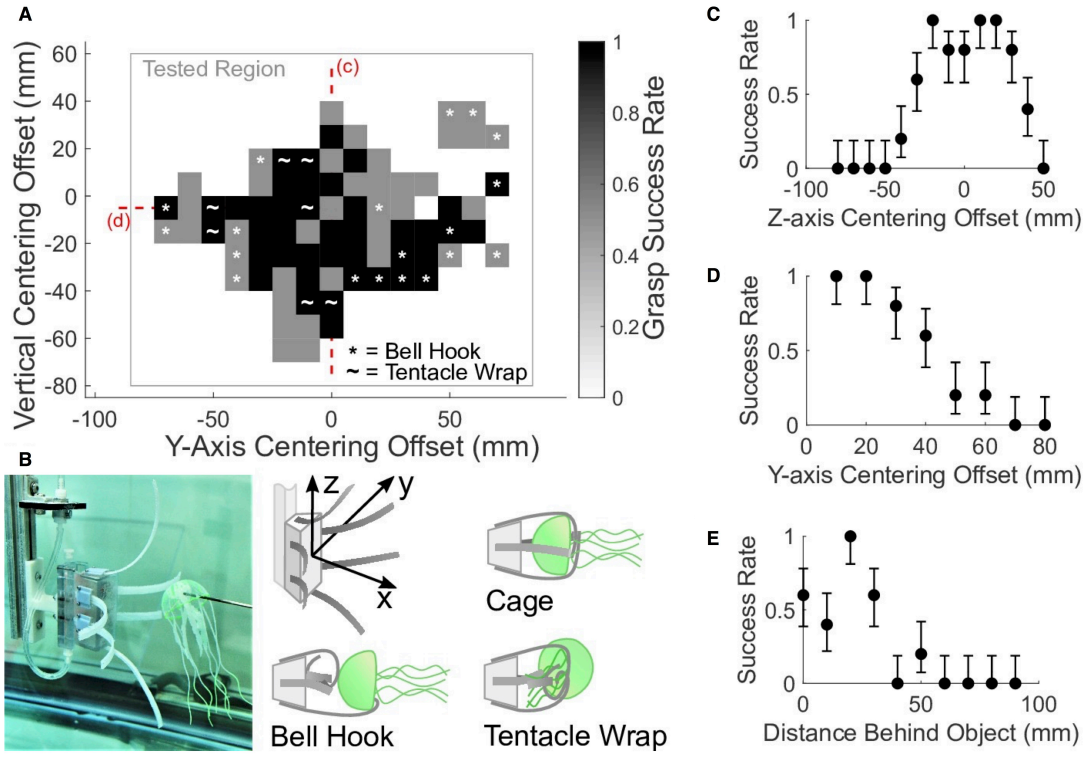


Figure 5.5: We mapped the region of acquisition of our soft gripper using our water tank testing setup. a) A coarse estimate (n = 2) of the region indicates a roughly diamond shape, and b) different grasp types were observed, including cage grasps, bell hooks, and tentacle wraps. A higher-fidelity investigation along c) the vertical axis, d) the y-axis, and e) the x-axis behind the target was performed with n = 5 grasps for each condition. Error bars in C-E represent the 95% Agresti-Coull confidence interval.

formed higher-fidelity testing along key axes. Based on the estimated region of acquisition, we can gain insight into the precision required to reliably grasp objects when the hand is mounted to the arm of a ROV.

A slice of the region of acquisition (located approximately 5 mm behind the target) was estimated empirically by performing a series of grasps on a surrogate target: a silicone model jellyfish. Each grasping operation consisted of an approach, grasp, retract, and release cycle. For each centering position, the palm of the gripper is initially located 350 mm behind the target. The gripper then moves toward the target, and a grasp is attempted by inflating the actuators to 6.0 psi. Finally, the gripper attempts to pull the target to a new position (200 mm behind the initial centering position), and releases it (by depressurizing the actuators) in preparation for the next test. All tests are performed at very low speeds (0.080 m s^{-1}) to ensure minimal fluid drag with the target and fingers. To capture the entire region, a sweep was performed over a grid of centering positions ($n = 2$ grasps per position) 160 mm in width and 120 mm in height, with a step size of 10 mm in both directions (Figure 5.5a).

To quantitatively asses the performance of the gripper at each centering position, the grasp success rate was determined by observing the number of successful grasps. A grasp was considered successful if the target was moved to its final position and remained there until it was released. If the target was released early or was not grasped, the attempt was considered a failure. The grasp success rate at a given hand position is then calculated as the number of successful grasps normalized by the total number of attempts. Based on the shape of the high-density, low repetition mapping of the region of acquisition, we also performed higher-repetition sweep ($n = 5$) along key axes associated with the three-dimensional volume of the region. The axes tested include the vertical axis (z) through the center of the region, one side of the horizontal axis (y) through the center, and the axis directly behind the center of the object (x) The resulting grasp success rates are shown in Figure 5.5c-e.

The region of acquisition measured for our gripper not only provides insight into the precision

needed to reliably grasp objects, but also into the mechanisms by which the gripper can passively adapt to achieve reliable grasps. The general shape of the region is a diamond (roughly symmetric about the vertical axis), as shown in Figure 5.5a. This shape is logical considering the placement of actuators around the rectangular palm. Also unsurprisingly, the center of the main region is located 15 mm below the center of the object, which can be explained by slight buoyancy of the soft actuators due to trapped air. A conservative metric for the characteristic dimension of the region of acquisition can be found by the radius of the largest circle that can be completely contained within the boundaries of the main region. For our gripper, this radius is approximately 42 mm, indicating that a centering offset within 42 mm of the target in any direction will result in at least a 50% chance of a successful grasp. In addition, the gripper has even better performance when translated directly along the y or z axes (radii of 50 mm and 65 mm, respectively). Moreover, the gripper was able to grasp objects up to 50 mm behind the target (x-axis), albeit with high variability in grasp success (Figure 5.5e). Finally, we observed that grasps toward the center of the region consistently demonstrated strong caging grasps, whereas locations along the edge of the region displayed a wider variety of grasps (hooking under the bell or wrapping around tentacles). Taken collectively, this information can be used to instruct operators on positioning requirements to most effectively use this gripper.

5.4.2 Measuring the Robustness to External Forces

The robustness to external forces and torques on an object during a grasp is typically defined as the maximum force the gripper can resist (or conversely, the minimum force required to pull an object out of the grasp) minimized over all force-application angles[221]. This measure of robustness can be used to understand how to maneuver an ROV arm to transport delicate samples to a storage container.

To quantify the maximum external force as a function of the applied angle, we executed grasps on the same synthetic jellyfish target. With zero centering offset, the hand was retracted, then paused

while force was applied on the object through the Kevlar tether at a known angle. Force was applied by adding constant increments of mass to a plastic container at the end of the tether (connected via low-friction pulley system to the target object) until the target slipped out of the gripper. The process was repeated five times for angles ranging from 0° (perpendicular to the palm) to 90° (parallel to the palm) in increments of 15° (Figure 5.6a). We assumed that the relationship is symmetric about the z-axis based on the symmetry of actuator placement.

Our results indicate that the gripper's ability to withstand external forces improves as the force application angle increases from 0° - 60°, while the grasp success rate decreases as a function of the angle (Figure 5.6b). We see that the worst-case scenario for our gripper involves pulling the target object straight back at an angle of 0° with an average maximum pull force of 0.20 $\pm$ 0.02 N. As the angle increases, the mean and error increase up until 60°, where the maximum pull force increases to 0.77 $\pm$ 0.18 N. In addition, the initial grasp success rate was 100% for angles 30° and below, but decreased as a function of the angle until 75°, where grasping was no longer possible. However, even the worst-case pull force (at 0°) is much greater than the theoretical thrust force (0.002-0.004 N, derived in the Appendix) generated by *A. aurita* within the target size range (7-10 cm bell diameter).

To understand the trend in the maximum force as a function of applied angle, one possible insight can be drawn from treating the ultra-soft actuators as tensile members with interactions between fingers treated as "weak points", as discussed in Section A.5.4. Based on this simplification, we find that tensile forces are not shared equally between all fingers, and shear forces between two fingers have a critical breaking point. This critical shear force causes the fingers to release the object at a certain applied force, which increases as a function of the applied angle, as shown in Figure A.14.

5.4.3 Evaluating Grasp Quality as a Function of Gripper Motion

During a typical deep-sea biological sampling operation, the act of moving the target animal after grasping it produces forces on the animal due to fluid drag. To understand how this effect manifests

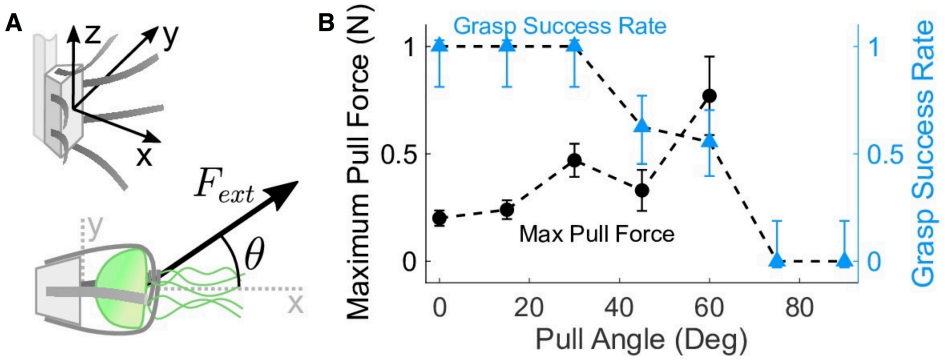


Figure 5.6: The robustness of our gripper to external forces on the object was evaluated by a) grasping the target and pulling it out at an angle. b) The maximum external force before failure increases as a function of the angle applied, while the grasp success rate decreases (n = 5 grasps per condition). Error bars represent the standard error of the mean for pull force measurements, and the 95% Agresti-Coull confidence interval for grasp success rate estimates.

itself during a grasping operation, we performed grasps on the same artificial jellyfish with the gripper positioned on-center, but with varying retraction speeds from 0.0080 m s^{-1} to 0.200 m s^{-1}. At lower speeds, the object remained at roughly the same position (with respect to the gripper) for the entire duration of the retraction motion. However, as speed increased, an increase in extraneous motion during retraction was observed. Thus, the speed at which the target is pulled could potentially have a significant impact on the stability of the grasp.

To further understand the maximum speed needed for an object to be pulled from the gripper due to fluid drag alone, we calculated the drag in water on our target jellyfish (approximated as a hemisphere), as discussed in Section A.5.3 (Figure A.13). Based on the average grip force measured at a 0° pull angle (0.2 N), we found that a velocity above 1.3 m s^{-1} would be required to dislodge a jellyfish from the soft gripper. Since all of our testing was performed using a 0.080 m s^{-1} retraction speed (roughly 1/9th the maximum speed), we assume all of our results represent quasi-static grasping. In addition, these estimates can help inform operators on how fast they can maneuver ROV arms while attempting to sample these delicate animals.

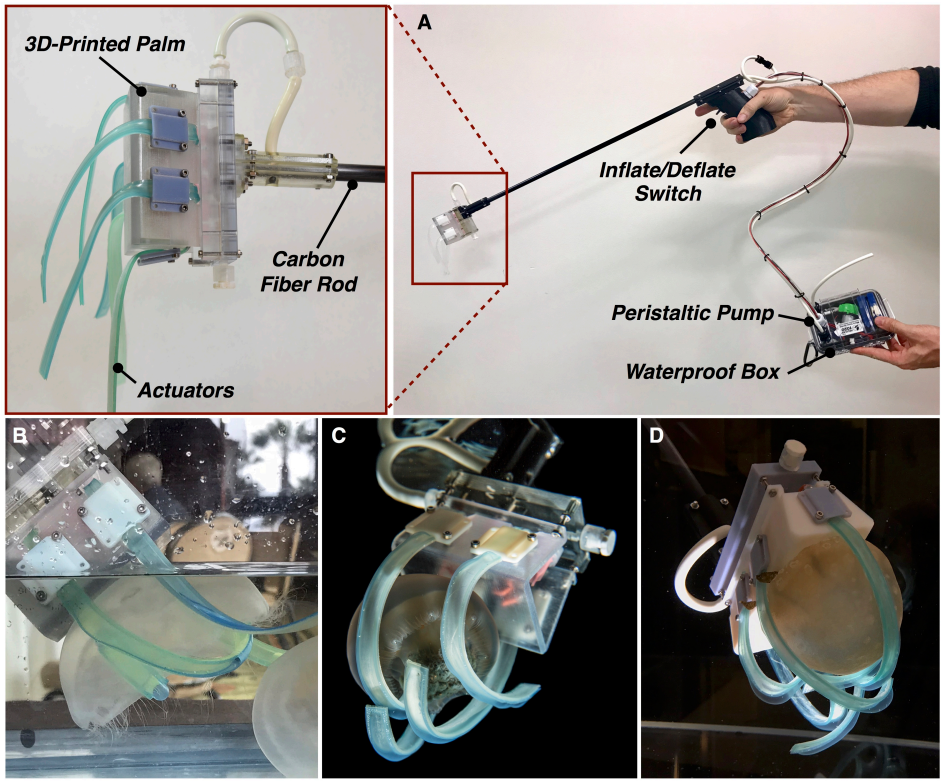


Figure 5.7: a) Design of soft robotic gripping device, shown with a four-actuator hub. *Inset:* Different hubs, including this six-actuator palm, can be attached modularly. Soft fiber-reinforced actuators grasping b) *Aurelia aurita*, c) *Catostylus mosaicus*, and d) *Mastigias papua*. c-d) Photos courtesy of Anand Varma.

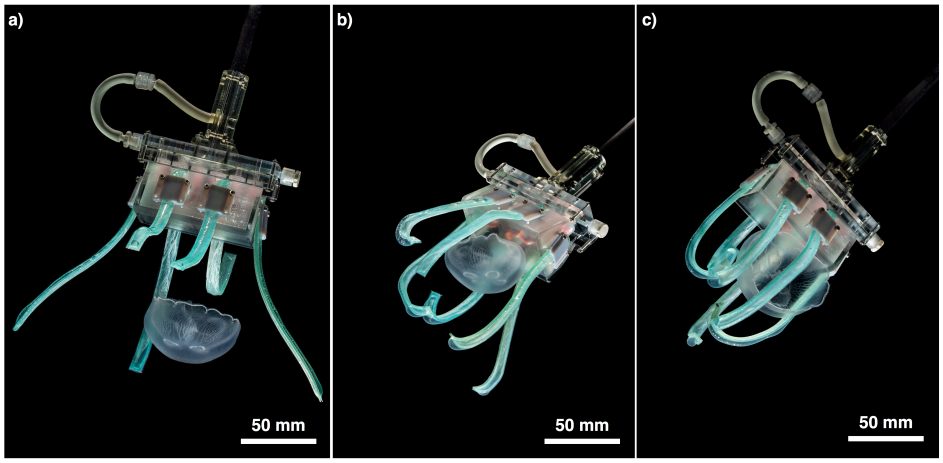


Figure 5.8: Gentle grasping of *Aurelia aurita*. a) Actuators approach the jellyfish, uninflated. b) Actuators begin to hydraulically pressurize. c) Actuator pressurization continues until the jellyfish is gently and securely grasped. Photos courtesy of Anand Varma.

5.5 Preliminary Field Testing of Soft Robotic Gripper

5.5.1 Design of Portable Grasping Device

Although these soft actuators are compatible with the manifold system of existing remotely operated vehicles, we aimed to test the viability of our robotic gripper outside a laboratory setting. To achieve this goal, we developed a portable, waterproof, hand-held device to operate the soft gripper (Figure 5.7a). This device uses a 12V peristaltic pump (PM200F, Simply Pumps, PA) to open and close the actuators. The actuators and hub are fastened to one end of a carbon fiber rod, while the pump and batteries are housed in a waterproof box at the opposite side. An input tube connected to the pump draws water from the device's environment, and facilitates rapid hydraulic actuation (actuators inflate in $\sim$ 5 seconds) in a marine, laboratory, or aquarium setting.

5.5.2 Gentle Handling of Jellyfish using Soft Gripper

Having characterized the performance of the soft nanofiber-reinforced actuators in controlled tank tests, we sought to demonstrate gentle grasping using live jellyfish. Adult *Aurelia aurita* (Figure 5.7b), *Catostylus mosaicus* (Figure 5.7c), and *Mastigias papua* (Figure 5.7D) housed at the New England Aquarium (Boston, MA) served as the target organisms (Animal Care and Use Committee protocol # 2018-09). For *A. aurita* and *C. mosaicus*, a single jellyfish was placed in a transparent tank and the hand-held robotic actuation device was used to carefully grasp and release the animal. The soft actuators were inserted into the tank (Figure 5.8a), pressurized to roughly 5 psi as the actuators enclosed the jellyfish (Figure 5.8b-c), and then de-pressurized to allow the animal to swim away. This procedure was repeated several times (roughly $n = 20$ grasps) using multiple jellyfish ($n = 2$-4 per species). We demonstrated that once a jellyfish was enclosed securely by the actuators, it was unable to break the grasp. An aquarist was present to periodically monitor the jellyfishes' behavior during the trials. In all cases, the jellyfish displayed no adverse effects or changes in behavior following the grasp.

Rectangular actuator hubs containing both four and six appendages were tested for their efficacy in grasping and restraining the jellyfish. The four-actuator palm measured 60 mm (length) by 50 mm (width), with two digits on each side of the longer edges. The six-actuator hub measured 78 mm by 45 mm, and featured an additional actuator on the top and bottom edges. While both setups were capable of grasping the gelatinous animals, the six-actuator device displayed a more secure grip. In several trials using the four-actuator palm, the appendages began inflating around a jellyfish, but the animal swam toward the top or bottom edges and evaded capture. The addition of an extra actuator at both ends improved grasp quality by gently restraining the jellyfish within the network of inflated actuators. During this pilot field study, each set of actuators were pressurized and de-pressurized approximately one hundred times before a failure was observed. The failure was

a rupture in the membrane enclosing the inflating channel of an individual actuator. During the lifetime of an actuator, the elastic membrane can become distended due to rapid pressurization or applying an input pressure above 8 psi. Eventually, a ∼1 cm tear may occur in the distorted membrane, at which time the actuator will be inoperable. The modular design of the soft gripper hub enabled the faulty part to be removed, and a new actuator to be inserted in its place.

5.6 Summary

In this chapter, we have demonstrated a novel approach to design, manufacture, and test nanofiber-reinforced soft robotic actuators for ultra-gentle manipulation of delicate marine organisms. Specifically, we discussed the geometric optimization of individual actuators to increase durability and batch throughput, and the design of a modular hub to unite a set of actuators into a gripping device. Moreover, we described two important grasp quality metrics: the region of acquisition of the gripper in a rectangular configuration and the robustness of its grasp to applied force. Next, we incorporated the device into a portable, hand-held tool that can be used to interact with biological specimens in a laboratory or in shallow marine environments. Finally, we have demonstrated the use of this portable soft gripper to successfully perform gentle grasping of three canonical jellyfish species (*Aurelia aurita, Catostylus mosaicus,* and *Mastigias papua*).

These results represent an unprecedented capability for delicate manipulation of fragile tissue samples. While other fiber-reinforced soft actuators have been developed to grasp delicate marine species (e.g., corals, sea cucumbers), none of these devices are able to apply sufficiently low contact pressure needed to safely interact with gelatinous soft-bodied animals. Our soft robotic actuators offer the opportunity for nondestructive interaction with and investigation of extremely delicate marine organisms whose study had previously been limited by existing collection paradigms. In the future, we envision the addition of sensors into these ultra-gentle actuators to monitor physiological

and genomic parameters *in situ*, and to better understand and conserve deep-sea biodiversity. They may also be utilized in tandem with other robotic devices, such as rotary-actuated folding polyhedra, in an effort to better investigate and characterize deep-sea lifeforms without bringing them to the surface. The scalability of our technology may be leveraged towards a variety of medical and industrial applications that require extreme care or low forces, such as tissue manipulation with endoscopic end-effectors, assembly line handling of fragile components, and delicate crop harvesting.

6

Conclusion

6.1 Summary

This thesis explores the development of novel polymer nanofabrics, and demonstrates their utility as a reinforcing material for ultra-gentle soft robotic actuators. To recap, the major contributions of this work are as follows:

1. We have established novel methods for manufacturing nanofabrics, and controlled their com-

position, morphology, orientation, and mechanical properties. Highly aligned nanotextiles can be produced using pull spinning; our experiments have demonstrated the flexibility and utility of this method for tissue engineering scaffolds and point-of-use apparel. In addition, we have fabricated and characterized multi-material nanofabrics composed of i) two discrete polymer fibers, and ii) functional polymers requiring solvents immiscible with those commonly used to produce nanofibers.

2. We present the design of a nanofiber-reinforced soft actuator that is robust and reproducible. Using soft lithography, rotary jet spinning, and molding processes, we can manufacture compliant composite actuators at the mili- and meso-scale. These actuators can be operated individually, or combined to form a gentle gripping device.

3. We have developed analytical models of composite actuator motion as a function of input pressure, nanofiber orientation, fiber and elastomer stiffness, and laminate structure. These frameworks have been used to guide design and development of fiber-reinforced actuators, and to predict the curvature and bending mode(s) achievable by an actuator.

4. We have demonstrated nondestructive grasping of ultra-low modulus (<1 kPa) objects. Our results indicate that soft fiber-reinforced actuators apply a low, safe contact pressure on the order of the stiffness of target organisms. Moreover, we have identified the region of attainment and resistance to applied forces for a soft gripping hand composed of six actuators. Finally, we have demonstrated the capability and efficacy of this device in a preliminary field trial involving three jellyfish species.

While these topics represent an exciting fusion of nanotechnology and soft robotics, many avenues remain to explore. The following sections provide a brief discussion of future directions in nanofiber manufacturing, soft robotic actuators, and marine sampling.

6.2 Point-of-Use Textiles

In Section 1.8, we demonstrated that the pull spinning system can be adapted to point- of-wear apparel, in which a garment or textile is manufactured directly onto the user's skin. We presented a simple, proof-of-concept study to show how nanofibrous textiles can be spun directly onto the knee joint of a doll without delamination as the joint was flexed and relaxed over multiple cycles. However, the potential of point-of-use textiles extends far beyond this preliminary study. Future applications for directed production of customized nanotextiles could extend to spray-on sportswear that gradually heats or cools an athlete's body, sterile bandages deposited directly onto a wound, and fabrics with locally varying mechanical properties.

While these potential directions hold promise for athletes, soldiers, and medical personnel, nanofiber manufacturing technology must be improved before it can be translated to these domains. The most critical challenge toward this goal is solvent selection. The vast majority of contemporary nanofiber fabrication systems utilize either volatile organic acids (which rapidly evaporate to expose a polymer solute) or dipolar organic solvents, such as dimethylformamide or N-Methyl-2-pyrrolidone. The latter class of compounds are particularly useful for dissolving conductive polymers, namely polypyrrole and poly(vinylidene fluoride), which are difficult to fabricate in high volume (as nanofibers), yet are of interest for polymer-based sensors. Nevertheless, both groups of solvents carry a variety of health and safety risks, which strictly limit their use to laboratory fume hoods and ventilated gloveboxes. In order to manufacture point-of-use fabrics, it will be necessary to adapt the fiber fabrication mechanisms to support less volatile solvents, explore novel avenues for organic solutes from which to spin fibers (e.g., cellulose or other plant-based materials), and/or scale alternate approaches (e.g., melt spinning) which do not require the use of solvents.

6.3 Sensing via Multi-Material Nanotextiles

Multi-modal nanofiber manufacturing holds great potential to fabricate multi-material nanotextile scaffolds, flexible sensors, and lightweight devices by combining electronic, elastic, or drug-eluting materials. In Chapter 2, we discussed the state of multi-material nanofiber fabriation, and presented a novel strategy for manufacturing such constructs. Specifically, we demonstrated the use of orthogonal solvents to produce a nanotextile containing discrete polyurethane (providing structural support and elasticity) and poly(vinylidene fluoride) (piezoelectric component) fibers. While this preliminary study focused on the challenges of manufacturing hybrid textiles with immiscible solvents, the next steps in the development of multi-modal nanofiber sensors must incorporate additional process control. For example, imposing pre-strain on the nanofabric during manufacturing may help to orient the polymer backbone into the preferred crystalline β phase and to increase the piezoelectricity of the device. Furthermore, imposing additional environmental controls within the fiber production chamber (e.g., humidity and temperature control) or doping the poly(vinylidene fluoride) solution with hydrated salts [223] may be useful in modulating solvent evaporation, polymer chain orientation and dipole orientation. These qualities may also impact the end-stage functionality of the hybrid textile. To optimize both the performance of functional materials and the formation of the supporting elastic fibers (e.g., polyurethane), the effect of external process controls must be examined for both precursor solutions.

6.4 Expanding the Topography of Fiber-Reinforced Actuators

In Chapters 3 and 4, we present analytical models that predict the curvature and bending mode of a cantilever soft actuator based on the materials and geometry of the device. We have shown that by varying fiber orientation, we can achieve complex coupled motions, such as bending-twisting. The next step in this development is to apply these custom motions toward specific tasks. For example,

while many of the grip strategies executed by our soft gripper are related to a caging grasp, we can imagine a grasper that relies on an entanglement grip to cushion target objects. Rather than wrapping actuators around the object, an entanglement gripper would use points of contact between a group of adjacent digits to gently immobilize a target. One approach toward achieving this grasp style is to utilize a variety of bending modes. Actuators that twist, contract into helices, and/or pleat into waves would be particularly suited to this task.

The preceding chapters have discussed the effect of nanofiber orientation on soft actuators that take the form of high aspect ratio cantilevers. This geometry is useful for our stated goal of gentle grasping for fragile tissue specimens, and has the additional advantage of modularity; appendages that have failed can easily be exchanged for new actuators. However, a cantilever construction represents just one simple shape that a fiber-reinforced soft robot can take. Another approach could be the design of a planar fiber-reinforced sheet; upon pressurization, the shape of the sheet would be transformed from a two- to a three-dimensional structure by regulating fiber orientation and air channel position. Using finite element models, fiber patterns could be prescribed to fit specific folding or shape criteria. To construct such patterns, fiber sheets could be incised via laser-cutting, as demonstrated in previous studies[180]. This construction would be a promising strategy to gently capture small marine organisms ($\sim$ <3 cm) which may be challenging to grasp using existing robotic grippers, nets, or vacuum systems.

6.5 The Future of Soft Robotic Gripping: Modular and Multi-Functional

This thesis focuses on the design, fabrication, and testing of soft robotic actuators for delicate manipulation. However, future robotic systems will incorporate additional functionality besides gentle grasping. By developing a series of actuators with various specific capabilities, a robotic gripper with specialized "fingers" can achieve multiple experimental objectives simultaneously. A multi-

functional gripper is of particular interest for use for domains (e.g., the deep sea) in which accessing the robot during an experiment to augment its function with additional components is either inconvenient or impossible. Potential functions that can be useful for next-generation soft grippers include: contact sensing, biological assays, and aqueous sampling.

The integration of compliant sensors with soft robotics is a promising avenue for developing more responsive actuators. Real-time reporting of contact pressure exerted by actuators on a biological target will improve grasp quality by providing ROV operators with greater tactile feedback. Moreover, pressure data may help to distinguish between marine species which visually resemble each other, but have significantly different stiffnesses. Two novel approaches for flexible and durable sensing utilize lossy optical waveguides [224] and a conductive potassium iodide and glycerol solution [225] to provide contact force data. Both strategies are promising for integration with deep-sea soft robotic grippers due to their biocompatible materials, operability in water, and compliant structure.

Another potential feature for future soft actuators is on-board biological assays. Among the animals encountered by an ROV in the deep-sea, there are many species about which little is known. Moreover, several of the organisms (e.g., certain corals) are extremely old, having survived in their environment for thousands of years. Damaging or destroying such rare and fragile specimens in the gripping process must be avoided at all costs. Instead, we can potentially use soft robotic actuators to gather biological data about these animals without grasping or applying force to them. For example, soft appendages could carefully brush or touch the surface of a delicate sample, releasing debris containing genetic information into the surrounding water. A small volume water sample may be taken using a device embedded into the palm, stored using reagents housed on-board, and analyzed when the ROV returns to the surface. Another option may be to embed sensors directly into the palm; in this case, data will be collected during a grasp and the animal will be subsequently released. Ideally, the devices used in this case would gather non-contact data, such as pulse oximetry readings. These operations could exist concurrently with pressure or curvature sensors within the actuators

themselves to provide a holistic profile of a grasp.

A third prospective feature for soft hydraulic actuators relates to water sampling, rather than specimen collection or manipulation. Our manifold design for deep-sea robotic actuation draws seawater from the area surrounding the ROV to inflate the robotic fingers. It is possible to use this feature to collect and preserve water or genetic samples instead. For example, the internal cavity of an actuator could contain dehydrated reagents or preservatives. When the actuator is inflated and water enters the channel, it would react with these materials *in-situ* to stabilize fragmented tissue or DNA samples in the water. Rather than deflating and releasing this water, a carousel hub design could seal the actuator and shift a new, empty digit into position for the subsequent sample.

6.6 Interactive Soft Robotics in Entertainment

Another potential application for the future generation of soft robots is interactive entertainment. With the rise of augmented and virtual reality, consumers are becoming accustomed to entertainment paradigms in which they can actively participate. Tactile sensation is a significant component of these experiences, but one which has not yet been comprehensively explored using compliant robots. One of the primary advantages of soft robots is their safety, particularly when compared with the rapid motions and heavy materials of conventional metallic robots. Their smooth movements and pliable materials make soft systems favorable candidates for interaction with human users. These qualities may be leveraged for entertainment by incorporating haptic sensations and contact sensors into the matrix of a soft robot, enabling a user to communicate with or control the robot intuitively using touch. For example, the pressure applied to a soft bladder in the body of an interactive robot could be monitored as the character receives a hug from a user. This measurement would enable the robot to respond appropriately, returning the action. To ensure that the devices can be used, maintained, and cleaned for as long as possible, engineers must select matrix materials

that are both durable and compliant. Other potential applications of soft robots in the entertainment space include: soft animatronic figures that use hydraulic or pneumatic pressurization to execute smooth motions, wearable compliant systems that extend a user's capabilities in the context of a game (e.g., antennae, wings, or a tail), or soft-bodied characters that move around a theme park and interact with guests.

6.7 Conclusion

Taken as a whole, this thesis demonstrates novel manufacturing strategies for polymer nanofabrics, the integration of nanofibers into soft robotic actuators, and the use of fiber-reinforced actuators to perform delicate manipulation tasks in an aqueous environment. Lessons learned from developing a actuator that is both robust enough to withstand marine operation and compliant enough to successfully capture fragile animals have widespread implications across a variety of applications, including manipulating tissue and surgical tools, sensing and mapping confined domains, grasping fragile objects, and industrial crop harvesting. With this potential in mind, the future of robotics appears bright – and soft.

A

Appendix A

A.1 Nanofiber Scaffolds for Tissue Engineering

In Chapter 1, we discussed a case study in which nanofiber scaffolds were used as the basis for an *in vitro* contractility assay to regulate muscle formation and to support function of smooth and skeletal muscle. The following sections detail the protocols used to culture muscle cells on the fiber scaffolds (fiber muscular thin films, or fMTFs), perform contractility assays, and quantify the contraction of

muscle tissue on the films.

A.1.1 Fiber Muscular Thin Film Cell Seeding and Culture

Mouse myoblast cell lines (C2C12) (CRL-1772, ATCC, Manassas, VA) were seeded at 50,000/cm^2 and cultured in a growth medium of Dulbecco's Modified Eagle's Medium (DMEM, 11995-065, GIBCO, Carlsbad, CA) supplemented with 15% fetal bovine serum (Invitrogen, Carlsbed, CA) until confluence. The C2C12s were then cultured for four days in an initial differentiation medium consisting of DMEM/F-12 culture medium (12-719F, Lonza, Walkersville, MD) supplemented with 1% horse serum (Gibco, Carlsbad, CA). Next, they were cultured for six days in a second differentiation medium consisting of DMEM/F-12 supplemented with 5% horse serum. Only passage numbers from 4 to 15 were used. For the human vascular smooth muscle studies, primary human pulmonary artery vascular smooth muscle cells (Lonza, Walkersville, MD) were cultured for two days in M199 culture medium (GIBCO, Carlsbad, CA) supplemented with 10% heat inactivated fetal bovine serum, 10 x 10^{-3} m HEPES (4-(2-hydroxyethyl)-1-piperazineethanesulfonic acid), 0.1 x 10^{-3} m minimal essential medium (MEM) nonessential amino acids, 20 x 10^{-3} m glucose, 1.5 x 10^{-6} m vitamin B-12, 50 U mL^1 penicillin, and 50 U mL^1 streptomycin (GIBCO, Carlsbad, CA). After two days, the medium was switched to a serum-free version of the growth media in order to induce a contractile phenotype for 24 hours prior to experimentation.

A.1.2 Contractility Assay and Analysis

The contractility assays were performed at desired time points on a stereomicroscope (Model MZ6, Leica Microsystems Inc., Wetzlar, Germany) outside the incubator connected to a National Instruments LabVIEW data acquisition board. A heating platform was set up on the microscope to replicate culture temperature (37°C) and electrical stimulation was performed using electrodes immersed

in the well, connected to an external field stimulator (Myopacer, IonOptix Corp., Milton, MA). During the contractility experiments, the samples were put in a custom Tyrode's solution developed in the lab (1.198 g L^{-1} HEPES, 0.040 g L^{-1} NaH_2PO_4, 0.901 g L^{-1} glucose, 0.265 g L^{-1} $CaCl_2$, 0.203 g L^{-1} $MgCl_2$, 0.403 g L^{-1} KCl, 7.889 g L^{-1} NaCl, pH 7.4, all chemicals from Sigma-Aldrich, St. Louis, MO). The stimulation was set at high voltage (40V) to obtain strongest force-frequency curve. For the human vascular smooth muscle, the vasoconstrictors acetylcholine and endothelin (Sigma-Aldrich, St. Louis, MO) were utilized to induce contraction, while the vasodilator HA1077 (Sigma-Aldrich, St. Louis, MO) was used to induce relaxation. Drugs were dosed serially after 10, 20, and 30 minutes, respectively. To capture the slow contraction of the smooth muscle, images were taken once every 30 seconds.

A.1.3 Fiber Muscular Thin Film Stress Quantification

The horizontal projections of the cantilevers were tracked using a custom ImageJ (NIH, Bethesda, MD) software and the radius of curvature was determined using a custom MATLAB software (Mathworks, Natick, MA). The existing muscular thin film model assumes a cell layer at the surface of the film and calculates the stress derived from the radius of curvature using a modified version of Stoney's equation[134,129]. The fMTF model was modified to account for cellular infiltration based on immunostained cryosections.

A.2 Structural Properties of Polymer Nanofibers

Centrifugal nanofiber manufacturing systems, such as pull spinning and rotary jet spinning, generate fibers by drawing and thinning a viscous jet. At this stage, the volatile solvent comprising the jet rapidly evaporates, yielding a polymer or protein nanofiber. This process can be used to generate fibers from a variety of polymers, including polycaprolactone, polyurethane, and nylon-6 (Figure

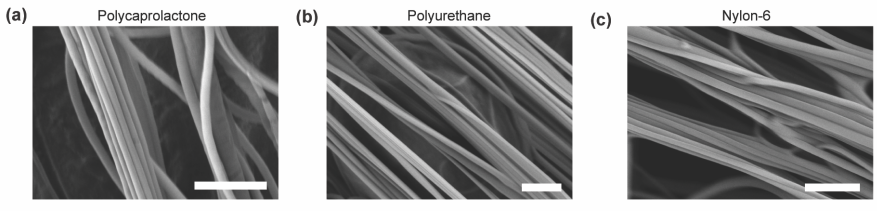


Figure A.1: Scanning electron micrographs of pull spun a) 6 wt/v% polycaprolactone b) 6 wt/v% polyurethane, and c) 6 wt/v% nylon-6 nanofibers. Scale bars, 500 nm.

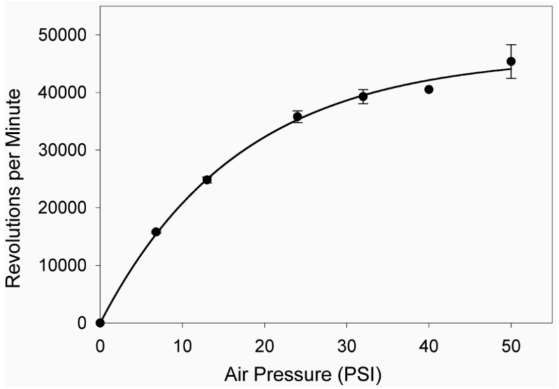


Figure A.2: Calibration curve of the pneumatic motor used to drive the pull spinning process. N = 3 production runs. Error is reported as SEM.

A.1). The composition and, therefore, bond structure of each nanoscale filament impacts the mechanical and chemical properties of the bulk nanotextile. In the following sections, we will discuss the structural properties of pull spun nylon-6 and polyurethane (PU) nanofibers.

A.2.1 Calibration of the Pull Spinning Apparatus

As shown in Figure A.2, the pull spinning device was calibrated by relating known air pressure to the number of revolutions of the bristle per minute. All experiments were conducted at a constant air pressure to minimize sample variation due to bristle revolution rate.

A.2.2 Pull Spun Nanofiber Morphology

We measured polymer nanofiber radii while varying several parameters, namely: motor rotation speed and distance from the bristle to the collector. Moreover, the degree of anisotropy (using orientation order parameter, OOP) was measured for several concentrations of polymer in the precursor solution. Results indicated that there were no significant variations in fiber radii under the first two conditions, suggesting minimal dependence of fiber radius on collector distance and rotational speed within the specified ranges (Figure A.3a-b). These experiments were also conducted using a 6 wt%/vol% polycaprolactone solution in HFIP, and similar trends were observed (1.2b-c). Furthermore, the OOP of polycaprolactone nanotextile sheets was approximately constant between 6-10 wt/v%, indicating that anisotropy is invariant to concentration within these bounds (Figure A.3c).

To determine whether fabrication time impacts the morphology of pull spun nanofiber sheets, we calculated the average fiber radius and % beading of a nonwoven fiber sheet while varying the length of each manufacturing session. No significant changes were detected in average fiber radius or % beading in 6 wt%/vol% polycaprolactone samples collected after 1, 5, or 10 min of continuous fabrication (Figure A.4).

A.2.3 Spectroscopic Analysis of Polymer Vibration Modes

Table A.1 includes several characteristic vibration modes of nylon-6 and polyurethane. These reference peaks were used to evaluate the role of hydrogen bonding in pull spun nylon, polyurethane, and polyurethane:nylon nanofiber samples. The amide I band of nylon 6 is associated with axial N-H and C=O bond deformation and has been reported at 1637 cm-1. Previous studies have postulated that an increase in the amide I band wavenumber indicates interactions between amide groups and carbonyl bonds within nylon 6 and polyurethane chains, respectively.[1-5] This bonding signifies a decrease in intra-chain nylon 6 interactions as interactions between amide bonds and

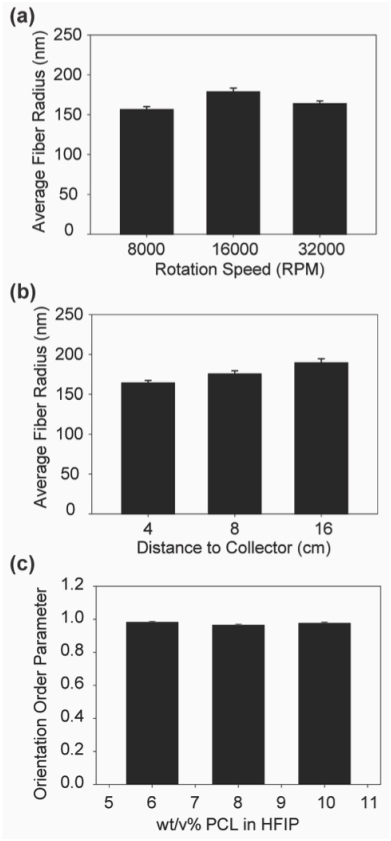


Figure A.3: a) Radius of 10 wt/v% nylon fibers measured as a function of the distance to the collector (cm), at a constant Ω of 45,000 RPM. b) Radius of 10 wt/v% nylon fibers measured as a function of the motor rotation speed (RPM), at fixed Rc of 10 cm. N = 3 production runs, 3 FOVs/run, 100 fibers per FOV. c) Orientation order parameter of free-standing nanofibers: 6 wt/v%, 8 wt/v%, and 10 wt/v% polycaprolactone (PCL) in HFIP. All error is reported as SEM.

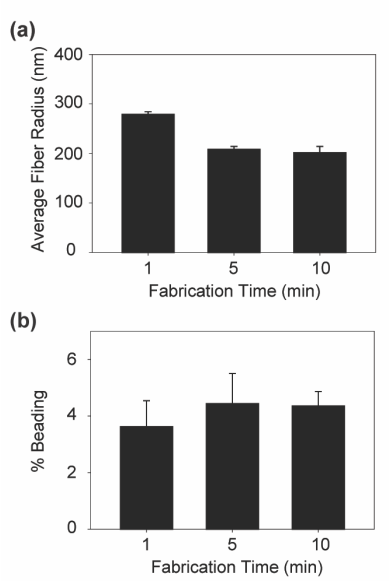


Figure A.4: a) Radius of 6 wt/v% polycaprolactone (PCL) fibers measured as a function of fabrication time. b) Percent beading of 6 wt/v% PCL fibers as a function of total fabrication time. For each time point, n = 3 production runs, 3 FOVs/run, 45 fibers per FOV.

urethane linkages increase. The amide I peak for the nylon/polyurethane hybrid in our empirical data is shifted from 1637 cm-1 to 1641 cm-1. [1-5] The peak intensity of the hybrid nanofibers also decreases from 0.34 to 0.24 absorbance units, confirming a decrease in interchain bonding within nylon 6 chains. Unlike the amide I band, the amide II peak is sensitive predominantly to N-H bonding. Our data reveals an amide II peak frequency shift from 1547 cm-1 to 1539 cm-1; previous studies suggest that this frequency upshift is a result of asymmetric changes in bond length and electron distribution during the formation of hydrogen bonds. The carbonyl bond stretching peak transition from 1729 cm-1 in pure polyurethane nanofibers to 1733 cm-1 in the hybrid sample is analogous to that of the amide I bond. The frequency downshift signals a decrease in intrachain polyurethane linkages and a consequent increase in polyurethane-nylon interactions. A similar trend is observed between 3500-3100 cm-1 for peaks denoting axial N-H bond stretching in nylon and polyurethane. [1-5] Deformation of amide bonds during hydrogen bond formation produces multiple hydrogen

Table A.1: Selected characteristic vibration modes of nylon 6 and polyurethane

Spectral Position [cm^{-1}]	Assignment
680	N-H out-of-plane bend (Amide V)
1539-1547	Secondary amine, N-H bend, C-N stretch (Amide II)
1637-1641	N-H stretch, C=O stretch (Amide I)
1729-1733	C=O stretch
2944-2966	C-H stretch
3100-3335	Secondary amine, N-H stretch (Amide II) [lex]

bond geometries, yielding a range of O-H vibration frequencies that comprise a broad band. The frequency peak shifts observed for the three polymer compositions indicate that blending PU and nylon increases hydrogen bonding within the resulting nanofiber constructs. Strengthening inter- and intrachain interactions result in stronger tensile strength for the anisotropic 5wt/v% PU: nylon composite blend. Comparing vibration modes of the pull-spun nanofibers to those of drop cast films with similar polymer concentrations reveals significant increases in hydrogen bonding after pull spinning. The presence of these interactions further indicates the role of this method in facilitating intrachain bonding.

A.2.4 Determination of Constant for Scaling Law

In Chapter 1, we described a scaling law for the radius (r) of pull spun nanofibers as a function of the kinematic viscosity (ν) of a precursor solution. The viscosity of the polymer or protein solution reduces the rate or fiber thinning as the solution transitions from a droplet to a jet; this effect intensifies as polymer concentration increases (Figure A.5). The scaling relation, $r = C\nu^{1/2}$, was initially outlined in Mellado et al. ([100]) with respect to rotary jet spinning, another centrifugal force-based nanofiber manufacturing system. In this expression, C is a dimensional constant with units of (m^2 s^1). To adapt this scaling law to pull spinning, we fit the constant C from the empirical relation between fiber radius and solution kinematic viscosity (Figure A.5). Thus, the relation demonstrates

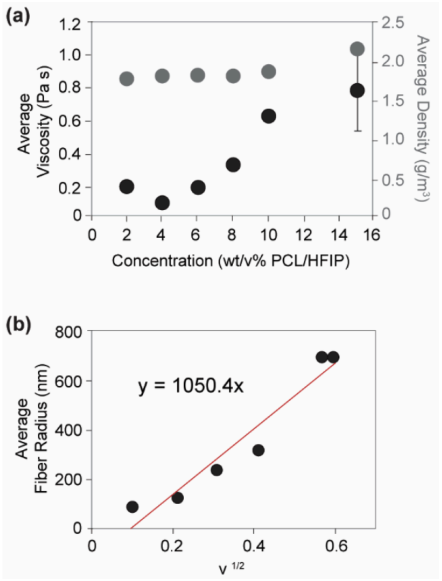


Figure A.5: Characterization of pull spun polymer solutions and nanofibers. a) Density (grey) and viscosity (black) of polycaprolactone (PCL) solutions in 1,1,1,3,3,3,-hexafluoro-2-propanol (HFIP) as a function of polymer concentration (N = 3, Error reported as standard deviation). b) Empirical determination of the scaling constant C from the relation between fiber radius (r) and solution viscosity (ν).

that higher solution viscosities result in larger nanofiber radii.

A.2.5 Thickness and Topology of Fiber Muscular Thin Films

In Chapter 1, Section 1.6, we demonstrated that the pull spinning system can be used to fabricate fiber muscular thin films (fMTFs), a new nanofiber-based platform that can recapitulate the anisotropy and nanostructure of skeletal and smooth muscle tissue. Figure A.6a depicts the thickness measurement of the cantilever-shaped fMTFs using an optimal profiler. The difference in thickness between an fMTF scaffold and the murine myoblast cell line (C2C12) it was seeded with is displayed in Figure A.6b. Confocal immunofluorescent microscopy was used to visualize the C2C12 cell layer on an fMTF after 7 days in culture. We showed that fMTFs support functional measurement of twitch and tetanus curves (murine skeletal muscle) and changes in contractile stress in response to vasocon-

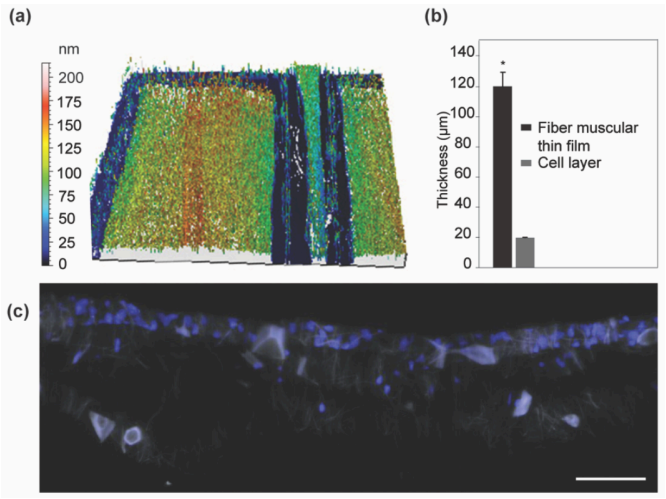


Figure A.6: Structural properties of fiber muscular thin films (fMTFs). a) Thickness of fMTF measured by optical profiler. b) Thickness measurements of fMTF and C2C12 cell layer cultured on the fiber scaffold. Thickness of the overall scaffolds, in comparison with that of the overlying cell layer. N = 2 samples with 2 FOVs. c) Confocal immunofluorescent microscopy image of C2C12 cell layer in fMTF after 7 days in culture. Nuclei stained for DAPI are visible in blue. Scale bar, 50 μm. Error is reported as SEM. * indicates p <0.05.

strictors and a rho kinase inhibitor (human vascular smooth muscle).

A.3 Mechanical Properties of Composite Micro-Actuators

In Chapter 3, we described the design and fabrication of nanofiber-reinforced micro-actuators. A key advantage of using nanofiber sheets as the strain-limiting layer in the laminate is their high surface area, in comparison to thicker microfibers. Higher surface area enables uncured PDMS to envelop the nonwoven sheet more comprehensively during the soft lithography manufacturing process; thus, the nanotextile is more firmly embedded in the elastomer matrix. To gauge the failure mode of the nanofibers when the composite actuator is extended to failure, we conducted uniaxial tensile tests. In addition to capturing the stress-strain curves of nanofibers (Figure A.7a-b: in pure sheets and embedded in a thin PDMS layer, as in the fabrication process) and multi-layer laminates, these empirical tests demonstrated that no de-bonding of the fiber sheet from the matrix is observed

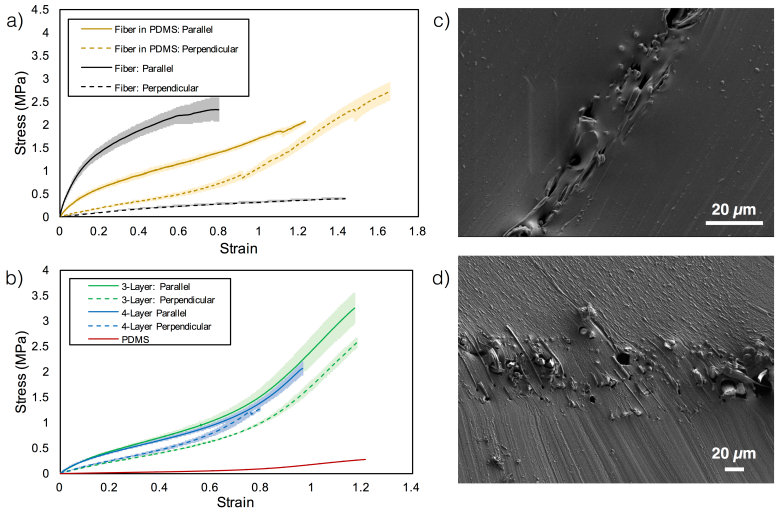


Figure A.7: Mechanical properties of a) pressed nanofiber sheets and fiber sheets embedded in 20μm PDMS, b) three- and four-layer composite laminates and pure PDMS. Scanning electron micrographs of nanofiber sheets embedded in four-layer composite laminates c) before and d) after uniaxial tensile testing. n = 3 production runs per condition. Error is reported as SEM.

after the sample is extended to failure (Figure A.7c-d). Rather than de-bonding from the PDMS matrix, the nanofibers experienced a tensile break.

A.3.1 Pressure vs. Inflating Channel Area

As described in Section 3.4, the relationship between input pressure and curvature of soft actuators is nonlinear. One way to observe this relation is to observe the area of the inflating air channel at known pressures (Figure A.8).

A.3.2 Burst Pressure Increases with Fiber Reinforcement

The failure pressure of nanofiber-reinforced actuators is significantly higher than that of silicone-only actuators. In this experiment, both sets of actuators were pressurized pneumatically. All test devices were fabricated using the same processing parameters, including internal channel height (0.5 mm), thickness of internal channel membrane (0.35 mm), and thickness of adhesion layer during the

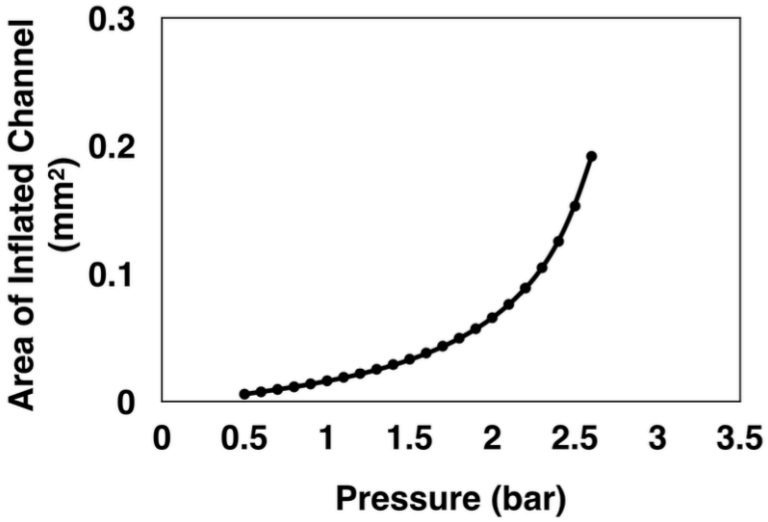


Figure A.8: The area of the inflating channel increases nonlinearly with applied pressure.

co-bonding process (0.03 mm). During pressurization, the membrane above the internal actuator channel inflates and thins. When the burst pressure is reached, a tear in this membrane forms. The rupture is commonly located toward the center of the channel, measures roughly 1 cm in length, and is oriented parallel to the length of the actuator (e.g., vertically down the channel, and not horizontally across it).

A.4 Laminate Plate Model for Soft Composite Actuators

A.4.1 Schematics of Composite Laminates

A general schematic of an arbitrary composite laminate is shown in Figure A.10a. The sample structure contains three types of lamina: isotropic (solid grey), anisotropic fiber-reinforced layers with fiber angle $+\varphi$ (top and bottom layers), and anisotropic layers with fiber angle $-\varphi$ (middle layer). A cross-sectional view of the structure (*inset*) indicates the laminate midplane (black dotted line), coordinate axes, and the thickness of each layer. Figure A.10b presents an illustration of the laminate

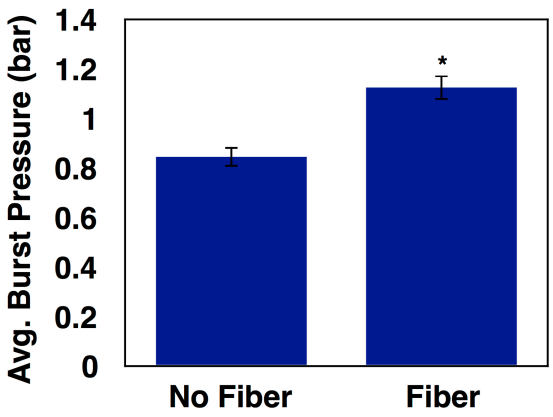


Figure A.9: The burst pressure of fiber-reinforced actuators is greater than that of silicone-only actuators. n = 5 actuators for each condition.

layup and coordinate system for the nanofiber-reinforced soft actuators presented in this study. The actuators consist of two layers: an isotropic elastomer layer at the top of the structure (solid grey), and a nanofiber sheet below (striped grey and blue). Because the initial cross-sectional area of the internal channel used to pressurize the actuator (in black) is significantly smaller than that of the elastomer layer, we assume that the elastomer lamina is homogeneous. The heights of the nanofiber (z_1) and elastomer (z_2) layers are defined in the analytical model with respect to the midplane of the structure (marked as dotted line). The base of the laminate, z_0, is defined as $-\frac{T}{2}$, where T is the total thickness of the actuator. For example, $z_1 = -\frac{T}{2} + t_f$, where t_f is the thickness of the nanofiber layer. The lower illustration in Figure A.10b shows the cross-section of a pressurized soft actuator. The total inflated area, $\mathcal{A}_i$, is shaded black. The thickness of the inflating membrane (t_m in the upper schematic) decreases as the actuator is pressurized, as per our assumption that the elastomer matrix is incompressible. Finally, the arc length of the inflated circular segment is marked as s.

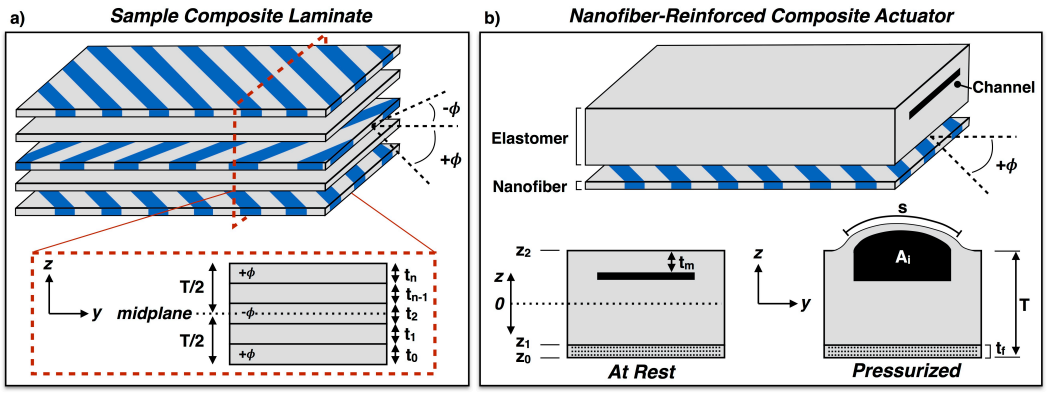


Figure A.10: Schematic showing layups of a sample composite laminate and of a nanofiber-reinforced soft actuator (cross-sectional view shown). a) A generic composite laminate with thickness T and arbitrary fiber angles $+\varphi$ and $-\varphi$. *Inset:* Cross-sectional view of lamina. b) Layup and cross-sectional views of nanofiber-reinforced soft actuator at rest and when pressurized. The hollow internal channel used to pressurize each actuator is shown in black; since the area of this section is significantly smaller than that of the elastomer layer, we assume that the elastomer lamina is homogeneous. The height of the nanofiber and elastomer layers are indicated as z_1 and z_2, respectfully. Fiber orientation angle is denoted as φ.

A.4.2 Impact of Matrix and Fiber Stiffness on Predicted Actuator Twist

The theoretical values for maximum actuator twist angle as a function of fiber orientation angle slightly overestimate the experimental results. It is possible that this discrepancy relates to human error in measuring empirical inputs, namely the Young's moduli of the matrix material (E_m) and nanofiber sheet (E_f). To better understand the effect of these stiffness values on the model's output, we calculated the maximum actuator twist angle for various E_m (using a constant E_f of 5.2 MPa, Figure A.11a) and E_f (using a constant E_m of 0.37 MPa, Figure A.11b). Our results indicate that the agreement between theoretical predictions and experimental data improves as E_f decreases; the best agreement was observed between E_f = 3-4 MPa. Future work can: 1) improve the accuracy of our model by investigating more accurate techniques to measure the Young's modulus of polymer nanofibers, and 2) reduce variance by increasing the number of actuators tested (currently n = 2-3).

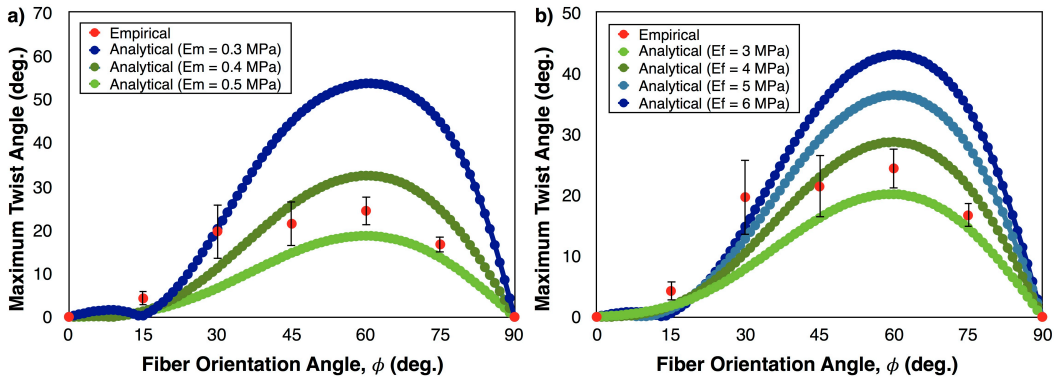


Figure A.11: Maximum actuator twist angle as a function of fiber orientation. Agreement between theoretical and empirical results is examined by varying the Young's modulus of a) the elastomer matrix (E_m) and b) the nanofiber sheet (E_f).

A.5 Performance of Soft Marine Grippers

A.5.1 Damage to Gelatinous Animal using Existing State-of-the Art Soft Gripper

Previous gentle marine manipulators have proved their ability to safety grasp and handle brittle (e.g., coral, crab) and soft (e.g., sea cucumber) animals during ROV expeditions. However, these devices are unsuited to handle ultra-delicate gelatinous marine animals. During a field expedition in the Phoenix Islands, a foam-tipped squishy robot finger[30] attempted to collect an acorn worm, a member of an extremely fragile invertebrate class. The ROV pilot lined up the soft actuators to grasp the worm; unfortunately, the force of an actuator brushing against the worm as it attempted to complete a grip ripped the animal's body and caused irreversible damage (Figure A.12). Since the pressure applied by each soft nanofiber-reinforced actuator is half that of a squishy robot finger, these novel devices represent an avenue to safely collect delicate specimens such as the acorn worm.

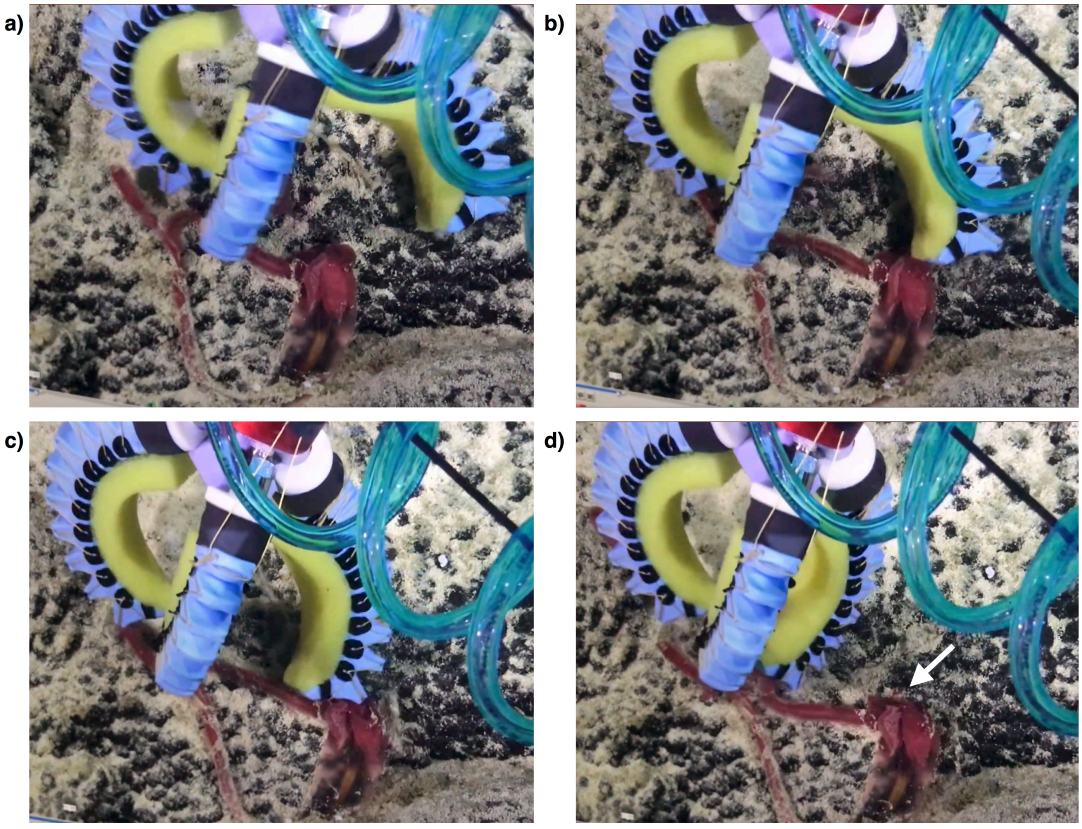


Figure A.12: An ROV pilot attempts to grasp an acorn worm using foam-tipped squishy robot fingers. a) The fingers are positioned around the body of the worm. b) A finger makes contact with the body of the animal. c) The finger presses and drags the animal against the ground, causing d) irreversible bodily damage (marked with white arrow). Images courtesy of the Schmidt Ocean Institute.

A.5.2 Calculating Jellyfish Thrust Force

Jellyfish swim by contracting and relaxing their bell, the umbrella-shaped structure that comprises most of their body. Moreover, jellyfish can can be categorized based on their propulsive mode: rowing or jetting[226]. Rowing is a more efficient method, in which an animal partially contracts its bell and produces complex vortices that interact with each other to generate additional acceleration between contraction cycles[227,228]. In contrast, jetting jellyfish fully contract their bell, producing a large stroke; the bell then closes and is refilled with water before the subsequent contraction occurs[229]. The jellyfish species targeted in this study fall into the first category[230,231,232]. Using an analytical formulation derived by Yang. et al[232] and by T.L. Daniel[233,234], we can estimate the thrust force generated by a rowing jellyfish. The thrust force, F_T, is expressed as:

$$F_T = -\varrho \mid w \mid^2 \Delta A \tag{A.1}$$

in which ϱ is the density of water, w represents the velocity of the expelled water jet relative to the bell, and ΔA is the change in cross-sectional area of the bell during a contraction cycle. $\mid w \mid$ can also be expressed as $\frac{fV}{\Delta A}$, where f indicated the frequency of bell contraction and V represents the volume of the bell. f, V, and ΔA can be written in terms of bell diameter (D) as $D^{-0.39}$, $D^{2.72}$, and $D^{1.9}$, respectively[232]. Thus, jellyfish with 7-10 cm bell diameters produce a thrust force (absolute value) of roughly 0.002-0.004 N. This force is two orders of magnitude lower than the worst-case pull force experienced by our soft actuators (at 0°).

A.5.3 Drag Force vs. Soft Gripper Speed

During tank testing of the soft gripping device, a velocity of 0.080 m s^{-1} was applied to move the entire device (hub and actuators) through water to grasp a target object. After measuring the resistance of the actuators to perturbations, we asked how fast the gripping device would have to be moved in order for the drag force of the water to overcome the gripping force. We calculated the drag force using the following equation:

$$F_D = C_D \frac{\varrho V^2}{2} A \tag{A.2}$$

in which C_D is the drag coefficient, ϱ is the fluid density, V represents gripper velocity, and A indicates the area of the target object. We approximated the target object as a solid hemisphere with $C_D = 0.42$ and $A = 0.002$ mm^2. Based on the average grip strength of 0.2 N (at a pull angle of 0°), it would be necessary to move the gripper at a minimum of 1.3 m s^{-1} for the object to the pulled from its grasp due to increased drag force. Consequently, we can assume that our testing speed is within the bounds of quasi-static grasping conditions.

A.5.4 Robustness to Applied External Forces

While grasping a gelatinous object of roughly spherical shape with high aspect ratio fingers, we observed that fingers often adhere to each other due to the self-adhesive silicone from which they are made. This forms a strong cage around the object, leading to larger amounts of force required to pull the object from the grasp compared to when the fingers do not adhere. When force is applied to the object, the fingers mostly act as tension members.

Using these observations, the act of grasping a jellyfish, then pulling the jellyfish out with some

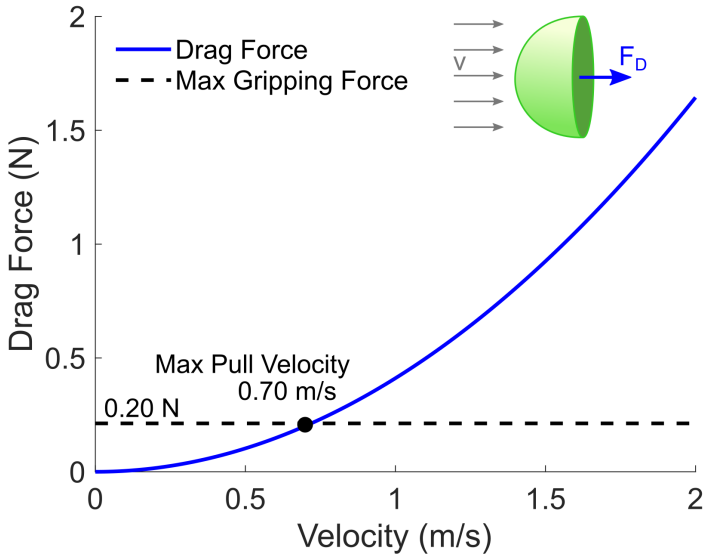


Figure A.13: The threshold at which the drag force from the water overcomes the gripping force applied by the soft actuators is roughly nine times the operational speed applied during empirical testing (0.080 m s^{-1}). The target object, a plastic jellyfish, is approximated as a solid hemisphere (shown in blue).

force F_{ext} at some angle ϑ can be reduced to a simple problem of tension in a rope applied at a given angle. Consider a two-dimensional object of diameter D being caged by two fingers that are adhered to each other toward the middle, as shown in Figure A.14. This grasp can be simplified further to a rope-pulley system, in which ropes are tied together at the point of force application. In addition, we can approximate the adhesion by allowing Rope 1 to have a weak point, which limits the maximum tensile force in that rope to $T_{1,max}$; this corresponds to the maximum shear force the adhered fingers can support before slipping. If we assume the applied force causes the rope to deflect a constant distance δ, we can use a force balance to determine the maximum external force that can be sustained at that angle.

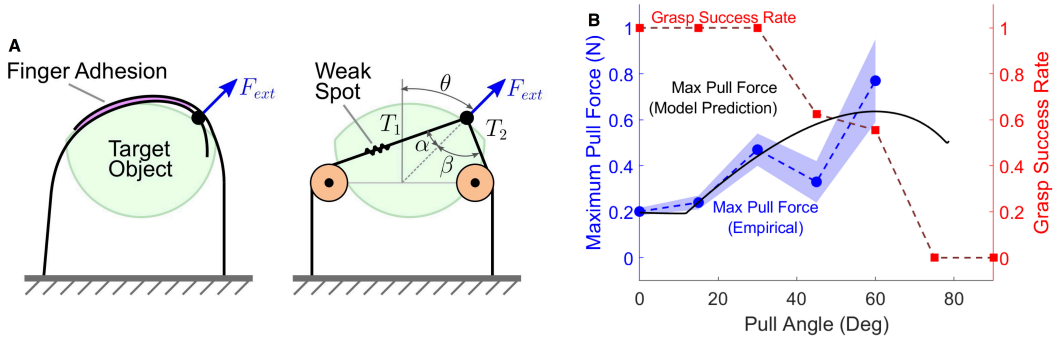


Figure A.14: a) Diagram of a two-dimensional simplification of a caging grasp, and the corresponding simple rope-pulley system. b) Predicted and empirically measured maximum pull force, and grasp success rate for various pull angles.

Taking a force balance in the radial and angular directions, we obtained the following equations:

$$\sum F_r : F_{ext} - T_1 cos(\alpha) - T_2 cos(\beta) = 0 \tag{A.3}$$

$$\sum F \quad : -T_1 sin(\alpha) + T_2 sin(\beta) = 0 \tag{A.4}$$

Next, we calculated the angles α and β using trigonometry:

$$\alpha(\vartheta) = \arcsin\left(\frac{D/2\sin(90+\vartheta)}{||\overline{AC}||}\right) \qquad ||\overline{AC}|| = \sqrt{d^2 + \left(\frac{d}{2} + \delta\tan\vartheta\right)^2} \tag{A.5}$$

$$\beta(\vartheta) = \arcsin\left(\frac{D/2\sin(90-\vartheta)}{||\overline{BC}||}\right) \qquad ||\overline{BC}|| = \sqrt{d^2 + \left(\frac{d}{2} - \delta\tan\vartheta\right)^2} \tag{A.6}$$

Simplifying and solving for F_{ext} as a function of ϑ, we obtained:

$$F_{ext,max} = T_{1,max}\left(\cos\alpha(\vartheta)\frac{\sin\alpha(\vartheta)}{\tan\beta(\vartheta)}\right) \tag{A.7}$$

which is valid for all angles before the point of force application moves past the right-side pulley.

This formula, while extremely basic, gives insight into how these soft fiber-reinforced actuators

operate. As a force is applied to an object caged in a grasp at an angle of 0°, the maximum external force is approximately 40% of the maximum shear force $T_{1,max}$. As the angle increases, the maximum external pull force increases up to a maximum force at a given angle, and then decreases. This trend can be observed in Figure A.14, where $\eth = 5$ mm and $T_{1,max} = 0.5$ N are chosen to approximately fit the data, while also being reasonable choices given the actual objects and actuators used. The caging grasp exhibits much higher complexity in three-dimensions, however we suspect the trends of this model illustrate a possible explanation for the trends seen in our empirical results (Figure 5.6b).

References

[1] Cecilia Laschi, Barbara Mazzolai, and Matteo Cianchetti. Soft robotics: Technologies and systems pushing the boundaries of robot abilities. *Science Robotics*, 1(1):eaah3690, 2016.

[2] Panagiotis Polygerinos, Nikolaus Correll, Stephen A Morin, Bobak Mosadegh, Cagdas D Onal, Kirstin Petersen, Matteo Cianchetti, Michael T Tolley, and Robert F Shepherd. Soft robotics: Review of fluid-driven intrinsically soft devices; manufacturing, sensing, control, and applications in human-robot interaction. *Advanced Engineering Materials*, 19(12):1700016, 2017.

[3] Steven I Rich, Robert J Wood, and Carmel Majidi. Untethered soft robotics. *Nature Electronics*, 1(2):102, 2018.

[4] Andrew D Marchese, Robert K Katzschmann, and Daniela Rus. A recipe for soft fluidic elastomer robots. *Soft Robotics*, 2(1):7–25, 2015.

[5] Sangbae Kim, Cecilia Laschi, and Barry Trimmer. Soft robotics: a bioinspired evolution in robotics. *Trends in Biotechnology*, 31(5):287–294, 2013.

[6] Vernon L Nickel, Jacquelin Perry, and Alice L Garrett. Development of useful function in the severely paralyzed hand. *The Journal of Bone and Joint Surgery*, 45(5):933–952, 1963.

[7] Erik H Skorina, Ming Luo, Wut Yee Oo, Weijia Tao, Fuchen Chen, Sina Youssefian, Nima Rahbar, and Cagdas D Onal. Reverse pneumatic artificial muscles (rpams): Modeling, integration, and control. *PloS One*, 13(10):e0204637, 2018.

[8] Danial Sangian, Ali Jeiranikhameneh, Sina Naficy, Stephen Beirne, and Geoffrey M Spinks. Three-dimensional printed braided sleeves for manufacturing mckibben artificial muscles. *3D Printing and Additive Manufacturing*, 0(0), 2018.

[9] Bertrand Tondu and Pierre Lopez. The mckibben muscle and its use in actuating robot-arms showing similarities with human arm behaviour. *Industrial Robot: An International Journal*, 24(6):432–439, 1997.

[10] Karun B. Shimoga and Andrew A. Goldenberg. Soft robotic fingertips: Part i: A comparison of construction materials. *The International Journal of Robotics Research*, 15(4):320–334, 1996.

[11] Prasad Akella and Mark Cutkosky. Manipulating with soft fingers: modeling contacts and dynamics. In *Robotics and Automation, 1989. Proceedings., 1989 IEEE International Conference on*, pages 764–769. IEEE, 1989.

[12] Karun B Shimoga and Andrew A Goldenberg. Soft materials for robotic fingers. In *Robotics and Automation, 1992. Proceedings., 1992 IEEE International Conference on*, pages 1300–1305. IEEE, 1992.

[13] Eric Brown, Nicholas Rodenberg, John Amend, Annan Mozeika, Erik Steltz, Mitchell R Zakin, Hod Lipson, and Heinrich M Jaeger. Universal robotic gripper based on the jamming of granular material. *Proceedings of the National Academy of Sciences*, 107(44):18809–18814, 2010.

[14] Eric I Corwin, Heinrich M Jaeger, and Sidney R Nagel. Structural signature of jamming in granular media. *Nature*, 435(7045):1075, 2005.

[15] Stephen Licht, Everett Collins, Dorick Ballat-Durand, and Manuel Lopes-Mendes. Universal jamming grippers for deep-sea manipulation. In *OCEANS 2016 MTS/IEEE Monterey*, pages 1–5. IEEE, 2016.

[16] Michael Wehner, Ryan L Truby, Daniel J Fitzgerald, Bobak Mosadegh, George M Whitesides, Jennifer A Lewis, and Robert J Wood. An integrated design and fabrication strategy for entirely soft, autonomous robots. *Nature*, 536(7617):451, 2016.

[17] Robert F Shepherd, Filip Ilievski, Wonjae Choi, Stephen A Morin, Adam A Stokes, Aaron D Mazzeo, Xin Chen, Michael Wang, and George M Whitesides. Multigait soft robot. *Proceedings of the National Academy of Sciences*, 108(51):20400–20403, 2011.

[18] Michael T Tolley, Robert F Shepherd, Bobak Mosadegh, Kevin C Galloway, Michael Wehner, Michael Karpelson, Robert J Wood, and George M Whitesides. A resilient, untethered soft robot. *Soft Robotics*, 1(3):213–223, 2014.

[19] Wei Wang, Jang-Yeob Lee, Hugo Rodrigue, Sung-Hyuk Song, Won-Shik Chu, and Sung-Hoon Ahn. Locomotion of inchworm-inspired robot made of smart soft composite (ssc). *Bioinspiration & Biomimetics*, 9(4):046006, 2014.

[20] Sangok Seok, Cagdas D Onal, Robert Wood, Daniela Rus, and Sangbae Kim. Peristaltic locomotion with antagonistic actuators in soft robotics. In *Robotics and Automation (ICRA), 2010 IEEE International Conference on*, pages 1228–1233. IEEE, 2010.

[21] Takuya Umedachi, Vishesh Vikas, and Barry A Trimmer. Softworms: the design and control of non-pneumatic, 3d-printed, deformable robots. *Bioinspiration & Biomimetics*, 11(2):025001, 2016.

[22] Cagdas D Onal and Daniela Rus. Autonomous undulatory serpentine locomotion utilizing body dynamics of a fluidic soft robot. *Bioinspiration & Biomimetics*, 8(2):026003, 2013.

[23] Florian Berlinger, Mihai Duduta, Hudson Gloria, David Clarke, Radhika Nagpal, and Robert Wood. A modular dielectric elastomer actuator to drive miniature autonomous underwater vehicles. In *2018 IEEE International Conference on Robotics and Automation (ICRA)*, pages 3429–3435. IEEE, 2018.

[24] Tiefeng Li, Guorui Li, Yiming Liang, Tingyu Cheng, Jing Dai, Xuxu Yang, Bangyuan Liu, Zedong Zeng, Zhilong Huang, Yingwu Luo, et al. Fast-moving soft electronic fish. *Science Advances*, 3(4):e1602045, 2017.

[25] Andrew D Marchese, Cagdas D Onal, and Daniela Rus. Autonomous soft robotic fish capable of escape maneuvers using fluidic elastomer actuators. *Soft Robotics*, 1(1):75–87, 2014.

[26] Koichi Suzumori, Satoshi Endo, Takefumi Kanda, Naomi Kato, and Hiroyoshi Suzuki. A bending pneumatic rubber actuator realizing soft-bodied manta swimming robot. In *Robotics and Automation, 2007 IEEE International Conference on*, pages 4975–4980. IEEE, 2007.

[27] Whitney Crooks, Gabrielle Vukasin, Maeve O'Sullivan, William Messner, and Chris Rogers. Fin ray effect inspired soft robotic gripper: From the robosoft grand challenge toward optimization. *Frontiers in Robotics and AI*, 3:70, 2016.

[28] Matteo Cianchetti, Maurizio Follador, Barbara Mazzolai, Paolo Dario, and Cecilia Laschi. Design and development of a soft robotic octopus arm exploiting embodied intelligence. In *Robotics and Automation (ICRA), 2012 IEEE International Conference on*, pages 5271–5276. IEEE, 2012.

[29] Jun Shintake, Samuel Rosset, Bryan Schubert, Dario Floreano, and Herbert Shea. Versatile soft grippers with intrinsic electroadhesion based on multifunctional polymer actuators. *Advanced Materials*, 28(2):231–238, 2016.

[30] Kevin C Galloway, Kaitlyn P Becker, Brennan Phillips, Jordan Kirby, Stephen Licht, Dan Tchernov, Robert J Wood, and David F Gruber. Soft robotic grippers for biological sampling on deep reefs. *Soft Robotics*, 3(1):23–33, 2016.

[31] Ramses V Martinez, Jamie L Branch, Carina R Fish, Lihua Jin, Robert F Shepherd, Rui Nunes, Zhigang Suo, and George M Whitesides. Robotic tentacles with three-dimensional mobility based on flexible elastomers. *Advanced Materials*, 25(2):205–212, 2013.

[32] Robert K Katzschmann, Joseph DelPreto, Robert MacCurdy, and Daniela Rus. Exploration of underwater life with an acoustically controlled soft robotic fish. *Science Robotics*, 2018.

[33] Nicholas W Bartlett, Michael T Tolley, Johannes TB Overvelde, James C Weaver, Bobak Mosadegh, Katia Bertoldi, George M Whitesides, and Robert J Wood. A 3d-printed, functionally graded soft robot powered by combustion. *Science*, 349(6244):161–165, 2015.

[34] Jan Fras, Yohan Noh, Mateusz Macias, Helge Wurdemann, and Kaspar Althoefer. Bio-inspired octopus robot based on novel soft fluidic actuator. In *2018 IEEE International Conference on Robotics and Automation (ICRA)*, pages 1583–1588. IEEE, 2018.

[35] Tommaso Ranzani, Sheila Russo, F Schwab, Conor J Walsh, and Robert J Wood. Deployable stabilization mechanisms for endoscopic procedures. In *Robotics and Automation (ICRA), 2017 IEEE International Conference on*, pages 1125–1131. IEEE, 2017.

[36] Daniel Bruder, Audrey Sedal, Ram Vasudevan, and C David Remy. Force generation by parallel combinations of fiber-reinforced fluid-driven actuators. *IEEE Robotics and Automation Letters*, 3(4), 2018.

[37] Fionnuala Connolly, Conor J Walsh, and Katia Bertoldi. Automatic design of fiber-reinforced soft actuators for trajectory matching. *Proceedings of the National Academy of Sciences*, 114(1):51–56, 2017.

[38] Tommaso Ranzani, Sheila Russo, Nicholas W Bartlett, Michael Wehner, and Robert J Wood. Increasing the dimensionality of soft microstructures through injection-induced self-folding. *Advanced Materials*, 30(38):1802739, 2018.

[39] Michaël De Volder and Dominiek Reynaerts. Pneumatic and hydraulic microactuators: a review. *Journal of Micromechanics and Microengineering*, 20(4):043001, 2010.

[40] Sheila Russo, Tommaso Ranzani, J Gafford, Conor J Walsh, and Robert J Wood. Soft pop-up mechanisms for micro surgical tools: Design and characterization of compliant millimeter-scale articulated structures. In *Robotics and Automation (ICRA), 2016 IEEE International Conference on*, pages 750–757. IEEE, 2016.

[41] Sheila Russo, Tommaso Ranzani, Conor J Walsh, and Robert J Wood. An additive millimeter-scale fabrication method for soft biocompatible actuators and sensors. *Advanced Materials Technologies*, 2017.

[42] Jean-Pierre Hubschman, Jean-Louis Bourges, W Choi, Arash Mozayan, Angelo Tsirbas, Chang-Jin Kim, and Steven D Schwartz. 'The Microhand:' a new concept of micro-forceps for ocular robotic surgery. *Eye*, 24(2):364, 2010.

[43] Satoshi Konishi, Shuhei Shimomura, Shuhei Tajima, and Yasuhiko Tabata. Implementation of soft microfingers for a hMSC aggregate manipulation system. *Microsystems & Nanoengineering*, 2:15048, 2016.

[44] Yusaku Watanabe, Masanori Maeda, Naoko Yaji, Ryoichi Nakamura, and Satoshi Konishi. Small, soft, and safe microactuator for retinal pigment epithelium transplantation. In *Micro Electro Mechanical Systems, 2007. MEMS. IEEE 20th International Conference on*, pages 659–662. IEEE, 2007.

[45] Leonardo Cappello, Kevin C Galloway, Siddharth Sanan, Diana A Wagner, Rachael Granberry, Sven Engelhardt, Florian L Haufe, Jeffrey D Peisner, and Conor J Walsh. Exploiting textile mechanical anisotropy for fabric-based pneumatic actuators. *Soft Robotics*, 5(5):662–674, 2018.

[46] Leonardo Cappello, Jan T Meyer, Kevin C Galloway, Jeffrey D Peisner, Rachael Granberry, Diana A Wagner, Sven Engelhardt, Sabrina Paganoni, and Conor J Walsh. Assisting hand function after spinal cord injury with a fabric-based soft robotic glove. *Journal of Neuroengineering and Rehabilitation*, 15(1):59, 2018.

[47] Chih-Hsing Liu, Chen-Hua Chiu, Ta-Lun Chen, Tzu-Yang Pai, Yang Chen, and Mao-Cheng Hsu. A soft robotic gripper module with 3d printed compliant fingers for grasping fruits. In *2018 IEEE/ASME International Conference on Advanced Intelligent Mechatronics (AIM)*, pages 736–741. IEEE, 2018.

[48] C Blanes, M Mellado, C Ortiz, and Angel Valera. Technologies for robot grippers in pick and place operations for fresh fruits and vegetables. *Spanish Journal of Agricultural Research*, 9(4):1130–1141, 2011.

[49] Bao Guanjun, Yao Pengfei, Xu Zonggui, Li Kun, Wang Zhiheng, Zhang Libin, and Yang Qinghua. Pneumatic bio-soft robot module: Structure, elongation and experiment. *International Journal of Agricultural and Biological Engineering*, 10(2):114–122, 2017.

[50] Yongha Hwang, Omeed H Paydar, and Robert N Candler. Pneumatic microfinger with balloon fins for linear motion using 3D printed molds. *Sensors and Actuators A: Physical*, 234:65–71, 2015.

[51] Shuichi Wakimoto, Koichi Suzumori, and Keiko Ogura. Miniature pneumatic curling rubber actuator generating bidirectional motion with one air-supply tube. *Advanced Robotics*, 25(9-10):1311–1330, 2011.

[52] Jungwook Paek, Inho Cho, and Jaeyoun Kim. Microrobotic tentacles with spiral bending capability based on shape-engineered elastomeric microtubes. *Scientific Reports*, 5:10768, 2015.

[53] Daniela Rus and Michael T Tolley. Design, fabrication and control of soft robots. *Nature*, 521(7553):467, 2015.

[54] Matteo Cianchetti, Andrea Arienti, Maurizio Follador, Barbara Mazzolai, Paolo Dario, and Cecilia Laschi. Design concept and validation of a robotic arm inspired by the octopus. *Materials Science and Engineering: C*, 31(6):1230–1239, 2011.

[55] Manuel Schaffner, Jakob A Faber, Lucas Pianegonda, Patrick A Rühs, Fergal Coulter, and André R Studart. 3d printing of robotic soft actuators with programmable bioinspired architectures. *Nature Communications*, 9(1):878, 2018.

[56] Bobak Mosadegh, Panagiotis Polygerinos, Christoph Keplinger, Sophia Wennstedt, Robert F Shepherd, Unmukt Gupta, Jongmin Shim, Katia Bertoldi, Conor J Walsh, and George M Whitesides. Pneumatic networks for soft robotics that actuate rapidly. *Advanced Functional Materials*, 24(15):2163–2170, 2014.

[57] Benjamin Gorissen, Wannes Vincentie, Farid Al-Bender, Dominiek Reynaerts, and Michaël De Volder. Modeling and bonding-free fabrication of flexible fluidic microactuators with a bending motion. *Journal of Micromechanics and Microengineering*, 23(4):045012, 2013.

[58] Xinquan Liang, Yi Sun, and Hongliang Ren. A flexible fabrication approach toward the shape engineering of microscale soft pneumatic actuators. *IEEE Robotics and Automation Letters*, 2(1):165–170, 2017.

[59] Fionnuala Connolly, Panagiotis Polygerinos, Conor J Walsh, and Katia Bertoldi. Mechanical programming of soft actuators by varying fiber angle. *Soft Robotics*, 2(1):26–32, 2015.

[60] Zheng Wang, Panagiotis Polygerinos, Johannes TB Overvelde, Kevin C Galloway, Katia Bertoldi, and Conor J Walsh. Interaction forces of soft fiber reinforced bending actuators. *IEEE/ASME Transactions on Mechatronics*, 22(2):717–727, 2017.

[61] Hong Kai Yap, Jeong Hoon Lim, Fatima Nasrallah, James CH Goh, and Raye CH Yeow. A soft exoskeleton for hand assistive and rehabilitation application using pneumatic actuators with variable stiffness. In *Robotics and Automation (ICRA), 2015 IEEE International Conference on*, pages 4967–4972. IEEE, 2015.

[62] Benjamin Gorissen, Michaël De Volder, Aline De Greef, and Dominiek Reynaerts. Theoretical and experimental analysis of pneumatic balloon microactuators. *Sensors and Actuators A: Physical*, 168(1):58–65, 2011.

[63] Kou Fujita, Mingcong Deng, and Shuichi Wakimoto. A miniature pneumatic bending rubber actuator controlled by using the pso-svr-based motion estimation method with the generalized gaussian kernel. *Actuators*, 6(1):6, 2017.

[64] Zheng-Ming Huang, Y-Z Zhang, M Kotaki, and S Ramakrishna. A review on polymer nanofibers by electrospinning and their applications in nanocomposites. *Composites Science and Technology*, 63(15):2223–2253, 2003.

[65] Leila F Deravi, Holly M Golecki, and Kevin K Parker. Protein-based textiles: bio-inspired and bio-derived materials for medical and non-medical applications. *Journal of Chemical and Biological Interfaces*, 1(1):25–34, 2013.

[66] Grant M. Gonzalez, Luke A. MacQueen, Johan U. Lind, Stacey A. Fitzgibbons, Christophe O. Chantre, Isabelle Huggler, Holly M. Golecki, Josue A. Goss, and Kevin K. Parker. Production of synthetic, para-aramid and biopolymer nanofibers by immersion rotary jet-spinning. *Macromolecular Materials and Engineering*, 302(1), 2017.

[67] Andrew K. Capulli, Luke A. MacQueen, Sean P. Sheehy, and Kevin K. Parker. Fibrous scaffolds for building hearts and heart parts. *Advanced Drug Delivery Reviews*, 96:83–102, 2016.

[68] Veysi Malkoc and Lingqian Chang. Applications of electrospun nanofibers in neural tissue engineering. *European Journal of BioMedical Research*, 1(3):25–29, 2015.

[69] Jun Seop Lee, Oh Seok Kwon, Seon Joo Park, Eun Yu Park, Sun Ah You, Hyeonseok Yoon, and Jyongsik Jang. Fabrication of ultrafine metal-oxide-decorated carbon nanofibers for dmmp sensor application. *ACS Nano*, 5(10):7992–8001, 2011.

[70] Wenying Liu, Stavros Thomopoulos, and Younan Xia. Electrospun nanofibers for regenerative medicine. *Advanced Healthcare Materials*, 1(1):10–25, 2012.

[71] Gabriel A Silva, Catherine Czeisler, Krista L Niece, Elia Beniash, Daniel A Harrington, John A Kessler, and Samuel I Stupp. Selective differentiation of neural progenitor cells by high-epitope density nanofibers. *Science*, 303(5662):1352–1355, 2004.

[72] A Sharma, Ashish Gupta, G Rath, A Goyal, RB Mathur, and Sanjay R Dhakate. Electrospun composite nanofiber-based transmucosal patch for anti-diabetic drug delivery. *Journal of Materials Chemistry B*, 1(27):3410–3418, 2013.

[73] Milena Ignatova, Nevena Manolova, and Iliya Rashkov. Electrospun antibacterial chitosan-b ased fibers. *Macromolecular Bioscience*, 13(7):860–872, 2013.

[74] Travis J Sill and Horst A von Recum. Electrospinning: applications in drug delivery and tissue engineering. *Biomaterials*, 29(13):1989–2006, 2008.

[75] Lauren Matlock-Colangelo, Daehwan Cho, Christine L Pitner, Margaret W Frey, and Antje J Baeumner. Functionalized electrospun nanofibers as bioseparators in microfluidic systems. *Lab on a Chip*, 12(9):1696–1701, 2012.

[76] Zaicheng Sun, Eyal Zussman, Alexander L Yarin, Joachim H Wendorff, and Andreas Greiner. Compound core–shell polymer nanofibers by co-electrospinning. *Advanced Materials*, 15(22):1929–1932, 2003.

[77] Taiji Zhang, Wei Wang, Dayong Zhang, Xinxiang Zhang, Yurong Ma, Yinglin Zhou, and Limin Qi. Biotemplated synthesis of gold nanoparticle–bacteria cellulose nanofiber nanocomposites and their application in biosensing. *Advanced Functional Materials*, 20(7):1152–1160, 2010.

[78] Sukumar Thenmozhi, Nallasamy Dharmaraj, Krishnagounder Kadirvelu, and Hak Yong Kim. Electrospun nanofibers: new generation materials for advanced applications. *Materials Science and Engineering: B*, 217:36–48, 2017.

[79] Zhenyi Zhang, Changlu Shao, Xinghua Li, Changhua Wang, Mingyi Zhang, and Yichun Liu. Electrospun nanofibers of p-type nio/n-type zno heterojunctions with enhanced photocatalytic activity. *ACS Applied Materials & Interfaces*, 2(10):2915–2923, 2010.

[80] Yunqian Dai, Wenying Liu, Eric Formo, Yueming Sun, and Younan Xia. Ceramic nanofibers fabricated by electrospinning and their applications in catalysis, environmental science, and energy technology. *Polymers for Advanced Technologies*, 22(3):326–338, 2011.

[81] Yuya Ishii, Ryohei Kaminose, and Mitsuo Fukuda. Optical waveguiding in an electrospun polymer nanofiber. In *Journal of Physics: Conference Series*, volume 433, page 012006. IOP Publishing, 2013.

[82] Jongho Kim, Jaeguk Noh, Seonyoung Jo, Ko Eun Park, Won Ho Park, and Taek Seung Lee. Simple technique for spatially separated nanofibers/nanobeads by multinozzle electrospinning toward white-light emission. *ACS Applied Materials & Interfaces*, 5(13):6038–6044, 2013.

[83] Andrea Camposeo, Luana Persano, and Dario Pisignano. Light-emitting electrospun nanofibers for nanophotonics and optoelectronics. *Macromolecular Materials and Engineering*, 298(5):487–503, 2013.

[84] Chieh Chang, Van H Tran, Junbo Wang, Yiin-Kuen Fuh, and Liwei Lin. Direct-write piezoelectric polymeric nanogenerator with high energy conversion efficiency. *Nano Letters*, 10(2):726–731, 2010.

[85] Gernot Hochleitner, Tomasz Jüngst, Toby D Brown, Kathrin Hahn, Claus Moseke, Franz Jakob, Paul D Dalton, and Jürgen Groll. Additive manufacturing of scaffolds with sub-micron filaments via melt electrospinning writing. *Biofabrication*, 7(3):035002, 2015.

[86] Andrew K Capulli, Maximillian Y Emmert, Francesco S Pasqualini, Debora Kehl, Etem Caliskan, Johan U Lind, Sean P Sheehy, Sung Jin Park, Seungkuk Ahn, Benedikt Weber, et al. JetValve: Rapid manufacturing of biohybrid scaffolds for biomimetic heart valve replacement. *Biomaterials*, 133:229–241, 2017.

[87] Ji Wang and Amrinder S Nain. Suspended micro/nanofiber hierarchical biological scaffolds fabricated using non-electrospinning step technique. *Langmuir*, 30(45):13641–13649, 2014.

[88] Quynh P Pham, Upma Sharma, and Antonios G Mikos. Electrospinning of polymeric nanofibers for tissue engineering applications: a review. *Tissue Engineering*, 12(5):1197–1211, 2006.

[89] Khaled Mezghani and Joseph E Spruiell. High speed melt spinning of poly (l-lactic acid) filaments. *Journal of Polymer Science Part B: Polymer Physics*, 36(6):1005–1012, 1998.

[90] Kgabo P Matabola, AR De Vries, Francis S Moolman, and Adriaan S Luyt. Single polymer composites: A review. *Journal of Materials Science*, 44(23):6213, 2009.

[91] Scott M Berry, Steven A Harfenist, Robert W Cohn, and Robert S Keynton. Characterization of micromanipulator-controlled dry spinning of micro-and sub-microscale polymer fibers. *Journal of Micromechanics and Microengineering*, 16(9):1825, 2006.

[92] Wei Wei, Yaopeng Zhang, Yingmei Zhao, Jie Luo, Huili Shao, and Xuechao Hu. Bio-inspired capillary dry spinning of regenerated silk fibroin aqueous solution. *Materials Science and Engineering: C*, 31(7):1602–1608, 2011.

[93] David M Phillips, Lawrence F Drummy, Rajesh R Naik, C Hugh, Douglas M Fox, Paul C Trulove, and Robert A Mantz. Regenerated silk fiber wet spinning from an ionic liquid solution. *Journal of Materials Chemistry*, 15(39):4206–4208, 2005.

[94] Kevin D Nelson, Andres Romero, Paula Waggoner, Brent Crow, Angela Borneman, and George M Smith. Technique paper for wet-spinning poly (l-lactic acid) and poly (dl-lactide-co-glycolide) monofilament fibers. *Tissue Engineering*, 9(6):1323–1330, 2003.

[95] CJ Luo, Simeon D Stoyanov, Eleanor Stride, Eddie Pelan, and Mohan Edirisinghe. Electrospinning versus fibre production methods: from specifics to technological convergence. *Chemical Society Reviews*, 41(13):4708–4735, 2012.

[96] Jeffrey E Plowman, Santanu Deb-Choudhury, Stefan Clerens, Ancy Thomas, Charisa D Cornellison, and Jolon M Dyer. Unravelling the proteome of wool: towards markers of wool quality traits. *Journal of Proteomics*, 75(14):4315–4324, 2012.

[97] Amrinder S Nain, Julie A Phillippi, Metin Sitti, James MacKrell, Phil G Campbell, and Cristina Amon. Control of cell behavior by aligned micro/nanofibrous biomaterial scaffolds fabricated by spinneret-based tunable engineered parameters (step) technique. *Small*, 4(8):1153–1159, 2008.

[98] Amrinder S Nain, Metin Sitti, Annette Jacobson, Tomasz Kowalewski, and Cristina Amon. Dry spinning based spinneret based tunable engineered parameters (step) technique for controlled and aligned deposition of polymeric nanofibers. *Macromolecular Rapid Communications*, 30(16):1406–1412, 2009.

[99] Mohammad R Badrossamay, Holly A McIlwee, Josue A Goss, and Kevin K Parker. Nanofiber assembly by rotary jet-spinning. *Nano Letters*, 10(6):2257–2261, 2010.

[100] Paula Mellado, Holly A McIlwee, Mohammad R Badrossamay, Josue A Goss, Lakshminarayanan Mahadevan, and Kevin K Parker. A simple model for nanofiber formation by rotary jet-spinning. *Applied Physics Letters*, 99(20):203107, 2011.

[101] Mohammad R Badrossamay, Kartik Balachandran, Andrew K Capulli, Holly M Golecki, Ashutosh Agarwal, Josue A Goss, Hansu Kim, Kwanwoo Shin, and Kevin K Parker. Engineering hybrid polymer-protein super-aligned nanofibers via rotary jet spinning. *Biomaterials*, 35(10):3188–3197, 2014.

[102] Holly McIlwee Golecki, Hongyan Yuan, Calla Glavin, Benjamin Potter, Mohammad R Badrossamay, Josue A Goss, Michael D Phillips, and Kevin Kit Parker. Effect of solvent evaporation on fiber morphology in rotary jet spinning. *Langmuir*, 30(44):13369–13374, 2014.

[103] Daoheng Sun, Chieh Chang, Sha Li, and Liwei Lin. Near-field electrospinning. *Nano Letters*, 6(4):839–842, 2006.

[104] Matthias ML Arras, Christian Grasl, Helga Bergmeister, and Heinrich Schima. Electrospinning of aligned fibers with adjustable orientation using auxiliary electrodes. *Science and Technology of Advanced Materials*, 13(3):035008, 2012.

[105] Dietmar W Hutmacher and Paul D Dalton. Melt electrospinning. *Chemistry–An Asian Journal*, 6(1):44–56, 2011.

[106] Toby D Brown, Paul D Dalton, and Dietmar W Hutmacher. Direct writing by way of melt electrospinning. *Advanced Materials*, 23(47):5651–5657, 2011.

[107] Chiho Song, John A Rogers, Jong-Man Kim, and Heejoon Ahn. Patterned polydiacetylene-embedded polystyrene nanofibers based on electrohydrodynamic jet printing. *Macromolecular Research*, 23(1):118–123, 2015.

[108] Apinya Chanthakulchan, Pisut Koomsap, Kampanat Auyson, and Pitt Supaphol. Development of an electrospinning-based rapid prototyping for scaffold fabrication. *Rapid Prototyping Journal*, 21(3):329–339, 2015.

[109] Alexander Tokarev, Darya Asheghali, Ian M Griffiths, Oleksandr Trotsenko, Alexey Gruzd, Xin Lin, Howard A Stone, and Sergiy Minko. Touch-and brush-spinning of nanofibers. *Advanced Materials*, 27(41):6526–6532, 2015.

[110] Dmitri Volfson, Scott Cookson, Jeff Hasty, and Lev S Tsimring. Biomechanical ordering of dense cell populations. *Proceedings of the National Academy of Sciences*, 105(40):15346–15351, 2008.

[111] Ian W Hamley. *Introduction to Soft Matter: Polymers, Colloids, Amphiphiles and Liquid Crystals*. Wiley, 2000.

[112] Leila F. Deravi, Nina R. Sinatra, Christophe O. Chantre, Alexander P. Nesmith, Hongyan Yuan, Sahm K. Deravi, Josue A. Goss, Luke A. MacQueen, Mohammad R. Badrossamy, Grant M. Gonzalez, Michael D. Phillips, and Kevin K. Parker. Design and fabrication of fibrous nanomaterials using pull spinning. *Macromolecular Materials and Engineering*, 302(3), 2017.

[113] Jayesh Doshi and Darrell H Reneker. Electrospinning process and applications of electrospun fibers. *Journal of Electrostatics*, 35(2-3):151–160, 1995.

[114] Nagarajan Muthuraman Thoppey, Jason R Bochinski, Laura I Clarke, and Russell E Gorga. Unconfined fluid electrospun into high quality nanofibers from a plate edge. *Polymer*, 51(21):4928–4936, 2010.

[115] Haoyi Li and Weimin Yang. Electrospinning technology in non-woven fabric manufacturing. In H.Y. Jeon, editor, *Non-woven Fabrics*. InTech, 2016.

[116] Gobind S Bisht, Giulia Canton, Alireza Mirsepassi, Lawrence Kulinsky, Seajin Oh, Derek Dunn-Rankin, and Marc J Madou. Controlled continuous patterning of polymeric nanofibers on three-dimensional substrates using low-voltage near-field electrospinning. *Nano Letters*, 11(4):1831–1837, 2011.

[117] Tingping Lei, Xizhao Lu, and Fuqian Yang. Fabrication of various micro/nano structures by modified near-field electrospinning. *AIP Advances*, 5(4):041301, 2015.

[118] Kamal Sarkar, Carlos Gomez, Steve Zambrano, Michael Ramirez, Eugenio de Hoyos, Horacio Vasquez, and Karen Lozano. Electrospinning to forcespinning™. *Materials Today*, 13(11):12–14, 2010.

[119] Suntharavathanan Mahalingam and Mohan Edirisinghe. Forming of polymer nanofibers by a pressurised gyration process. *Macromolecular Rapid Communications*, 34(14):1134–1139, 2013.

[120] Bahijja Tolulope Raimi-Abraham, Suntharavathanan Mahalingam, Mohan Edirisinghe, and Duncan QM Craig. Generation of poly (n-vinylpyrrolidone) nanofibres using pressurised gyration. *Materials Science and Engineering: C*, 39:168–176, 2014.

[121] Zewen Xu, Sunthar Mahalingam, Pooja Basnett, Bahijja Raimi-Abraham, Ipsita Roy, Duncan Craig, and Mohan Edirisinghe. Making nonwoven fibrous poly (ε-caprolactone) constructs for antimicrobial and tissue engineering applications by pressurized melt gyration. *Macromolecular Materials and Engineering*, 301(8):922–934, 2016.

[122] Tao Huang, Larry R Marshall, Jack Eugene Armantrout, Scott Yembrick, William H Dunn, James M Oconnor, Tim Mueller, Marios Avgousti, and Mark David Wetzel. Production of nanofibers by melt spinning, October 2 2012. US Patent 8,277,711.

[123] Rafael E Benavides, Sadhan C Jana, and Darrell H Reneker. Nanofibers from scalable gas jet process. *ACS Macro Letters*, 1(8):1032–1036, 2012.

[124] Lidia E Larrondo and R St. John Manley. Electrostatic fiber spinning from polymer melts. i. experimental observations on fiber formation and properties. *Journal of Polymer Science: Polymer Physics Edition*, 19(6):909–920, 1981.

[125] Sunil Kumar Vimal, Nadim Ahamad, and Dhirendra S Katti. A simple method for fabrication of electrospun fibers with controlled degree of alignment having potential for nerve regeneration applications. *Materials Science and Engineering: C*, 63:616–627, 2016.

[126] Jochen Walser and Stephen J Ferguson. Oriented nanofibrous membranes for tissue engineering applications: Electrospinning with secondary field control. *Journal of the Mechanical Behavior of Biomedical Materials*, 58:188–198, 2016.

[127] Manoranjan Acharya, Ganesh Kumar Arumugam, and Patricia A Heiden. Dual electric field induced alignment of electrospun nanofibers. *Macromolecular Materials and Engineering*, 293(8):666–674, 2008.

[128] Irvin Teh, Feng-Lei Zhou, Penny L Hubbard Cristinacce, Geoffrey JM Parker, and Jürgen E Schneider. Biomimetic phantom for cardiac diffusion mri. *Journal of Magnetic Resonance Imaging*, 43(3):594–600, 2016.

[129] Alexander P Nesmith, Ashutosh Agarwal, Megan L McCain, and Kevin K Parker. Human airway musculature on a chip: an in vitro model of allergic asthmatic bronchoconstriction and bronchodilation. *Lab on a Chip*, 14(20):3925–3936, 2014.

[130] Anna Grosberg, Alexander P Nesmith, Josue A Goss, Mark D Brigham, Megan L McCain, and Kevin K Parker. Muscle on a chip: in vitro contractility assays for smooth and striated muscle. *Journal of Pharmacological and Toxicological Methods*, 65(3):126–135, 2012.

[131] Adam W Feinberg, Alex Feigel, Sergey S Shevkoplyas, Sean Sheehy, George M Whitesides, and Kevin K Parker. Muscular thin films for building actuators and powering devices. *Science*, 317(5843):1366–1370, 2007.

[132] Rong Liu, Trevor Little, and JR Williams. Compression form-fitted athletic wear: Pressure performance, moisture management properties under different tension ratios, and corresponding psychophysical responses. *Fibers and Polymers*, 15(3):632–644, 2014.

[133] Erik MM Manders, Fons J Verbeek, and Jacob A Aten. Measurement of co-localization of objects in dual-colour confocal images. *Journal of Microscopy*, 169(3):375–382, 1993.

[134] Gang Wang, Megan L McCain, Luhan Yang, Aibin He, Francesco Silvio Pasqualini, Ashutosh Agarwal, Hongyan Yuan, Dawei Jiang, Donghui Zhang, Lior Zangi, et al. Modeling the mitochondrial cardiomyopathy of barth syndrome with induced pluripotent stem cell and heart-on-chip technologies. *Nature Medicine*, 20(6):616, 2014.

[135] Jianghui Zhao, Hongying Liu, and Lan Xu. Preparation and formation mechanism of highly aligned electrospun nanofibers using a modified parallel electrode method. *Materials & Design*, 90:1–6, 2016.

[136] G. R. Rakesh, G. S. Ranjit, K. K. Karthikeyan, P. Radhakrishnan, and Pullithadathil Biji. A facile route for controlled alignment of carbon nanotube-reinforced, electrospun nanofibers using slotted collector plates. *Express Polymer Letters*, 9(2), 2015.

[137] J.R.Y. Stevenson, Sandro Lattante, Pascal André, Marco Anni, and Graham A Turnbull. Fabrication of free-standing ordered fluorescent polymer nanofibres by electrospinning. *Applied Physics Letters*, 107(17), 2015.

[138] Ning Pan. Development of a constitutive theory for short-fiber yarns. part iv: The mechanics of blended fibrous structures. *Journal of the Textile Institute*, 87(3):467–483, 1996.

[139] Subhas Ghosh and L. Chapman. Effects of fiber blends and needling parameters on needlepunched moldable nonwoven fabric. *Journal of the Textile Institute*, 93(1):75–87, 2002.

[140] Alex Khang, Prashanth Ravishankar, Aditya Krishnaswamy, Patrick K Anderson, Stephanie G Cone, Zizhao Liu, Xianghong Qian, and Kartik Balachandran. Engineering anisotropic biphasic janus-type polymer nanofiber scaffold networks via centrifugal jet spinning. *Journal of Biomedical Materials Research Part B: Applied Biomaterials*, 105(8):2455–2464, 2017.

[141] Sheng-Po Fang, PitFee Jao, David E Senior, Kyoung-Tae Kim, and Yong-Kyu Yoon. Study on high throughput nanomanufacturing of photopatternable nanofibers using tube nozzle electrospinning with multi-tubes and multi-nozzles. *Micro and Nano Systems Letters*, 5(1):10, 2017.

[142] Semra Senturk-Ozer, Seda Aktas, Jing He, Frank T Fisher, and Dilhan M Kalyon. Nanoporous nanocomposite membranes via hybrid twin-screw extrusion—multijet electrospinning. *Nanotechnology*, 28(2):025301, 2016.

[143] S.P. Adhikari, G.P. Awasthi, H.J. Kim, C.H. Park, and C.S. Kim. Electrospinning directly synthesized porous tio2 nanofibers modified by graphitic carbon nitride sheets for enhanced photocatalytic degradation activity under solar light irradiation. *Langmuir*, 32(24):6163–6175, 2016.

[144] Han Bit Lee, Young Won Kim, Jonghun Yoon, Nak Kyu Lee, and Suk-Hee Park. 3d customized and flexible tactile sensor using a piezoelectric nanofiber mat and sandwich-molded elastomer sheets. *Smart Materials and Structures*, 26(4):045032, 2017.

[145] Benjamin Gorissen, Chris Van Hoof, Dominiek Reynaerts, and Michael De Volder. SU8 etch mask for patterning PDMS and its application to flexible fluidic microactuators. *Microsystems & Nanoengineering*, 2:16045, 2016.

[146] Benjamin Gorissen, Takuya Chishiro, Shuhei Shimomura, Dominiek Reynaerts, Michael De Volder, and Satoshi Konishi. Flexible pneumatic twisting actuators and their application to tilting micromirrors. *Sensors and Actuators A: Physical*, 216:426–431, 2014.

[147] Bin Li, Tao Du, Bo Yu, Jasper van der Gucht, and Feng Zhou. Caterpillar-inspired design and fabrication of a self-walking actuator with anisotropy, gradient, and instant response. *Small*, 11(28):3494–3501, 2015.

[148] Ok Chan Jeong and Satoshi Konishi. All PDMS pneumatic microfinger with bidirectional motion and its application. *Journal of Microelectromechanical Systems*, 15(4):896–903, 2006.

[149] Kevin C Galloway, Panagiotis Polygerinos, Conor J Walsh, and Robert J Wood. Mechanically programmable bend radius for fiber-reinforced soft actuators. In *Advanced Robotics (ICAR), 2013 16th International Conference on*, pages 1–6. IEEE, 2013.

[150] Shunichi Kurumaya, Hiroyuki Nabae, Gen Endo, and Koichi Suzumori. Design of thin McKibben muscle and multifilament structure. *Sensors and Actuators A: Physical*, 261:66–74, 2017.

[151] Jian Yao, Cees WM Bastiaansen, and Ton Peijs. High strength and high modulus electrospun nanofibers. *Fibers*, 2(2):158–186, 2014.

[152] Sajedeh Khorshidi, Atefeh Solouk, Hamid Mirzadeh, Saeedeh Mazinani, Jose M Lagaron, Shahriar Sharifi, and Seeram Ramakrishna. A review of key challenges of electrospun scaffolds for tissue-engineering applications. *Journal of Tissue Engineering and Regenerative Medicine*, 10(9):715–738, 2016.

[153] Shaohua Wu, Bin Duan, Xiaohong Qin, and Jonathan T Butcher. Nanofiber-structured hydrogel yarns with pH-response capacity and cardiomyocyte-drivability for bio-microactuator application. *Acta Biomaterialia*, 2017.

[154] Márcio Dias Lima, Mohammad W Hussain, Geoffrey M Spinks, Sina Naficy, Daniela Hagenasr, Julia S Bykova, Derrick Tolly, and Ray H Baughman. Efficient, absorption-powered artificial muscles based on carbon nanotube hybrid yarns. *Small*, 11(26):3113–3118, 2015.

[155] Saptarshi Chattopadhyay, T Alan Hatton, and Gregory C Rutledge. Aerosol filtration using electrospun cellulose acetate fibers. *Journal of Materials Science*, 51(1):204–217, 2016.

[156] Jonas Matulevicius, Linas Kliucininkas, Tadas Prasauskas, Dalia Buivydiene, and Dainius Martuzevicius. The comparative study of aerosol filtration by electrospun polyamide, polyvinyl acetate, polyacrylonitrile and cellulose acetate nanofiber media. *Journal of Aerosol Science*, 92:27–37, 2016.

[157] Moo Yeol Lee, Jayeon Hong, Eun Kwang Lee, Hojeong Yu, Hyoeun Kim, Jea Uk Lee, Wonoh Lee, and Joon Hak Oh. Highly flexible organic nanofiber phototransistors fabricated on a textile composite for wearable photosensors. *Advanced Functional Materials*, 26(9):1445–1453, 2016.

[158] Umesha Mogera, Abhay A Sagade, Subi J George, and Giridhar U Kulkarni. Ultrafast response humidity sensor using supramolecular nanofibre and its application in monitoring breath humidity and flow. *Scientific reports*, 4, 2014.

[159] Christopher Moraes, Jan-Hung Chen, Yu Sun, and Craig A Simmons. Microfabricated arrays for high-throughput screening of cellular response to cyclic substrate deformation. *Lab on a Chip*, 10(2):227–234, 2010.

[160] Miao Liu, Jianren Sun, Ying Sun, Christopher Bock, and Quanfang Chen. Thickness-dependent mechanical properties of polydimethylsiloxane membranes. *Journal of Micromechanics and Microengineering*, 19(3):035028, 2009.

[161] Jack A Myers. Handbook of equations for mass and area properties of various geometrical shapes. Technical report, Naval Ordnance Test Station China Lake CA, 1962.

[162] Carver, Inc. Autofour/30-12hc, 2016. [Online; accessed August 30, 2017].

[163] Robert Mangan and Michel Destrade. Gent models for the inflation of spherical balloons. *International Journal of Non-linear Mechanics*, 68:52–58, 2015.

[164] Landon M Kanner and Cornelius O Horgan. Elastic instabilities for strain-stiffening rubber-like spherical and cylindrical thin shells under inflation. *International Journal of Non-Linear Mechanics*, 42(2):204–215, 2007.

[165] Yi Sun, Shuang Song, Xinquan Liang, and Hongliang Ren. A miniature soft robotic manipulator based on novel fabrication methods. *IEEE Robotics and Automation Letters*, 1(2):617–623, 2016.

[166] Yiwan Huang, Daniel R King, Tao Lin Sun, Takayuki Nonoyama, Takayuki Kurokawa, Tasuku Nakajima, and Jian Ping Gong. Energy-dissipative matrices enable synergistic toughening in fiber reinforced soft composites. *Advanced Functional Materials*, 27(9), 2017.

[167] Noriyo Ichinose, Masaru Ishikawa, and Kiyoshi Morimoto. Effect of stress transfer between fiber and matrix on toughness of polymer composite. *Polymer Composites*, 32(10):1617–1624, 2011.

[168] Gareth M Bayley, Mikael Hedenqvist, and Peter E Mallon. Large strain and toughness enhancement of poly (dimethyl siloxane) composite films filled with electrospun polyacrylonitrile-graft-poly (dimethyl siloxane) fibres and multi-walled carbon nanotubes. *Polymer*, 52(18):4061–4072, 2011.

[169] Krishan Kumar Chawla and Marc A Meyers. *Mechanical behavior of materials*. Prentice Hall, 1999.

[170] Panagiotis Polygerinos, Zheng Wang, Johannes TB Overvelde, Kevin C Galloway, Robert J Wood, Katia Bertoldi, and Conor J Walsh. Modeling of soft fiber-reinforced bending actuators. *IEEE Transactions on Robotics*, 31(3):778–789, 2015.

[171] Benjamin M Finio and Robert J Wood. Optimal energy density piezoelectric twisting actuators. In *Intelligent Robots and Systems (IROS), 2011 IEEE/RSJ International Conference on*, pages 384–389. IEEE, 2011.

[172] Yong-Lae Park and Robert J Wood. Smart pneumatic artificial muscle actuator with embedded microfluidic sensing. In *SENSORS, 2013 IEEE*, pages 1–4. IEEE, 2013.

[173] Joshua Bishop-Moser and Sridhar Kota. Design and modeling of generalized fiber-reinforced pneumatic soft actuators. *IEEE Transactions on Robotics*, 31(3):536–545, 2015.

[174] Girish Krishnan. Kinematics of a new class of smart actuators for soft robots based on generalized pneumatic artificial muscles. In *Intelligent Robots and Systems (IROS 2014), 2014 IEEE/RSJ International Conference on*, pages 587–592. IEEE, 2014.

[175] Sung-Hoon Ahn, Kyung-Tae Lee, Hyung-Jung Kim, Renzhe Wu, Ji-Soo Kim, and Sung-Hyuk Song. Smart soft composite: An integrated 3d soft morphing structure using bend-twist coupling of anisotropic materials. *International Journal of Precision Engineering and Manufacturing*, 13(4):631–634, 2012.

[176] Hugo Rodrigue, Binayak Bhandari, Min-Woo Han, and Sung-Hoon Ahn. A shape memory alloy–based soft morphing actuator capable of pure twisting motion. *Journal of Intelligent Material Systems and Structures*, 26(9):1071–1078, 2015.

[177] Dong Wang, Ling Li, Ahmad Serjouei, Longteng Dong, Oliver Weeger, Guoying Gu, and Qi Ge. Controllable helical deformations on printed anisotropic composite soft actuators. *Applied Physics Letters*, 112(18):181905, 2018.

[178] Yi Sun, Hong Kai Yap, Xinquan Liang, Jin Guo, Peng Qi, Marcelo H Ang Jr, and Chen-Hua Yeow. Stiffness customization and patterning for property modulation of silicone-based soft pneumatic actuators. *Soft robotics*, 4(3):251–260, 2017.

[179] Yang Yang and Yonghua Chen. Novel design and 3d printing of variable stiffness robotic fingers based on shape memory polymer. In *Biomedical Robotics and Biomechatronics (BioRob), 2016 6th IEEE International Conference on*, pages 195–200. IEEE, 2016.

[180] Nina R Sinatra, Tommaso Ranzani, Joost J Vlassak, Kevin K Parker, and Robert J Wood. Nanofiber-reinforced soft fluidic micro-actuators. *Journal of Micromechanics and Microengineering*, 28(8):084002, 2018.

[181] Mei-Ling Zhu, Shi-Wei Ricky Lee, Hing-Leung Li, Tong-Yi Zhang, and Pin Tong. Modeling of torsional vibration induced by extension-twisting coupling of anisotropic composite laminates with piezoelectric actuators. *Smart materials and structures*, 11(1):55, 2002.

[182] Hugo Rodrigue, Wei Wang, Dong-Ryul Kim, and Sung-Hoon Ahn. Curved shape memory alloy-based soft actuators and application to soft gripper. *Composite Structures*, 176:398–406, 2017.

[183] Ermira J Abdullah, Dayang L Majid, Fairuz I Romli, Priyanka S Gaikwad, Lim G Yuan, and Nurul F Harun. Active control of strain in a composite plate using shape memory alloy actuators. *International Journal of Mechanics and Materials in Design*, 11(1):25–39, 2015.

[184] Sung-Hyuk Song, Jang-Yeob Lee, Hugo Rodrigue, Ik-Seong Choi, Yeon June Kang, and Sung-Hoon Ahn. 35 hz shape memory alloy actuator with bending-twisting mode. *Scientific reports*, 6:21118, 2016.

[185] Johannes Schindelin, Ignacio Arganda-Carreras, Erwin Frise, Verena Kaynig, Mark Longair, Tobias Pietzsch, Stephan Preibisch, Curtis Rueden, Stephan Saalfeld, Benjamin Schmid, et al. Fiji: an open-source platform for biological-image analysis. *Nature methods*, 9(7):676, 2012.

[186] Lessa K Grunenfelder, Nobphadon Suksangpanya, Christopher L Salinas, Garrett W Milliron, Nicholas A Yaraghi, Steven A Herrera, Kenneth Evans-Lutterodt, Steven R Nutt, Pablo D Zavattieri, and David Kisailus. Bio-inspired impact-resistant composites. *Acta Biomaterialia*, 10(9):3997–4008, 2014.

[187] Linlin Xiao, Junsheng Li, Sophie Mieszkin, Alessio Di Fino, Anthony S Clare, Maureen E Callow, James A Callow, Michael Grunze, Axel Rosenhahn, and Pavel A Levkin. Slippery liquid-infused porous surfaces showing marine antibiofouling properties. *ACS Applied Materials & Interfaces*, 5(20):10074–10080, 2013.

[188] Alexander K Epstein, Donggyoon Hong, Philseok Kim, and Joanna Aizenberg. Biofilm attachment reduction on bioinspired, dynamic, micro-wrinkling surfaces. *New Journal of Physics*, 15(9):095018, 2013.

[189] Marisa Rangel and Miriam Falkenberg. An overview of the marine natural products in clinical trials and on the market. *Journal of Coastal Life Medicine*, 3(6):421–428, 2015.

[190] Paula Kiuru, M Valeria D'Auria, Christian D Muller, Päivi Tammela, Heikki Vuorela, and Jari Yli-Kauhaluoma. Exploring marine resources for bioactive compounds. *Planta Medica*, 80(14):1234–1246, 2014.

[191] Thomas K Doyle, Graeme C Hays, Chris Harrod, and Jonathan DR Houghton. Ecological and societal benefits of jellyfish. In *Jellyfish Blooms*, pages 105–127. Springer, 2014.

[192] William M Graham, Stefan Gelcich, Kelly L Robinson, Carlos M Duarte, Lucas Brotz, Jennifer E Purcell, Laurence P Madin, Hermes Mianzan, Kelly R Sutherland, Shin-ichi Uye, et al. Linking human well-being and jellyfish: ecosystem services, impacts, and societal responses. *Frontiers in Ecology and the Environment*, 12(9):515–523, 2014.

[193] Cathy H Lucas, Daniel OB Jones, Catherine J Hollyhead, Robert H Condon, Carlos M Duarte, William M Graham, Kelly L Robinson, Kylie A Pitt, Mark Schildhauer, and Jim Regetz. Gelatinous zooplankton biomass in the global oceans: geographic variation and environmental drivers. *Global Ecology and Biogeography*, 23(7):701–714, 2014.

[194] Philip R Pugh. Gelatinous zooplankton-the forgotten fauna. *Underwater Science Program*, 14:67–78, 1989.

[195] Stefano Piraino, Ferdinando Boero, Brigitte Aeschbach, and Volker Schmid. Reversing the life cycle: medusae transforming into polyps and cell transdifferentiation in turritopsis nutricula (cnidaria, hydrozoa). *The Biological Bulletin*, 190(3):302–312, 1996.

[196] Osamu Shimomura, Frank H Johnson, and Yo Saiga. Extraction, purification and properties of aequorin, a bioluminescent protein from the luminous hydromedusan, *Aequorea*. *Journal of Cellular and Comparative Physiology*, 59(3):223–239, 1962.

[197] Vincent Pieribone and David F Gruber. *Aglow in the dark: the revolutionary science of biofluorescence*. Harvard University Press, 2005.

[198] Camille Gambini, Bérengère Abou, Alain Ponton, and Annemiek JM Cornelissen. Micro- and macrorheology of jellyfish extracellular matrix. *Biophysical Journal*, 102(1):1–9, 2012.

[199] Michael J Abrams, Ty Basinger, William Yuan, Chin-Lin Guo, and Lea Goentoro. Self-repairing symmetry in jellyfish through mechanically driven reorganization. *Proceedings of the National Academy of Sciences*, 112(26):E3365–E3373, 2015.

[200] Dave Rudolf and David Mould. An interactive fluid model of jellyfish for animation. In *International Conference on Computer Vision, Imaging and Computer Graphics*, pages 59–72. Springer, 2009.

[201] M Edwin Demont and John M Gosline. Mechanics of jet propulsion in the hydromedusan jellyfish, polyorchis pexicillatus: I. mechanical properties of the locomotor structure. *Journal of Experimental Biology*, 134(1):313–332, 1988.

[202] Casey W Dunn, Philip R Pugh, and Steven HD Haddock. Marrus claudanielis, a new species of deep-sea physonect siphonophore (siphonophora, physonectae). *Bulletin of Marine Science*, 76(3):699–714, 2005.

[203] Satja Sivčev, Joseph Coleman, Edin Omerdić, Gerard Dooly, and Daniel Toal. Underwater manipulators: A review. *Ocean Engineering*, 163:431–450, 2018.

[204] Hannah Stuart, Shiquan Wang, Oussama Khatib, and Mark R Cutkosky. The ocean one hands: An adaptive design for robust marine manipulation. *The International Journal of Robotics Research*, 36(2):150–166, 2017.

[205] Daniel M Vogt, Kaitlyn P Becker, Brennan T Phillips, Moritz A Graule, Randi D Rotjan, Timothy M Shank, Erik E Cordes, Robert J Wood, and David F Gruber. Shipboard design and fabrication of custom 3d-printed soft robotic manipulators for the investigation of delicate deep-sea organisms. *PloS one*, 13(8):e0200386, 2018.

[206] Stephen Licht, Everett Collins, Manuel Lopes Mendes, and Christopher Baxter. Stronger at depth: Jamming grippers as deep sea sampling tools. *Soft Robotics*, 4(4):305–316, 2017.

[207] Christopher Kelley, Terrence Kerby, Pierre-Marie Sarradin, Jozée Sarrazin, and Dhugal J Lindsay. Submersibles and remotely operated vehicles. *Biological sampling in the deep sea*, pages 285–305, 2016.

[208] Jonathan BC Davies, David M Lane, GC Robinson, Des J O'Brien, Martin FC Pickett, Michael Sfakiotakis, and B Deacon. Subsea applications of continuum robots. In *Underwater Technology, 1998. Proceedings of the 1998 International Symposium on*, pages 363–369. IEEE, 1998.

[209] Zhi Ern Teoh, Brennan T Phillips, Kaitlyn P Becker, Griffin Whittredge, James C Weaver, Chuck Hoberman, David F Gruber, and Robert J Wood. Rotary-actuated folding polyhedrons for midwater investigation of delicate marine organisms. *Science Robotics*, 3(20):eaat5276, 2018.

[210] Magali Zbinden, Bruce Shillito, Nadine Le Bris, Constance De Villardi de Montlaur, Erwan Roussel, François Guyot, Françoise Gaill, and Marie-Anne Cambon-Bonavita. New insigths on the metabolic diversity among the epibiotic microbial communitiy of the hydrothermal shrimp rimicaris exoculata. *Journal of Experimental Marine Biology and Ecology*, 359(2):131–140, 2008.

[211] GI Matsumoto, KA Raskoff, and DJ Lindsay. Tiburonia granrojo n. sp., a mesopelagic scyphomedusa from the pacific ocean representing the type of a new subfamily (class scyphozoa: order semaeostomeae: family ulmaridae: subfamily tiburoniinae subfam. nov.). *Marine Biology*, 143(1):73–77, 2003.

[212] Attawith Sudsang and Jean Ponce. A new approach to motion planning for disc-shaped robots manipulating a polygonal object in the plane. In *Robotics and Automation, 2000. Proceedings. ICRA'00. IEEE International Conference on*, volume 2, pages 1068–1075. IEEE, 2000.

[213] Morgan Quigley, Ken Conley, Brian Gerkey, Josh Faust, Tully Foote, Jeremy Leibs, Rob Wheeler, and Andrew Y Ng. ROS: an open-source Robot Operating System. In *ICRA Workshop on Open Source Software*, volume 3, page 5. Kobe, Japan, 2009.

[214] Thomas G Nevell, David P Edwards, AJ Davis, and Roger A Pullin. The surface properties of silicone elastomers exposed to seawater. *Biofouling*, 10(1-3):199–212, 1996.

[215] Kah Peng Lee, Tom C Arnot, and Davide Mattia. A review of reverse osmosis membrane materials for desalination - development to date and future potential. *Journal of Membrane Science*, 370(1-2):1–22, 2011.

[216] Wentao Xu, Chunfeng Ma, Jielin Ma, Tiansheng Gan, and Guangzhao Zhang. Marine biofouling resistance of polyurethane with biodegradation and hydrolyzation. *ACS Applied Materials & Interfaces*, 6(6):4017–4024, 2014.

[217] Subhas C Shit and Pathik Shah. A review on silicone rubber. *National Academy Science Letters*, 36(4):355–365, 2013.

[218] Levent Bat, Hasan Huseyin Satilmis, Zekiye Birinci-Ozdemir, Fatih Sahin, and Funda Ustun. Distribution and population dynamics of aurelia aurita (cnidaria; scyphozoa) in the southern black sea. *North-Western Journal of Zoology*, 5(2), 2009.

[219] Sheldon Rey Boco, Ephrime B Metillo, and RD Papa. Abundance, size and symbionts of catostylus sp. medusae (scyphozoa, rhizostomeae) in panguil bay, northern mindanao, philippines. *Philippine Journal of Systematic Biology*, 8:63–81, 2014.

[220] Daniel M. Aukes and Mark R. Cutkosky. Simulation-based tools for evaluating underactuated hand designs. *2013 IEEE International Conference on Robotics and Automation (ICRA)*, pages 2067–2073, May 2013.

[221] Carlo Ferrari and John Canny. Planning optimal grasps. *1992 IEEE International Conference on Robotics and Automation (ICRA)*, pages 2290–2295, May 1992.

[222] Xiao-Yi Zhang, Yoshihiko Nakamura, K. Goda, and Ken'ichi Yoshimoto. Robustness of power grasp. *Proceedings of the 1994 IEEE International Conference on Robotics and Automation*, pages 2828–2835, 1994.

[223] Yasmin Mohamed Yousry, Kui Yao, Shuting Chen, Weng Heng Liew, and Seeram Ramakrishna. Mechanisms for enhancing polarization orientation and piezoelectric parameters of pvdf nanofibers. *Advanced Electronic Materials*, 4(6):1700562, 2018.

[224] Clark B Teeple, Kaitlyn P Becker, and Robert J Wood. Soft curvature and contact force sensors for deep-sea grasping via soft optical waveguides. In *2018 IEEE/RSJ International Conference on Intelligent Robots and Systems (IROS)*, pages 1621–1627. IEEE, 2018.

[225] Siyi Xu, Daniel M Vogt, Wen-Hao Hsu, John Osborne, Timothy Walsh, Jonathan R Foster, Sarah K Sullivan, Vincent C Smith, Andreas W Rousing, Eugene C Goldfield, et al. Biocompatible soft fluidic strain and force sensors for wearable devices. *Advanced Functional Materials*, page 1807058, 2018.

[226] John O Dabiri, Sean P Colin, and John H Costello. Morphological diversity of medusan lineages constrained by animal–fluid interactions. *Journal of Experimental Biology*, 210(11):1868–1873, 2007.

[227] Brad J Gemmell, John H Costello, Sean P Colin, Colin J Stewart, John O Dabiri, Danesh Tafti, and Shashank Priya. Passive energy recapture in jellyfish contributes to propulsive advantage over other metazoans. *Proceedings of the National Academy of Sciences*, 110(44):17904–17909, 2013.

[228] John O Dabiri, Sean P Colin, John H Costello, and Morteza Gharib. Flow patterns generated by oblate medusan jellyfish: field measurements and laboratory analyses. *Journal of Experimental Biology*, 208(7):1257–1265, 2005.

[229] Silas Alben, LA Miller, and Jifeng Peng. Efficient kinematics for jet-propelled swimming. *Journal of Fluid Mechanics*, 733:100–133, 2013.

[230] John H Costello, Sean P Colin, and John O Dabiri. Medusan morphospace: phylogenetic constraints, biomechanical solutions, and ecological consequences. *Invertebrate Biology*, 127(3):265–290, 2008.

[231] Sean P Colin, John H Costello, Kakani Katija, Jamie Seymour, and Kristen Kiefer. Propulsion in cubomedusae: mechanisms and utility. *PLoS One*, 8(2):e56393, 2013.

[232] Patricia J Yang, Matthew Lemons, and David L Hu. Rowing jellyfish contract to maintain neutral buoyancy. *Theoretical and Applied Mechanics Letters*, 8(3):147–152, 2018.

[233] Thomas L Daniel. Cost of locomotion: unsteady medusan swimming. *Journal of Experimental Biology*, 119(1):149–164, 1985.

[234] Thomas L Daniel. Mechanics and energetics of medusan jet propulsion. *Canadian Journal of Zoology*, 61(6):1406–1420, 1983.